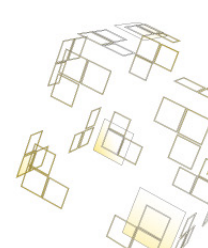
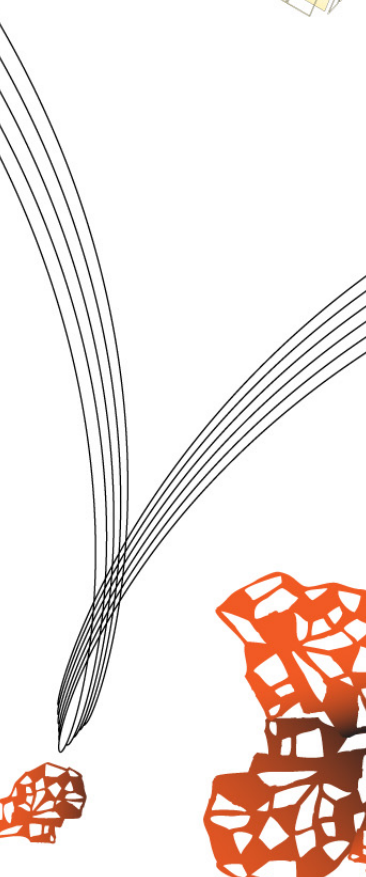




Master Thesis
Multi Scale Mechanics Group
Mechanical Engineering
Faculty of Engineering Technology



Closure laws for granular, shallow-layer, bi-dispersed flows down an inclined chute



Author : Ate te Voortwis
Committee :
Dr. T. Weinhart
Prof. Dr. rer.-nat. S. Luding
Dr. A.R. Thornton
Dr. R. Hagmeijer

MSM008
April 25, 2013

UNIVERSITEIT TWENTE.

Preface

With this MSc Thesis I would like to mark the end of my years as a student of Mechanical Engineering at the University of Twente. Although at first I was rather reluctant to start my nine-month masters project, I have to say that it turned out to be quite exciting and challenging. In these nine months I have enjoyed the satisfying experience of submerging myself in a problem, and coping with the successes and failures that come with it. The reason I actually enjoyed it however, is almost entirely attributable to the people from the Multi Scale Mechanics group, which showed superb enthusiasm in supervising and guiding me. This may seem natural, however in my opinion it is not. In countless occasions I entered Thomas' office, asking whether 'he had a minute?', and I think it took Thomas roughly two weeks to make a mental note that those meetings usually were not finished within a minute. For some reason however I always got the impression that Thomas actually liked my (more often than not, rather basic or even simple) questions, and maybe even found it challenging when I responded, again, with a doubtful 'Yeah... but why?'. In the same office Anthony had his domain, and I challenge the reader to envision how motivating it can be to have someone two doors away, that in my opinion can be described as an almost ridiculously fascinated segregation authority. Therefore I would like to stress that I did not take the tight collaboration I enjoyed the last nine months for granted, I value it highly and want to thank you both for it. In addition to that, Stefan has had a profound influence in my years as a master student in his research group. Especially in the organisation of my internship I was astonished by the vigour with which he set about arranging the matter, but also in my MSc. project he repeatedly gave new directions or insights that I would never have thought of myself. Summarising I can say that due to the pleasant, vibrant atmosphere I encountered within the Multi Scale Mechanics group, I have never had to drag myself into office, which in my opinion is rather something, and I wish to thank you for that.

Ate te Voortwis, April 25, 2013

Summary

Granular matter is present in everyday life in many forms, and can be defined as a collection of discrete, solid, macroscopic particles. The particles are macroscopic in the sense that the particles have a size of approximately μm or larger, which puts them distinctly above the atomic scale. Although granular systems are encountered in many forms both in nature and industry, a closed theoretical description such as the Navier-Stokes equations for fluids is not yet available.

The focus of this research was on geophysical mass flows, which can take rather destructive shapes in the form of mud slides and snow avalanches. A slightly more abstract system is considered in this thesis, in which dry, soft and spherical particles of two different sizes flow down an inclined rough chute. When these granular chute flows are bi-dispersed, and thus contain particles of two different sizes, segregation phenomena can occur. Due to an effect known as *kinetic sieving*, the small particles will percolate to the bottom of the flow, and in turn the large particles are squeezed upwards.

A popular model to describe these granular chute flows, originally considering only one species, is the depth-averaged shallow flow model. Given the assumption that the flow is shallow compared to its length, one can depth-average the Cauchy balances for mass and momentum, which yields a reduction in the number of variables. To be able to solve these equations however, a set of closure relations is needed, among which is a friction law that describes the relation between the downward normal stress and the shear stress exerted on the flow by the rough base.

For mono-dispersed granular chute flows such a friction law exists; the Pouliquen friction law predicts the friction for a mono-dispersed flow in terms of the flow height and the depth-averaged velocity, which are state parameters. This research strived to extend this friction law to the field of bi-dispersed flows, and use it to predict the friction coefficient in quasi 2D, bi-dispersed chute flows.

The Pouliquen friction law involves relations concerning both arresting and steady flows, and thus measurements were required for both. Since obtaining measurement data from physical experiments is in general quite hard for granular flows, a series of simulations was done using the discrete particle method (DPM). Being bi-dispersed, the flows have two additional parameters compared to mono-dispersed flows: the size-ratio between the small and large particle radii and the relative volume of the large particles with respect to the total volume of all particles. The latter parameter in this case is of most interest, since in segregated chute flows the large particles will be transported to the front of the flow (being at the top of the flow they have a higher average velocity than the small particles) and thus the relative large volume fraction will change both over time and in different regions of the flow. The size ratio however will not vary within the flow in this research (i.e. in one system there are always only two distinct particle sizes).

Both the results concerning arresting and steady state flows show very good agreement with the results for mono-dispersed flows, which supports the hypothesis that the Pouliquen friction law is also applicable to bi-dispersed flows.

Having established the friction law for different bi-dispersed configurations, it was used to predict the friction for an unsteady system. Whereas all previous simulations are done in a periodic box, now the flow is allowed to flow freely down the chute and develop a flow-front. Then the relative large particle concentration will vary throughout the flow, and have an effect on the friction coefficient experienced by the flow.

One major advantage of simulating all individual particles is that the actual friction experienced by the flow can be measured. When this measured value is compared with the value predicted by the friction law, two conclusions can be formulated. First of all, the general trend of the friction coefficient is predicted correctly, and the local concentration has a strong effect on the friction. Second however, the friction law fails to correctly predict the friction for parts of the flow in which the concentration is far from the steady state. This is a problem at the very front, where large particles are overrun by the avalanche and temporarily reside at the very bottom of the flow, causing extra friction.

Contents

Preface	i
Summary	iii
1 Introduction	1
2 Theoretical background	5
2.1 Depth averaged shallow layer equations	5
2.1.1 Mathematical background	6
2.1.2 Boundary conditions	7
2.1.3 Dimensionless form	8
2.1.4 Depth averaging	10
2.1.5 Segregation equation	12
2.1.6 Friction coefficient μ	12
2.1.7 Closure relations	13
2.2 Closure laws in terms of h_{stop}	14
2.3 Bidispersity and segregation	16
2.4 Discrete Particle Method	18
2.4.1 Contact laws	18
2.4.2 Contact laws for bi-dispersed flows	20
2.4.3 Time integration	22
2.5 Coarse graining	23
2.5.1 Theory	23
2.5.2 Coarse grained stress tensor	24
2.5.3 Spatial averaging	25
2.5.4 Smoothing length w	26
2.6 Flow height and Froude number	27
3 Simulation setup	29
3.1 Simulation parameters	29
3.2 Simulations in the periodic box	30
3.2.1 h_{stop} -algorithm	31
3.2.2 Initial packing and generation of the rough bottom	33
3.2.3 Steady flow generation	33
3.2.4 Mixed contact properties	35
3.2.5 Varying volume-ratio η	38
3.2.6 Varying size-ratio σ	39
3.3 Quasi 2D simulations	40
3.3.1 Inflow	41
3.3.2 Particle friction	43
3.3.3 Statistics	43
4 Results	45
4.1 Periodic box simulations	45
4.1.1 h_{stop} simulations	45
Sample run	46
Fitting h_{stop}	47

	System 1: Varying volume-ratio η	47
	System 2: Varying volume-ratio η with decreased small particle friction	50
	System 3: Varying size-ratio σ	51
	Conclusion	53
4.1.2	Froude flowrule	53
	Lithostatic assumption	53
	Fitting the Froude flowrule	54
	Sample run Froude simulation	54
	System 1: Varying volume-ratio η	55
	System 2: Varying volume-ratio η with decreased small particle friction	57
	System 3: Varying size-ratio σ	58
	Combined fit of h_{stop} and the Froude flowrule	60
	Fit trends	63
	Conclusion	64
4.2	Quasi 2D avalanche flow	65
4.2.1	Developing avalanche fronts	65
4.2.2	Flow height and flow front definition	67
4.2.3	Applying the $\mu(h, F, \eta)$ -flowrule	68
	Avalanche 1	69
	Avalanche 2	71
	Avalanche 3	73
	Conclusion	74
5	Conclusion and recommendations	77
5.1	Conclusion	77
5.2	Recommendations	78

Chapter 1

Introduction

The ultimate aim of this research is to be able to accurately predict geophysical mass flows, which can be seen in a widespread variety in both nature and industry. Mud slides and snow avalanches come to mind as rather destructive examples, but also transport-chutes and rotating drums in for example, food-processing flows in industry show similar features. Here a more idealised problem of dry, granular material flowing down an inclined chute is considered, containing particles of only two different sizes. Having two distinct phases, in this case differing in size, can give rise to so-called segregation phenomena. Many segregation mechanisms exist [3], and any difference in the constituents properties such as density, shape and contact forces can cause segregation. Often however the dominant one is *size segregation* [6], in which the flowing particle flow develops two segregated layers due to size differences of the particles.

The importance of understanding these segregation phenomena becomes evident in mud-slides: due to segregation effects the run-out (distance after which the avalanche stops) can be much longer for segregated flows [13]. Therefore, when predicting for example safe distances from avalanche-prone hills to build your house it is of importance to incorporate segregation effects.

In the last few decades, extensive work has been done on this type of granular flows. Due to the ongoing increase in computational capacity, the simulation of granular flows through Discrete Particle Method (DPM) solvers like [24, 26] has become feasible. On modern supercomputers simulations with $O(10^9)$ particles are possible. A typical DPM solver will integrate the equations of motion of individual particles, computing the pair-wise interaction forces with a given contact model. Real granular chute flows however incorporate a number of particles several orders of magnitude higher. For example, if one considers particles of mm in diameter, a litre of material already contains 10^6 particles. Therefore a lot of work is focused on the development of continuum models for granular flows. In the field of granular chute flows, huge progress has been achieved with models using shallow layer modelling, utilising the depth-averaged conservation equations of mass and momentum ([19], [11]).

These shallow granular layer models show a clear resemblance with the shallow-water equations. An important difference however is the introduction of a basal friction coefficient μ , whereas the shallow-fluid model has a viscous drag term, which vanishes when the velocity is zero. Originally this friction coefficient was set to be constant [19] and thus behave Coulomb like, which implied that steady flow was only possible at a single chute inclination θ , for which the friction exactly balanced the gravitational forces. Both physical [5, 8] and numerical [27] experiments however show that steady flow is possible over a range of chute inclinations.

To overcome this limitation, Pouliquen developed an improved friction law [16], characterised by two inclinations δ_1 and δ_2 , between which steady flow is possible. At chute angles below δ_1 , the friction is strong enough to dissipate all kinetic energy gained by gravitational acceleration and the flow will come to a halt. Above δ_2 the friction is too low to dissipate the gained energy and the flow accelerates indefinitely. In between the two angles steady flow is possible and there the Pouliquen friction law predicts the friction. Finally, for $\delta_1 \rightarrow \delta_2$ the Coulomb model is recovered. In this thesis an approach similar to [27] and [22] will be followed, in which a closure law for the friction, which is needed to solve the depth-averaged shallow layer equations for granular chute flows, is derived in line with the Pouliquen experimental approach [17], utilising a series of DPM simulations.

Whereas [27] and [22] only consider mono-dispersed flows, this research aims to extend this idea to bi-dispersed flows, thereby considering segregation phenomena as described in [20] and their influence on the friction coefficient μ . Bi-dispersed flows have only two different particle sizes, and their segregation

behaviour is analysed in [12].

In this work the systems considered are dry, cohesion-less, granular, bi-dispersed chute flows, i.e. flows with two differently sized types of particles, flowing down an inclined chute. In these flows the smaller sized particles will percolate to the bottom of the flow, due to an effect known as *kinetic sieving* ([15],[20]). The kinetic sieving mechanism is a result of a combination of percolation and squeeze expulsion. Due to gravity both large and small particles will fall into gaps opening up beneath them, small particles however have a larger chance of finding a gap sufficiently large. Therefore small particles percolate down easier. Squeeze expulsion is the phenomena that (both large and small) particles can be pushed either up or down due to force imbalances. This effect is not dependent on the particle size, but it does introduce a driving force for particles to move either up or down. Combined with the percolation, the result is that the small particles have a higher chance of going down, whereas the large particles are squeezed up.

In figure 1.1 several snapshots are displayed of a chute flow which is initially normally graded, i.e. all heavy large (orange) particles are at the bottom, with the small particles (blue) on top. Over time the flow will segregate, reversing the vertical order of the phases.

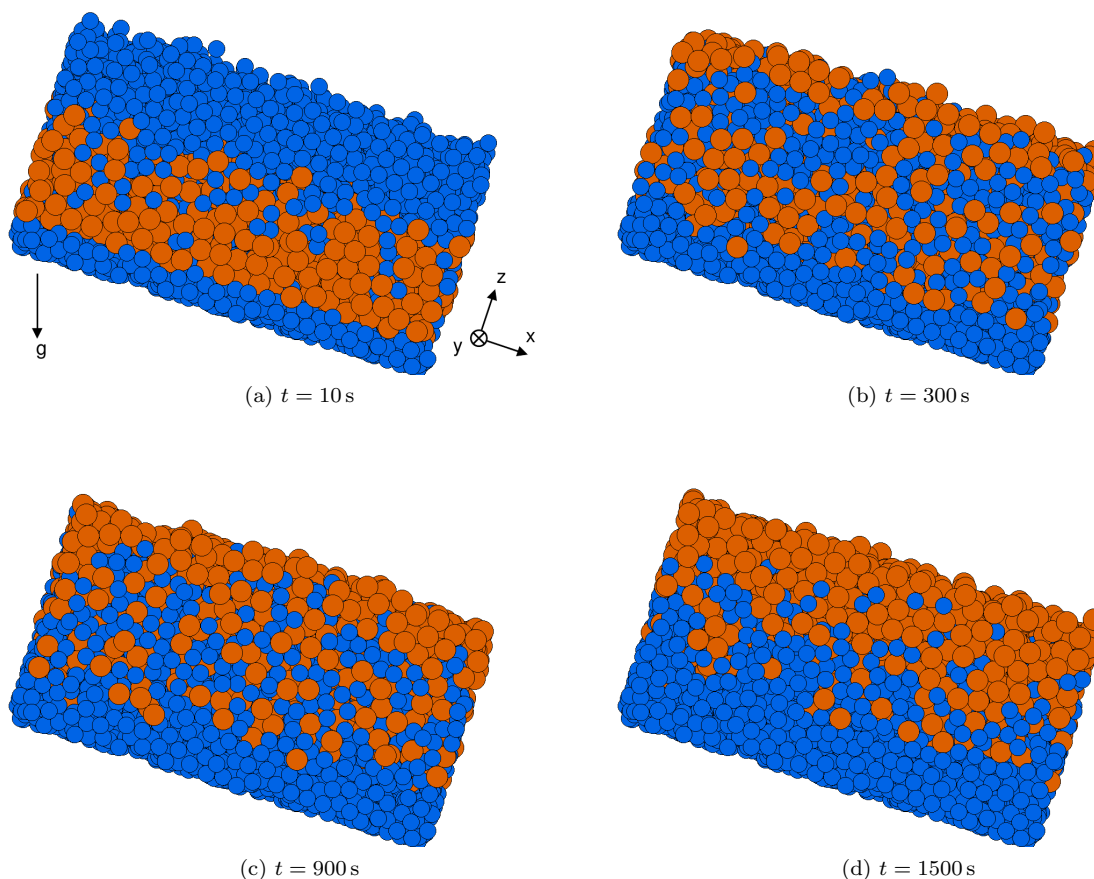


Figure 1.1: Initially normally graded flow, segregating over time, snapshots at $t = [10, 600, 900, 1500]$ s. The orange particles are 26% bigger in diameter than the blue particles (making them exactly two times larger in mass and volume). Note that the base is made out of fixed small particles, which is visible in the first snapshot.

Given the phenomena introduced, this thesis aims to answer two main research questions:

- Can the Pouliquen friction law be applied to predict the macroscopic friction in steady, bi-dispersed chute flows?
- Can the friction law be applied to predict the friction in bi-dispersed avalanche fronts, incorporating the effect of the different mixtures throughout the flow?

In this thesis the findings of the research will be reported. In chapter 2 the theories available will be treated. First the shallow granular layer equations are derived and the different closure relations needed to solve the system will be considered. In addition to that the quantities used to describe the segregation of the flow will be defined. The final part of the chapter deals with the Discrete Particle Method which is used to simulate granular systems. An important aspect of these simulations is the so-called micro-macro transition, i.e the step from discrete particle-based quantities to macroscopic fields. Then in chapter 3 an outline of the simulation setup will be discussed. Numerous simulation configurations are used to simulate both steady and non-steady systems. The results of these simulations and their comparison with the available theory will be dealt with in chapter 4. Finally a conclusion and possible future directions will be formulated in section 5.

Chapter 2

Theoretical background

This thesis spans several theoretical areas. The depth-averaged shallow-layer equations are used to describe granular chute flows with a continuum approach. They are treated in section 2.1. The closure laws needed for these equations are formulated in line with the Pouliquen experimental approach [17] in section 2.2. Derivation of the needed relations to be able to handle bi-dispersed flows is done in section 2.3. Then the Discrete Particle Method (DPM), used for the numerical experiments is described in 2.4. Next, the translation from the discrete results from the DPM simulations to the continuum macro-scale is done by means of a coarse graining method, discussed in 2.5. Finally, in section 2.6 this coarse graining method is used to derive relations for the depth averaged flow variables required.

2.1 Depth averaged shallow layer equations

In the field of granular flows a lot of work has been done on the subject of shallow layer flows. Using depth-averaged versions of the continuity equation and the Cauchy momentum equation, the number of degrees of freedom is greatly reduced. Derivation of these depth averaged shallow layer equations starts from the continuity equation and the Cauchy conservation equation for momentum. Through depth-averaging the (shallow) flow-depth direction is integrated out [11]. This gives a system of equations describing the flow in terms of depth averaged quantities which can be solved numerically, given a set of closure relations. Pouliquen *et al.* [17] developed a *flowrule* to describe the *friction coefficient* μ in terms of flow variables, being the flow height h and the depth-averaged velocity \bar{u} , yielding one of the closure relations needed. Weinhart *et al.* [27, 28] measured the coefficients needed in these closure relations for mono-dispersed flow through DPM simulations. The closure relations needed consist of a relation for the basal friction coefficient μ (in [27] referred to as the *flowrule*), a relation for the normal stress anisotropy, relating the stresses in down-slope and depth direction and a shape factor α describing the ratio between the squared average velocity and the average squared velocity. This work aims to extend this to bi-dispersed flow and to find a closure relation for the friction coefficient.

In the ongoing sections a coordinate system $Oxyz$ will be used, in which x is directed down-slope a chute at angle θ . The z direction is normal to the slope and the y coordinate is directed perpendicular to the flow direction. Note that since the bottom in general does not need to be flat, the down-slope direction is defined to be along the mean slope of the bottom.

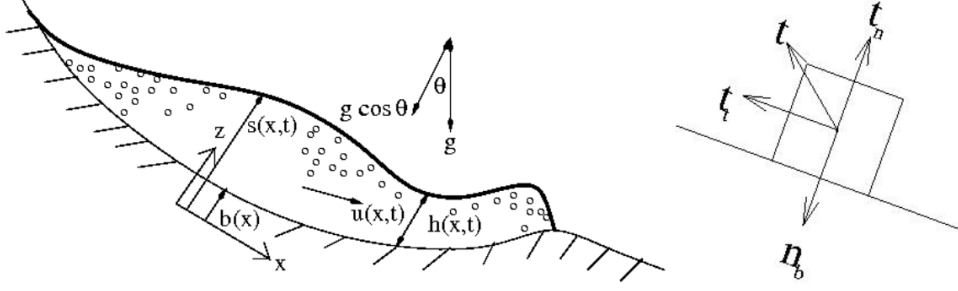


Figure 2.1: Avalanche domain with the coordinate-system and at the right the tractions $\mathbf{t} = \sigma \cdot \mathbf{n}_b$ at the base, exerted by the base on the flow. Picture taken from [2].

2.1.1 Mathematical background

The derivation starts with the continuity equation and Cauchy's momentum balance:

$$\text{Mass: } \frac{D\rho}{Dt} + \rho(\nabla \cdot \mathbf{u}) = 0, \quad (2.1)$$

$$\text{Momentum: } \frac{D\rho\mathbf{u}}{Dt} = \nabla \cdot \sigma + \rho\mathbf{B}, \quad (2.2)$$

$$\frac{D}{Dt} = \frac{\partial}{\partial t} + \mathbf{u} \cdot \nabla. \quad (2.3)$$

In these equation ρ denotes the density, $\mathbf{u} = (u, v, w)^T$ is the velocity vector, σ is the stress tensor and \mathbf{B} is the body-force-density applied. Next some assumptions are made which will simplify the set of equations. First of all the flow is assumed to be incompressible ($\frac{D\rho}{Dt} = 0$) and of uniform density, thus density is constant. Second, any gradients in y -direction are neglected, such that the flow is uniform in y -direction and there is zero flow-velocity in y -direction. This is just for simplicity, and is not needed in general. Finally the only body force present is gravity ρg , where $g = g'(\sin \theta, 0, -\cos \theta)^T$ as the chute is inclined at an angle θ . Given these assumptions, the simplified conservation equations become:

$$\text{Mass: } \nabla \cdot \mathbf{u} = \frac{\partial u}{\partial x} + \frac{\partial w}{\partial z} = 0, \quad (2.4)$$

$$\text{Momentum x: } \rho \left(\frac{\partial u}{\partial t} + u \frac{\partial u}{\partial x} + w \frac{\partial u}{\partial z} \right) = \frac{\partial \sigma_{xx}}{\partial x} + \frac{\partial \sigma_{xz}}{\partial z} + \rho g \sin \theta, \quad (2.5)$$

$$\text{Momentum z: } \rho \left(\frac{\partial w}{\partial t} + u \frac{\partial w}{\partial x} + w \frac{\partial w}{\partial z} \right) = \frac{\partial \sigma_{xz}}{\partial x} + \frac{\partial \sigma_{zz}}{\partial z} - \rho g \cos \theta. \quad (2.6)$$

Next the two spatial derivatives on the left hand side of the momentum balance for the x -direction can be rewritten:

$$u \frac{\partial u}{\partial x} + w \frac{\partial u}{\partial z} = 2u \frac{\partial u}{\partial x} + w \frac{\partial u}{\partial z} - u \frac{\partial u}{\partial x}. \quad (2.7)$$

And mass conservation is used to rewrite:

$$u \frac{\partial u}{\partial x} + w \frac{\partial u}{\partial z} = 2u \frac{\partial u}{\partial x} + w \frac{\partial u}{\partial z} + u \frac{\partial w}{\partial z}, \quad (2.8)$$

$$u \frac{\partial u}{\partial x} + w \frac{\partial u}{\partial z} = \frac{\partial u^2}{\partial x} + \frac{\partial uw}{\partial z}. \quad (2.9)$$

Similarly for the z -direction:

$$u \frac{\partial w}{\partial x} + w \frac{\partial w}{\partial z} = \frac{\partial w^2}{\partial z} + \frac{\partial uw}{\partial x}. \quad (2.10)$$

Substituting (2.9) and (2.10) in (2.5) and (2.6):

$$\text{Momentum x: } \rho \left(\frac{\partial u}{\partial t} + \frac{\partial u^2}{\partial x} + \frac{\partial uw}{\partial z} \right) = \frac{\partial \sigma_{xx}}{\partial x} + \frac{\partial \sigma_{xz}}{\partial z} + \rho g \sin \theta, \quad (2.11)$$

$$\text{Momentum z: } \rho \left(\frac{\partial w}{\partial t} + \frac{\partial w^2}{\partial z} + \frac{\partial uw}{\partial x} \right) = \frac{\partial \sigma_{xz}}{\partial x} + \frac{\partial \sigma_{zz}}{\partial z} - \rho g \cos \theta. \quad (2.12)$$

Next, if the free-surface of the flow is defined to be at $z = s(x, t)$ and the basal surface at $z = b(x, t)$ the height of the avalanche can be defined as:

$$h(x, t) = s(x, t) - b(x). \quad (2.13)$$

Note that the location of the base is fixed, i.e it does not evolve over time. From now on a superscript s and b will be used to denote quantities evaluated at the surface or the base respectively. Thus \mathbf{u}^b is the velocity-vector at the base, and \mathbf{n}^s denotes the surface-normal vector.

2.1.2 Boundary conditions

Next the boundary conditions at the base and the free-surface are derived. First of all it is observed that particles at the base or the free-surface can only move tangent to that surface. In the continuum domain this means that streamlines do not punch through the boundary surfaces. This is expressed via the kinematic boundary conditions:

$$\frac{Ds - z}{Dt} = \frac{\partial s - z}{\partial t} + u^s \frac{\partial s - z}{\partial x} - w^s = \frac{\partial s}{\partial t} + u^s \frac{\partial s}{\partial x} - w^s = 0, \quad (2.14)$$

$$\frac{Db - z}{Dt} = \frac{\partial b - z}{\partial t} + u^b \frac{\partial b - z}{\partial x} - w^b = \frac{\partial b}{\partial t} + u^b \frac{\partial b}{\partial x} - w^b = 0. \quad (2.15)$$

Note that since z is an independent coordinate, it drops out of the derivatives. In addition to these kinematic boundary conditions, boundary conditions for the *traction* at the surfaces are derived as well. The traction is defined as the force vector applied per unit area. The free-surface is defined to be traction free (i.e air-drag is neglected), and at the basal surface a Coulomb friction model is applied, relating the tangential traction to the pressure normal to the base. The direction of this tangential traction is opposite to that of the flow velocity. The traction force per unit surface \mathbf{t} is defined as the product of the stress tensor with the normal of the surface (see figure 2.1), so for the free-surface this gives:

$$\mathbf{t}^s = \sigma^s \mathbf{n}^s = \mathbf{0}. \quad (2.16)$$

The traction at the base is first decomposed in a normal and a tangential part:

$$\mathbf{t}^b = \sigma^b \mathbf{n}^b = \mathbf{t}_t^b + \mathbf{t}_n^b = \mathbf{t}_t^b - \mathbf{n}^b |\mathbf{t}_n^b|. \quad (2.17)$$

The minus indicates that the traction acts in opposite direction compared to the unit normal (see figure 2.1), i.e into the domain. At the base the Coulomb model states that \mathbf{t}_t^b is given as the product of the normal component of the traction with some friction constant μ :

$$\mathbf{t}_t^b = -\mu |\mathbf{t}_n^b| \frac{\mathbf{u}^b}{|\mathbf{u}^b|}. \quad (2.18)$$

The factor $-\frac{\mathbf{u}^b}{|\mathbf{u}^b|}$ makes sure the tangential component of the basal traction is always opposed to the flow motion (i.e slowing the flow down). The traction component normal to the base is simply the normal component of equation (2.16):

$$|\mathbf{t}_n^b| = -\mathbf{n}^b \cdot \mathbf{t}^b = -\mathbf{n}^b \cdot (\sigma^b \mathbf{n}^b). \quad (2.19)$$

So the boundary condition at the base becomes:

$$\sigma^b \mathbf{n}^b = \mu (\mathbf{n}^b \cdot (\sigma^b \mathbf{n}^b)) \frac{\mathbf{u}^b}{|\mathbf{u}^b|} + (\mathbf{n}^b \cdot (\sigma^b \mathbf{n}^b)) \mathbf{n}^b, \quad (2.20)$$

$$\sigma^b \mathbf{n}^b = (\mathbf{n}^b \cdot (\sigma^b \mathbf{n}^b)) \left(\mu \frac{\mathbf{u}^b}{|\mathbf{u}^b|} + \mathbf{n}^b \right). \quad (2.21)$$

The normal vectors \mathbf{n}^s and \mathbf{n}^b can easily be described in terms of the spatial derivatives of $s(x)$ and $b(x)$ and the unit normal vectors \mathbf{e}_x and \mathbf{e}_z :

$$\mathbf{n}^s = \frac{1}{\sqrt{(\frac{\partial s}{\partial x})^2 + 1}} \left(-\frac{\partial s}{\partial x} \mathbf{e}_x + \mathbf{e}_z \right), \quad (2.22)$$

$$\mathbf{n}^b = \frac{1}{\sqrt{(\frac{\partial b}{\partial x})^2 + 1}} \left(\frac{\partial b}{\partial x} \mathbf{e}_x - \mathbf{e}_z \right). \quad (2.23)$$

For brevity this can be written as:

$$\mathbf{n}^s = (\Delta^s)^{-1} \left(-\frac{\partial s}{\partial x} \mathbf{e}_x + \mathbf{e}_z \right), \quad \Delta^s = \sqrt{\left(\frac{\partial s}{\partial x} \right)^2 + 1}, \quad (2.24)$$

$$\mathbf{n}^b = (\Delta^b)^{-1} \left(\frac{\partial b}{\partial x} \mathbf{e}_x - \mathbf{e}_z \right), \quad \Delta^b = \sqrt{\left(\frac{\partial b}{\partial x} \right)^2 + 1}. \quad (2.25)$$

2.1.3 Dimensionless form

The equations are non-dimensionalised similar as in [11, 2], with the typical flow length L , a typical flow height H and the gravitational acceleration g . This is done such that later the fact that for shallow chute flows the *aspect ratio* $\varepsilon = H/L$ is small can be exploited, i.e the avalanche height is much smaller than its length: $\varepsilon \ll 1$.

$$x = L\tilde{x}, \quad z = H\tilde{z}, \quad (2.26)$$

$$t = \sqrt{L/g}\tilde{t}, \quad (2.27)$$

$$u = \sqrt{Lg}\tilde{u}, \quad w = \varepsilon\sqrt{Lg}\tilde{w}, \quad \varepsilon = H/L, \quad (2.28)$$

$$\sigma_{xx} = \rho g H \tilde{\sigma}_{xx}, \quad \sigma_{zz} = \rho g H \tilde{\sigma}_{zz}, \quad \sigma_{xz} = \varepsilon^\gamma \rho g H \tilde{\sigma}_{xz}, \quad 0 < \gamma < 1. \quad (2.29)$$

Note that the classical choice for the constant relating the normal component of the stress tensor to the shear component would be μ . However μ is not constant and depends on the flow variables. Therefore a constant γ is introduced, which relates the maximum value of the friction-coefficient to the aspect-ratio ε . First the non-dimensional quantities Δ^s, Δ^b and $\mathbf{n}^s, \mathbf{n}^b$ become a function of the non-dimensional variables:

$$\mathbf{n}^s = (\Delta^s)^{-1} \left(-\frac{H}{L} \frac{\partial \tilde{s}}{\partial \tilde{x}} \mathbf{e}_x + \mathbf{e}_z \right) = (\Delta^s)^{-1} \left(-\varepsilon \frac{\partial \tilde{s}}{\partial \tilde{x}} \mathbf{e}_x + \mathbf{e}_z \right), \quad (2.30)$$

$$\mathbf{n}^b = (\Delta^b)^{-1} \left(\frac{H}{L} \frac{\partial \tilde{b}}{\partial \tilde{x}} \mathbf{e}_x - \mathbf{e}_z \right) = (\Delta^b)^{-1} \left(\varepsilon \frac{\partial \tilde{b}}{\partial \tilde{x}} \mathbf{e}_x - \mathbf{e}_z \right), \quad (2.31)$$

$$\Delta^s = \sqrt{\left(\frac{H}{L} \frac{\partial \tilde{s}}{\partial \tilde{x}} \right)^2 + 1} = \sqrt{\left(\varepsilon \frac{\partial \tilde{s}}{\partial \tilde{x}} \right)^2 + 1}, \quad (2.32)$$

$$\Delta^b = \sqrt{\left(\frac{H}{L} \frac{\partial \tilde{b}}{\partial \tilde{x}} \right)^2 + 1} = \sqrt{\left(\varepsilon \frac{\partial \tilde{b}}{\partial \tilde{x}} \right)^2 + 1}. \quad (2.33)$$

Next, introducing the nondimensional quantities, the continuity equation (2.4) becomes:

$$\frac{\sqrt{Lg}}{L} \frac{\partial \tilde{u}}{\partial \tilde{x}} + \frac{\varepsilon \sqrt{Lg}}{H} \frac{\partial \tilde{w}}{\partial \tilde{z}} = \frac{\sqrt{Lg}}{L} \frac{\partial \tilde{u}}{\partial \tilde{x}} + \frac{\sqrt{Lg}}{L} \frac{\partial \tilde{w}}{\partial \tilde{z}} = \frac{\partial \tilde{u}}{\partial \tilde{x}} + \frac{\partial \tilde{w}}{\partial \tilde{z}} = 0. \quad (2.34)$$

Similarly the conservation of momentum (2.11) and (2.12) transforms in:

$$\frac{\partial \tilde{u}}{\partial \tilde{t}} + \frac{\partial \tilde{u}^2}{\partial \tilde{x}} + \frac{\partial \tilde{u}\tilde{w}}{\partial \tilde{z}} = \varepsilon \frac{\partial \tilde{\sigma}_{xx}}{\partial \tilde{x}} + \varepsilon^\gamma \frac{\partial \tilde{\sigma}_{xz}}{\partial \tilde{z}} + \sin \theta, \quad (2.35)$$

$$\varepsilon \left(\frac{\partial \tilde{w}}{\partial \tilde{t}} + \frac{\partial \tilde{w}^2}{\partial \tilde{z}} + \frac{\partial \tilde{u}\tilde{w}}{\partial \tilde{x}} \right) = \varepsilon^{1+\gamma} \frac{\partial \tilde{\sigma}_{xz}}{\partial \tilde{x}} + \frac{\partial \tilde{\sigma}_{zz}}{\partial \tilde{z}} - \cos \theta. \quad (2.36)$$

Next the boundary conditions are transformed, starting with the kinematic boundary conditions, (2.14) and (2.15):

$$\frac{\partial s}{\partial t} + u^s \frac{\partial s}{\partial x} - w^s = 0 \rightarrow \frac{\partial \tilde{s}}{\partial \tilde{t}} + \tilde{u}^s \frac{\partial \tilde{s}}{\partial \tilde{x}} - \tilde{w}^s = 0, \quad (2.37)$$

$$\frac{\partial b}{\partial t} + u^b \frac{\partial b}{\partial x} - w^b = 0 \rightarrow \frac{\partial \tilde{b}}{\partial \tilde{t}} + \tilde{u}^b \frac{\partial \tilde{b}}{\partial \tilde{x}} - \tilde{w}^b = 0. \quad (2.38)$$

At the free surface $\tilde{s}(\tilde{x})$, the two components of the free surface traction are both zero (using the definition of the normal in equation (2.24)):

$$\mathbf{t}^b = \sigma^s \cdot \mathbf{n}^s = \sigma^s \cdot (\Delta^s)^{-1} \left(-\frac{\partial s}{\partial x} \mathbf{e}_x + \mathbf{e}_z \right) = \mathbf{0}. \quad (2.39)$$

$$(2.40)$$

So the x and z -component (t_x^b and t_z^b) of the traction transform to:

$$t_x^b = -\sigma_{xx}^s \frac{\partial s}{\partial x} + \sigma_{xz}^s = 0 \text{ and } t_z^b = -\sigma_{xz}^s \frac{\partial s}{\partial x} + \sigma_{zz}^s = 0, \quad (2.41)$$

$$-\rho g H \tilde{\sigma}_{xx}^s \frac{H}{L} \frac{\partial \tilde{s}}{\partial \tilde{x}} + \varepsilon^\gamma \rho g H \tilde{\sigma}_{xz}^s = 0 \text{ and } -\rho g H \varepsilon^\gamma \tilde{\sigma}_{xz}^s \frac{H}{L} \frac{\partial \tilde{s}}{\partial \tilde{x}} + \rho g H \tilde{\sigma}_{zz}^s = 0, \quad (2.42)$$

$$-\varepsilon \tilde{\sigma}_{xx}^s \frac{\partial \tilde{s}}{\partial \tilde{x}} + \varepsilon^\gamma \tilde{\sigma}_{xz}^s = 0 \text{ and } -\varepsilon^{\gamma+1} \tilde{\sigma}_{xz}^s \frac{\partial \tilde{s}}{\partial \tilde{x}} + \tilde{\sigma}_{zz}^s = 0. \quad (2.43)$$

Repeating exactly the same steps, also the boundary condition for the traction at the base, equation (2.21) can be non-dimensionalised. The traction is split in a x - and z -component, and the relation for the normal vector at the base, equation (2.25) is substituted. Starting with the x -component of the traction:

$$\sigma_{xx}^b n_x^b + \sigma_{xz}^b n_z^b = (\mathbf{n}^b \cdot (\sigma^b \mathbf{n}^b)) \left(\mu \frac{u^b}{|\mathbf{u}^b|} + n_x^b \right), \quad (2.44)$$

$$\sigma_{xx}^b (\Delta^b)^{-1} \frac{\partial b}{\partial x} - \sigma_{xz}^b (\Delta^b)^{-1} = (\mathbf{n}^b \cdot (\sigma^b \mathbf{n}^b)) \left(\mu \frac{u^b}{|\mathbf{u}^b|} + (\Delta^b)^{-1} \frac{\partial b}{\partial x} \right), \quad (2.45)$$

$$\sigma_{xx}^b \frac{\partial b}{\partial x} - \sigma_{xz}^b = (\mathbf{n}^b \cdot (\sigma^b \mathbf{n}^b)) \left(\Delta^b \mu \frac{u^b}{|\mathbf{u}^b|} + \frac{\partial b}{\partial x} \right). \quad (2.46)$$

But now, non-dimensionalising $(\mathbf{n}^b \cdot (\sigma^b \mathbf{n}^b))$ is not straight forward. First the matrix vector products are written out:

$$\mathbf{n}^b \cdot (\sigma^b \mathbf{n}^b) = \mathbf{n}^b \cdot ((\sigma_{xx}^b n_x^b + \sigma_{xz}^b n_z^b) \mathbf{e}_x + (\sigma_{xz}^b n_x^b + \sigma_{zz}^b n_z^b) \mathbf{e}_z), \quad (2.47)$$

$$= (\sigma_{xx}^b n_x^b + \sigma_{xz}^b n_z^b) n_x^b + (\sigma_{xz}^b n_x^b + \sigma_{zz}^b n_z^b) n_z^b, \quad (2.48)$$

$$= \sigma_{xx}^b n_x^b n_x^b + 2\sigma_{xz}^b n_x^b n_z^b + \sigma_{zz}^b n_z^b n_z^b. \quad (2.49)$$

Substituting non-dimensional quantities gives:

$$n_x^b = (\Delta^b)^{-1} \varepsilon \frac{\partial \tilde{b}}{\partial \tilde{x}}, \quad n_z^b = -(\Delta^b)^{-1}, \quad \Delta^b = \sqrt{\left(\varepsilon \frac{\partial \tilde{b}}{\partial \tilde{x}} \right)^2 + 1}, \quad (2.50)$$

$$\mathbf{n}^b \cdot (\sigma^b \mathbf{n}^b) = \rho g H (\Delta^b)^{-2} \left(\tilde{\sigma}_{xx}^b \left(\varepsilon \frac{\partial \tilde{b}}{\partial \tilde{x}} \right)^2 - 2\varepsilon^{\gamma+1} \tilde{\sigma}_{xz}^b \frac{\partial \tilde{b}}{\partial \tilde{x}} + \tilde{\sigma}_{zz}^b \right). \quad (2.51)$$

Which can be written as:

$$\mathbf{n}^b \cdot (\sigma^b \mathbf{n}^b) = \rho g H (\Delta^b)^{-2} \tilde{\chi}^b, \text{ with: } \tilde{\chi}^b = \left(\tilde{\sigma}_{xx}^b \left(\varepsilon \frac{\partial \tilde{b}}{\partial \tilde{x}} \right)^2 - 2\varepsilon^{\gamma+1} \tilde{\sigma}_{xz}^b \frac{\partial \tilde{b}}{\partial \tilde{x}} + \tilde{\sigma}_{zz}^b \right). \quad (2.52)$$

In this way $\tilde{\chi}^b$ can be thought of as the non-dimensional component normal to the base of the traction on that base. Furthermore, the length of the velocity vector becomes:

$$|\mathbf{u}^b| = \sqrt{(u^b)^2 + (w^b)^2} = \sqrt{(\sqrt{Lg} \tilde{u}^b)^2 + (\varepsilon \sqrt{Lg} \tilde{w}^b)^2} = \sqrt{Lg} \sqrt{(\tilde{u}^b)^2 + (\varepsilon \tilde{w}^b)^2} \quad (2.53)$$

Now the basal traction, equation (2.46) can be non-dimensionalised :

$$\rho g H \tilde{\sigma}_{xx}^b \varepsilon \frac{\partial \tilde{b}}{\partial \tilde{x}} - \rho g H \varepsilon^\gamma \tilde{\sigma}_{xz}^b = (\rho g H (\Delta^b)^{-2} \tilde{\chi}^b) \left(\Delta^b \mu \frac{\sqrt{Lg} \tilde{u}^b}{\sqrt{Lg} \sqrt{(\tilde{u}^b)^2 + (\varepsilon \tilde{w}^b)^2}} + \varepsilon \frac{\partial \tilde{b}}{\partial \tilde{x}} \right) \quad (2.54)$$

$$\tilde{\sigma}_{xx}^b \varepsilon \frac{\partial \tilde{b}}{\partial \tilde{x}} - \varepsilon^\gamma \tilde{\sigma}_{xz}^b = ((\Delta^b)^{-2} \tilde{\chi}^b) \left(\Delta^b \mu \frac{\tilde{u}^b}{\sqrt{(\tilde{u}^b)^2 + (\varepsilon \tilde{w}^b)^2}} + \varepsilon \frac{\partial \tilde{b}}{\partial \tilde{x}} \right) \quad (2.55)$$

In exactly the same way also the z -component of the boundary condition for the traction at the basal surface (2.21) can be non-dimensionalised :

$$\sigma_{xz}^b n_x^b + \sigma_{zz}^b n_z^b = (\mathbf{n}^b \cdot (\sigma^b \mathbf{n}^b)) \left(\mu \frac{w^b}{|\mathbf{u}^b|} + n_z^b \right). \quad (2.56)$$

Becomes:

$$\tilde{\sigma}_{xz}^b \varepsilon^{\gamma+1} \frac{\partial \tilde{b}}{\partial \tilde{x}} - \tilde{\sigma}_{zz}^b = ((\Delta^b)^{-2} \tilde{\chi}^b) \left(\Delta^b \mu \frac{\varepsilon \tilde{w}^b}{\sqrt{(\tilde{u}^b)^2 + (\varepsilon \tilde{w}^b)^2}} - 1 \right). \quad (2.57)$$

2.1.4 Depth averaging

With the conservation equations and boundary conditions in non-dimensional form the next step can be applied: depth averaging. Depth averaged variables are defined as the variable integrated over the height, divided by that height:

$$\bar{f} = 1/h \int_b^s f dz \text{ with: } h = s - b. \quad (2.58)$$

Starting with depth averaging the non dimensional continuity equation, note that from now on the tildes are omitted:

$$\frac{1}{h} \int_b^s \frac{\partial u}{\partial x} + \frac{\partial w}{\partial z} dz = 0, \quad (2.59)$$

$$\int_b^s \frac{\partial u}{\partial x} + \frac{\partial w}{\partial z} dz = 0, \quad (2.60)$$

$$\int_b^s \frac{\partial u}{\partial x} dz + \left[w \right]_{z=b}^{z=s} = 0. \quad (2.61)$$

In which $[f]_{z=b}^{z=s} = f(s) - f(b)$. Next Leibnitz' rule is employed, to change the order of differentiation and integration on the first term:

$$\text{stressLeibnitz: } \frac{\partial}{\partial x} \int_b^s f dz = \int_b^s \frac{\partial f}{\partial x} dz + \left[f \frac{\partial z}{\partial x} \right]_{z=b(x)}^{z=s(x)}, \quad (2.62)$$

$$\frac{\partial}{\partial x} \int_b^s u dz - \left[u \frac{\partial z}{\partial x} \right]_{z=b}^{z=s} + \left[w \right]_{z=b}^{z=s} = 0. \quad (2.63)$$

The two terms in the brackets are combined, and from equation (2.58) one gets $\int_b^s u dz = h\bar{u}$:

$$\frac{\partial h\bar{u}}{\partial x} + \left[w - u \frac{\partial z}{\partial x} \right]_{z=b}^{z=s} = 0, \quad (2.64)$$

$$\frac{\partial h\bar{u}}{\partial x} + \left(w^s - u^s \frac{\partial s}{\partial x} \right) - \left(w^b - u^b \frac{\partial b}{\partial x} \right) = 0. \quad (2.65)$$

Substituting the kinematic boundary conditions for both the base and the surface (equation (2.38) and (2.37)) gives the depth averaged continuity equation:

$$\frac{\partial h\bar{u}}{\partial x} + \frac{\partial s}{\partial t} - \frac{\partial b}{\partial t} = 0, \quad (2.66)$$

$$\frac{\partial h\bar{u}}{\partial x} + \frac{\partial h}{\partial t} = 0. \quad (2.67)$$

In the same (but lengthier) fashion the momentum conservation equation in x -direction, equation (2.35) can be depth averaged (the pre-factor $1/h$ is already cancelled):

$$\int_b^s \frac{\partial u}{\partial t} + \frac{\partial u^2}{\partial x} + \frac{\partial uw}{\partial z} dz = \int_b^s \varepsilon \frac{\partial \sigma_{xx}}{\partial x} + \varepsilon^\gamma \frac{\partial \sigma_{xz}}{\partial z} + \sin \theta dz. \quad (2.68)$$

Each term is treated separately below:

$$\int_b^s \frac{\partial u}{\partial t} dz = \frac{\partial}{\partial t} \int_b^s u dz - \left[\frac{\partial z}{\partial t} u \right]_b^s = \frac{\partial h \bar{u}}{\partial t} - \left[\frac{\partial z}{\partial t} u \right]_b^s, \quad (2.69)$$

$$\int_b^s \frac{\partial u^2}{\partial x} dz = \frac{\partial}{\partial x} \int_b^s u^2 dz - \left[\frac{\partial z}{\partial x} u^2 \right]_b^s = \frac{\partial h \bar{u}^2}{\partial x} - \left[\frac{\partial z}{\partial x} u^2 \right]_b^s, \quad (2.70)$$

$$\int_b^s \frac{\partial uw}{\partial z} dz = \left[uw \right]_b^s, \quad (2.71)$$

$$\int_b^s \varepsilon \frac{\partial \sigma_{xx}}{\partial x} dz = \varepsilon \frac{\partial}{\partial x} \int_b^s \sigma_{xx} dz - \varepsilon \left[\frac{\partial z}{\partial x} \sigma_{xx} \right]_b^s = \varepsilon \frac{\partial h \bar{\sigma}_{xx}}{\partial x} - \varepsilon \left[\frac{\partial z}{\partial x} \sigma_{xx} \right]_b^s, \quad (2.72)$$

$$\int_b^s \varepsilon^\gamma \frac{\partial \sigma_{xz}}{\partial z} dz = \varepsilon^\gamma \left[\sigma_{xz} \right]_b^s, \quad (2.73)$$

$$\int_b^s \sin \theta dz = \sin \theta (s - b) = h \sin \theta. \quad (2.74)$$

Substituting the above terms back in (2.68) and rearranging one gets:

$$\frac{\partial h \bar{u}}{\partial t} + \frac{\partial h \bar{u}^2}{\partial x} + \left[uw - \frac{\partial z}{\partial t} u - \frac{\partial z}{\partial x} u^2 \right]_b^s = \varepsilon \frac{\partial h \bar{\sigma}_{xx}}{\partial x} + \left[\varepsilon^\gamma \sigma_{xz} - \varepsilon \frac{\partial z}{\partial x} \sigma_{xx} \right]_b^s + h \sin \theta, \quad (2.75)$$

$$\frac{\partial h \bar{u}}{\partial t} + \frac{\partial h \bar{u}^2}{\partial x} - \left[u \left(\frac{\partial z}{\partial t} + \frac{\partial z}{\partial x} u - w \right) \right]_b^s = \varepsilon \frac{\partial h \bar{\sigma}_{xx}}{\partial x} + \left[\varepsilon^\gamma \sigma_{xz} - \varepsilon \frac{\partial z}{\partial x} \sigma_{xx} \right]_b^s + h \sin \theta. \quad (2.76)$$

In the terms between the brackets the boundary conditions for the traction at the base and the surface (equations (2.55) & (2.43)) and the kinematic boundary conditions (equation (2.38) & (2.37)) can be recognised. Substituting those in gives:

$$\frac{\partial h \bar{u}}{\partial t} + \frac{\partial h \bar{u}^2}{\partial x} = \varepsilon \frac{\partial h \bar{\sigma}_{xx}}{\partial x} - ((\Delta^b)^{-2} \chi^b) \left(\Delta^b \mu \frac{\tilde{u}^b}{\sqrt{(\tilde{u}^b)^2 + (\varepsilon \tilde{w}^b)^2}} + \varepsilon \frac{\partial \tilde{b}}{\partial \tilde{x}} \right) + h \sin \theta. \quad (2.77)$$

Next the fact is used that for the systems considered $\varepsilon = H/L \ll 1$, and terms of order larger than ε are neglected. Note that it is assumed that $0 < \gamma < 1$. First the expression for χ^b , equation (2.52) is rewritten:

$$\chi^b = \left(\sigma_{xx}^b \left(\varepsilon \frac{\partial b}{\partial x} \right)^2 - 2\varepsilon^{\gamma+1} \sigma_{xz}^b \frac{\partial b}{\partial x} + \sigma_{zz}^b \right) = \sigma_{zz}^b + O(\varepsilon^{\gamma+1}). \quad (2.78)$$

Next the normalisation constants for the unit vectors $\Delta^{s,b}$ become:

$$\Delta^b = \sqrt{\left(\varepsilon \frac{\partial \tilde{b}}{\partial \tilde{x}} \right)^2 + 1} = 1 + O(\varepsilon), \quad (2.79)$$

$$\Delta^s = \sqrt{\left(\varepsilon \frac{\partial \tilde{s}}{\partial \tilde{x}} \right)^2 + 1} = 1 + O(\varepsilon). \quad (2.80)$$

Furthermore the fraction giving direction to the friction term simplifies, if it is assumed that $u(z) > 0$ throughout the whole depth the term can be written in depth averaged variables:

$$\frac{u^b}{\sqrt{(u^b)^2 + (\varepsilon w^b)^2}} = \frac{\bar{u}}{|\bar{u}|} + O(\varepsilon). \quad (2.81)$$

So, assuming $\mu = O(\varepsilon^\gamma)$, equation (2.77) becomes:

$$\frac{\partial h \bar{u}}{\partial t} + \frac{\partial h \bar{u}^2}{\partial x} = \varepsilon \frac{\partial h \bar{\sigma}_{xx}}{\partial x} - \sigma_{zz}^b \left(\mu \frac{\bar{u}}{|\bar{u}|} + \varepsilon \frac{\partial b}{\partial x} \right) + h \sin \theta + O(\varepsilon^{1+\gamma}). \quad (2.82)$$

Now the non-dimensional momentum conservation equation in z -direction (equation (2.36)) can be used to obtain a relation for σ_{zz} . Therefore it should be noted from (2.36) that the leading order behaviour for σ_{zz} is governed by:

$$\frac{\partial \sigma_{zz}}{\partial z} = \cos \theta + O(\varepsilon). \quad (2.83)$$

This can be integrated to get a relation for σ_{zz} :

$$\sigma_{zz} = z \cos(\theta) + C. \quad (2.84)$$

Using the zero traction boundary condition at the surface up to leading order (equation (2.43) becomes $\sigma_{zz}^s = 0$) gives:

$$\sigma_{zz} = (z - s) \cos \theta + O(\varepsilon), \quad (2.85)$$

$$\sigma_{zz}^b = -h \cos \theta + O(\varepsilon). \quad (2.86)$$

Which yields the lithostatic-pressure balance (up to leading order). So the momentum balance in x -direction becomes:

$$\frac{\partial h \bar{u}}{\partial t} + \frac{\partial h \bar{u}^2}{\partial x} = \varepsilon \frac{\partial h \bar{\sigma}_{xx}}{\partial x} + h(\sin \theta - \cos \theta \mu \frac{\bar{u}}{|\bar{u}|}) - \varepsilon h \cos \theta \frac{\partial b}{\partial x} + O(\varepsilon^{1+\gamma}). \quad (2.87)$$

Now recalling the non-dimensional, depth-averaged continuity equation ((2.67)):

$$\frac{\partial h}{\partial t} + \frac{\partial h \bar{u}}{\partial x} = 0. \quad (2.88)$$

It can be seen that there are two equations for five unknowns: $h, \bar{u}, \bar{u}^2, \mu, \bar{\sigma}_{xx}$. Therefore three closure-relations need to be defined to be able to (numerically) solve the set of equations. Firstly, a constitutive model is needed, relating the normal stresses in x and z directions. Similar to [27] a linear relation between the two will assumed, by means of a stress-ratio K :

$$\bar{\sigma}_{xx} = K \bar{\sigma}_{zz}. \quad (2.89)$$

Next \bar{u}^2 and \bar{u} are assumed to be related by a *shape factor* α :

$$\bar{u}^2 = \alpha \bar{u}. \quad (2.90)$$

Now the complete depth-averaged shallow-layer equations have become:

$$\frac{\partial h}{\partial t} + \frac{\partial h \bar{u}}{\partial x} = 0, \quad (2.91)$$

$$\frac{\partial h \bar{u}}{\partial t} + \frac{\partial}{\partial x}(h \alpha \bar{u}^2) = \varepsilon \frac{\partial h K \bar{\sigma}_{zz}}{\partial x} + h \left(\sin \theta - \cos \theta \mu \frac{\bar{u}}{|\bar{u}|} \right) - \varepsilon h \cos \theta \frac{\partial b}{\partial x} + O(\varepsilon^{1+\gamma}). \quad (2.92)$$

2.1.5 Segregation equation

The depth averaged shallow layer equations that are derived describe the behaviour of the flow as a whole, they do not however provide any mechanisms to describe the behaviour of the two different phases (large and small particles). Therefore a segregation model as described in [12] is needed. This model gives an extra segregation equation, derived from mixture theory, in which each phase individually has to satisfy mass and momentum balances. It therefore depends on the velocity field, which can be prescribed or constructed from the depth averaged shallow layer equations derived here. Given this velocity field the segregation equation describes the relative volume fraction of the two phases in space and time.

2.1.6 Friction coefficient μ

From the conservation of momentum in x and z -direction (equations (2.5) and (2.6)) it is possible to derive a steady state friction coefficient μ which relates the shear-stress σ_{xz} to the downward normal-stress σ_{zz} . Assuming a steady, uniform flow, such that all derivatives with respect to t and x become zero, and assuming $w = 0$, the momentum balance for x and z becomes:

$$\frac{\partial \sigma_{xz}}{\partial z} + \rho g \sin \theta = 0, \quad (2.93)$$

$$\frac{\partial \sigma_{zz}}{\partial z} - \rho g \cos \theta = 0. \quad (2.94)$$

Since ρ and g are constant, this can be integrated over z from z to infinity, giving the stress due to the weight of the flow above z :

$$\int_z^\infty \frac{\partial \sigma_{xz}}{\partial z'} + \rho g \sin \theta dz' = [\sigma_{xz}(z')]_{z'=z}^{z'=\infty} + \int_z^\infty \rho g \sin \theta dz' = 0, \quad (2.95)$$

$$\int_z^\infty \frac{\partial \sigma_{zz}}{\partial z'} - \rho g \cos \theta dz' = [\sigma_{zz}(z')]_{z'=z}^{z'=\infty} - \int_z^\infty \rho g \cos \theta dz' = 0. \quad (2.96)$$

Next, applying a constant density profile for $0 < z < h$ and the fact that the stress at infinity is zero:

$$[\sigma_{xz}(z')]_{z'=z}^{z'=\infty} + \int_z^\infty \rho g \sin \theta dz' = \sigma_{xz}(z) + (h-z)\rho g \sin \theta = 0, \quad (2.97)$$

$$[\sigma_{zz}(z')]_{z'=z}^{z'=\infty} - \int_z^\infty \rho g \cos \theta dz' = \sigma_{zz}(z) - (h-z)\rho g \cos \theta = 0. \quad (2.98)$$

Rearranging gives:

$$-\sigma_{xz}(z) = (h-z)\rho g \sin \theta \quad (2.99)$$

$$\sigma_{zz}(z) = (h-z)\rho g \cos \theta \quad (2.100)$$

The friction coefficient μ^m is given as the ratio between the downward normal and the shear stress:

$$\mu^m(z) = -\frac{\sigma_{xz}}{\sigma_{zz}}. \quad (2.101)$$

Which, given the assumption of steady, uniform flow is equal to (combining (2.99) and (2.100) with (2.101)):

$$\mu^m = -\frac{\sigma_{xz}}{\sigma_{zz}} = \frac{\sin \theta}{\cos \theta} = \tan \theta. \quad (2.102)$$

Since in section 2.5.2 a way of measuring the stress tensor for particle simulations will be presented, it is possible to measure the friction coefficient that a flow experiences. In the rest of this thesis this ‘measured’ friction coefficient will be denoted with an uppercase m : μ^m .

2.1.7 Closure relations

To be able to solve the depth averaged shallow layer equations K , α and a relation for the friction coefficient μ need to be defined. First of all, it is assumed that $K \approx 1$, which is true for low-shear shallow flows. For very rapid flow it is known that $K > 1$ [10]. Next α is addressed. Although not the focus-area of this research a few examples of different velocity profiles and their shape-factors will be given. If it is assumed that the x -velocity is a simple linear function of z (it is assumed that $b(x) = 0$, i.e the bottom is flat and located at $z = 0$):

$$u(z) = c_1 z + c_2 \quad (2.103)$$

Next $\overline{u^2}$ and \bar{u} can be computed:

$$\bar{u} = \frac{1}{h} \int_0^h u(z) dz = \frac{1}{h} \int_0^h c_1 z + c_2 dz = \frac{1}{h} \left[\frac{c_1}{2} z^2 + c_2 z \right]_0^h = \frac{c_1}{2} h + c_2, \quad (2.104)$$

$$(\bar{u})^2 = \frac{c_1^2}{4} h^2 + c_1 c_2 h + c_2^2, \quad (2.105)$$

$$\overline{u^2} = \frac{1}{h} \int_0^h u^2(z) dz = \frac{1}{h} \int_0^h c_1^2 z^2 + 2c_1 c_2 z + c_2^2 dz = \frac{1}{h} \left[\frac{c_1^2}{3} z^3 + c_1 c_2 z^2 + c_2^2 z \right]_0^h, \quad (2.106)$$

$$\overline{u^2} = \frac{c_1^2}{3} h^2 + \frac{2c_1 c_2}{2} h + c_2^2. \quad (2.107)$$

So the shape factor α becomes:

$$\alpha = \frac{\overline{u^2}}{(\bar{u})^2} = \frac{\frac{c_1^2}{3} h^2 + \frac{2c_1 c_2}{2} h + c_2^2}{\frac{c_1^2}{4} h^2 + c_1 c_2 h + c_2^2} = 1 + \frac{1}{3} \frac{\left(\frac{c_1 h}{2} \right)^2}{\left(\frac{c_1 h}{2} + c_2 \right)^2} \in [1, 4/3] \text{ for } c_1, c_2 > 0. \quad (2.108)$$

First considering the simplest case, a plug-flow with uniform velocity:

$$\text{Plug flow: } u(z) = c_2 \text{ with: } c_1 = 0. \quad (2.109)$$

This gives the trivial solution:

$$\alpha_{plug} = \frac{c_2^2}{c_2^2} = 1. \quad (2.110)$$

Next, a linear velocity profile with $u(z=0) = 0$ would give:

$$\text{Linear velocity profile: } u(z) = c_1 z \text{ with: } c_2 = 0, \quad (2.111)$$

$$\alpha = \frac{\frac{c_1^2}{3} h^2}{\frac{c_1^2}{4} h^2} = \frac{4}{3}. \quad (2.112)$$

Finally, a realistic (for shallow granular avalanches) Bagnold[1] flow profile, which scales the velocity with $z^{3/2}$ (the more lengthy derivation has been omitted) gives:

$$\text{Bagnold flow: } u(z) = c_1 \left(h^{3/2} - (h-z)^{3/2} \right), \quad (2.113)$$

$$\alpha = 5/4. \quad (2.114)$$

Given these two relations for α and K the only missing link is the friction coefficient μ , and its determination is the main focus of this thesis. In the next chapter an existing closure for μ will be discussed, and how it can be applied to bi-dispersed flows.

2.2 Closure laws in terms of h_{stop}

For the closure of the depth averaged shallow layer equations a relation for the friction coefficient μ is needed. Originally this friction coefficient was taken to behave Coulomb-like, which relates the friction coefficient to the tangent of the internal friction angle δ : $\mu = \tan(\delta)$. This however would mean that steady flow is only possible at one chute angle, being the internal friction angle (δ), at higher inclinations the flow would accelerate indefinitely, at lower inclinations the flow would arrest. In experiments however steady flows are observed over a range of angles. Therefore, Forterre and Pouliquen [7] investigated this flow-range. In the experiments they measured the minimum flow height h_{stop} of the particles versus the chute inclination θ . A lower height would cause the flow to arrest. This h_{stop} was fitted with equation (2.115):

$$h_{stop} = A \cdot d \cdot \frac{\tan(\delta_2) - \tan(\theta)}{\tan(\theta) - \tan(\delta_1)}, \quad \delta_1 < \theta < \delta_2. \quad (2.115)$$

In equation (2.115) δ_1 is the minimum flow angle, a lower chute-angle would cause the flow to arrest, independent of the height. Next, δ_2 is the angle above which no flow arrests, also independent of the flow height h . Furthermore d is a characteristic particle diameter and A a characteristic dimensionless length scale. Now the h_{stop} curve separates the arresting regime from the flowing regime. So for $h < h_{stop}$ the flow arrests, and for $h > h_{stop}$ and $\delta_1 < \theta < \delta_2$ flow is possible. An example h_{stop} -curve is plotted in figure 2.2, in which the two phases (arresting- and non-arresting flow) are indicated.

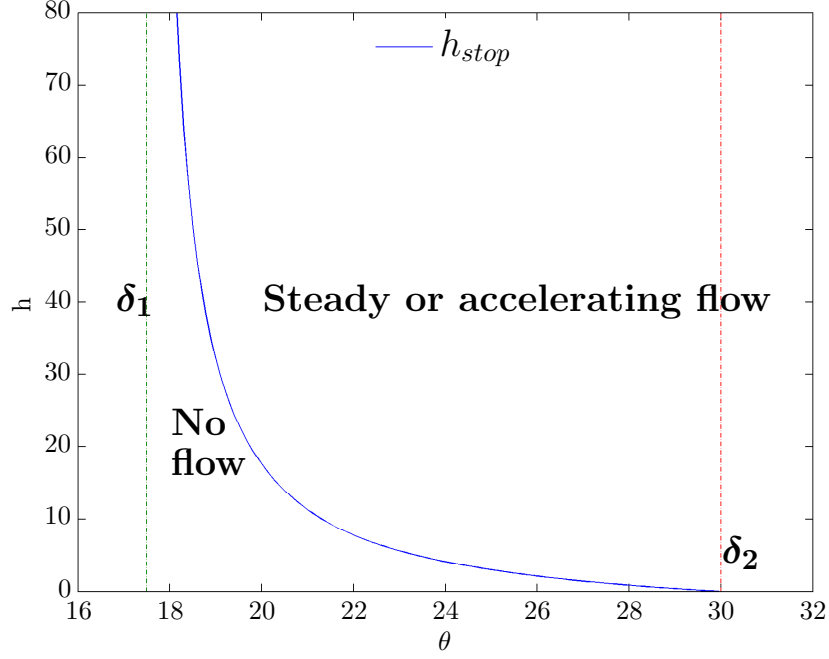


Figure 2.2: Flow phase diagram example

Given this h_{stop} curve it was found in [16] that for mono-dispersed flows, steady flow is possible at a Froude number which is a linear function of the flow height scaled with $h_{stop}(\theta)$. The Froude number relates the depth-averaged flow velocity to the surface gravity-wave speed and is given by:

$$F = \frac{\bar{u}}{\sqrt{g \cos(\theta)h}}, \quad (2.116)$$

in which \bar{u} denotes the depth-averaged downslope velocity and g is the gravitational constant. The Froude number is similar to the Mach-number. It was found that for steady flows F relates linearly to h with:

$$F = \beta \frac{h}{h_{stop}(\theta)} - \gamma, \quad (2.117)$$

in which β and γ are fitting parameters independent of θ and particle size (for mono-dispersed flow). Note that originally Pouliquen assumed $\gamma = 0$, in ongoing research however it was found that the introduction of γ did improve the fit. Next, using $\mu = \tan(\theta)$ (for steady flow) it is possible to derive a closure law for the friction coefficient in terms of flow variables F and h . Starting with the fit for the h_{stop} -curve, equation (2.115), which can be rewritten:

$$\tan(\theta)(h_{stop} + A * d) = h_{stop} \tan(\delta_1) + A * d * \tan(\delta_2), \quad (2.118)$$

$$\tan(\theta) = \frac{h_{stop} \tan(\delta_1)}{h_{stop} + A * d} + A * d * \frac{\tan(\delta_2)}{h_{stop} + A * d}. \quad (2.119)$$

Next $\frac{A * d \tan(\delta_1)}{h_{stop} + A * d}$ is added to the first term of the right-hand side, and subtracted from the last term:

$$\tan(\theta) = \frac{(h_{stop} + A * d) \tan(\delta_1)}{h_{stop} + A * d} + A * d * \frac{\tan(\delta_2) - \tan(\delta_1)}{h_{stop} + A * d}, \quad (2.120)$$

$$\tan(\theta) = \tan(\delta_1) + A * d * \frac{\tan(\delta_2) - \tan(\delta_1)}{h_{stop} + A * d}. \quad (2.121)$$

Finally the relation between h_{stop} and the Froude number (equation (2.117)) is used to get a relation

for the friction coefficient in terms of the flow variables F and h :

$$h_{stop}(\theta) = \frac{\beta h}{F + \gamma}, \quad (2.122)$$

$$\tan(\theta) = \mu(F, h) = \tan(\delta_1) + \frac{\tan(\delta_2) - \tan(\delta_1)}{\frac{\beta h}{A \cdot d(F + \gamma)} + 1}. \quad (2.123)$$

In this research this relation for μ based on the flow variables will be used, and compared to the measured friction coefficient defined as μ^m :

$$\mu^m = -\frac{\sigma_{xy}}{\sigma_{zz}}. \quad (2.124)$$

2.3 Bidispersity and segregation

The flows investigated are bi-dispersed, meaning there are particles of two different sizes present. Both the rate at which the segregation develops and the shape of the steady state segregation profile depend on this size ratio. First the relative size of the particles is characterised by the size ratio σ :

$$\sigma = \frac{r_{small}}{r_{large}}. \quad (2.125)$$

On a macroscopic scale the ratio between the total volume of both phases needs to be defined:

$$\eta = \frac{V_{large}}{V_{small} + V_{large}} = \frac{N_{large} \cdot \frac{4}{3}\pi r_{large}^3}{N_{large} \cdot \frac{4}{3}\pi r_{large}^3 + N_{small} \cdot \frac{4}{3}\pi \cdot r_{small}^3} = \frac{N_{large}}{N_{large} + N_{small} \cdot \sigma^3}. \quad (2.126)$$

If now the size ratio σ and the number of large particle N_{large} are set, the number of small particles is given by (rearranging (2.126)):

$$N_{small} = \frac{N_{large}}{\sigma^3} \frac{1 - \eta}{\eta}. \quad (2.127)$$

Note that the definition of σ originates from the paper by Savage and Lun [20], but since this convention only allows for values between zero and unity, the inverse of this ratio is used most of the time, in line with the paper by Thornton *et al* [23]. Furthermore, to be able to compare simulations, spatial coordinates are non-dimensionalised with a particle diameter, similarly as in [27]. However, since both large and small particles are present, in this case the large particle diameter is used to nondimensionalise the system. So in non-dimensional units the large particles have unity diameter.

An important factor in this work is to establish whether flows are in the steady state. For mono-dispersed flow one could simply look at the kinetic energy, if the total kinetic energy of the flow converges to a steady value over time the flow has reached its steady state. Dealing with bi-dispersed flow however it is important to check that the segregation profile has reached its steady shape as well. As a homogeneously mixed (or any other mixture differing from the steady concentration profile) flow will flow over time, a segregation profile will develop in which the small particles percolate down and the large particles are squeezed to the top of the flow. However, this would after some time result in perfectly segregated flows, which is not observed in experiments, where there is always a *mixing region* between the two phases. This mixing is due to simple diffusion, a result of the movement of the particles. Therefore the shape of the steady segregation profile depends on the amount of diffusion versus the amount of segregation present. Since there are only particles of two different sizes present, it is relatively easy to characterise the state of the segregation compared to poly-dispersed flows with a continuous distribution of particles sizes. This is done by taking the ratio of the z -coordinate of the centre of mass (COM) of both the large and the small phase:

$$S = \frac{COM_{small}}{COM_{large}}. \quad (2.128)$$

First it should be noted that for completely segregated flow (i.e two completely pure layers) the fraction of the flow-height occupied by the two separate phases is a function of η :

$$h_l = \eta h, \quad (2.129)$$

$$h_s = (1 - \eta)h. \quad (2.130)$$

Now since it is known that the large phase is on top of the small phases, it is possible to derive relations for the COM of the small phase and that of the large phase in terms of η and the height h (note, this only holds for two pure phases):

$$COM_{small} = h_s/2 = (1 - \eta)\frac{h}{2}, \quad (2.131)$$

$$COM_{large} = h - h_l/2 = (1 - \eta/2)h. \quad (2.132)$$

Such that when $\eta = 1/2$, i.e $V_{small} = V_{large}$, S becomes:

$$S = \frac{(1 - \eta)\frac{h}{2}}{(1 - \eta/2)h} = \frac{\frac{h}{4}}{\frac{3}{4}h} = 1/3. \quad (2.133)$$

As mentioned however, there will always be diffusion causing S to increase. E.g for completely *mixed* flow S becomes:

$$S = \frac{\frac{1}{2}h}{\frac{1}{2}h} = 1. \quad (2.134)$$

And finally, for *inversely graded* flow (i.e large particles at the bottom, small particles at the top of the flow) and again $\eta = 1/2$ S becomes:

$$S = \frac{3/4}{1/4} = 3 \quad (2.135)$$

That being said, the focus of this research is on the derivation of a closure law for the friction coefficient μ . This friction coefficient will depend on both the (local) volume ratio η and the particle size ratio σ . The developing avalanches considered in this research however will have a constant σ (there will be only two particle sizes in each system), so the objective is to compute the friction coefficient as a function of the local volume ratio η in the flow. Since the flowrule for $\mu(F, h)$ (equation (2.123)) depends on h_{stop} and the Froude flowrule fit (which gives the β and γ from equation (2.117)), both h_{stop} and $F(\frac{h}{h_{stop}})$ need to be fitted for every η . This of course is not feasible, since η is a continuous variable. Therefore when the friction coefficient is needed for a specific η for which the flowrule data is not directly available, it will be computed as the linear weighted average of $\mu(F, h)$ for the two closest η^i values (below and above η) for which there is flowrule data. Let the superscript η denote the flowrule being computed for that specific η , i.e $\mu^{\eta_0}(F, h)$ is the friction coefficient for a flow with volume ratio η_0 , and let η be a volume ratio for which there is no flowrule data, with η_0 and η_1 being the two closest volume fraction ratios for which there is flowrule data, such that $\eta_0 < \eta < \eta_1$. Then the linearly weighted friction coefficient for η is given as:

$$\mu(F, h, \eta) = \frac{\eta_1 - \eta}{\eta_1 - \eta_0} \mu^{\eta_0}(F, h) + \frac{\eta - \eta_0}{\eta_1 - \eta_0} \mu^{\eta_1}(F, h). \quad (2.136)$$

Given this definition, for $\eta = \eta_1$, one gets μ^{η_1} , for $\eta = \eta_0$ one gets μ^{η_0} and for any η in between a weighted average of μ^{η_0} and μ^{η_1} is returned.

2.4 Discrete Particle Method

To obtain insight in real granular flows is in general extremely difficult. For example, measuring a simple velocity profile throughout the flow depth is a tremendous challenge. Using transparent walls, it is possible to measure velocity directly at the wall, but then the wall has a large effect on the flow properties. Therefore, numerical simulations are used, which allow for much easier extraction of data. These Discrete Particle Method (DPM) simulations will be performed in MercuryDPM [26, 24], an open-source DPM solver developed at the University of Twente. The particle interaction forces are determined by a linear spring-dashpot model [4] coupled with a frictional sliding force [14]. Given the total force on each particle, this subsequently allows for the integration of Newton's equations of motion in time to obtain trajectories for the particles. After these simulations are performed the results (particle positions, velocities and interaction forces) will be *coarse grained* to obtain macroscopic fields for quantities like velocity, stress and density. In this section DPM will be treated in more detail, and contact-laws and coarse graining methods used will be discussed.

2.4.1 Contact laws

In this section the contact-properties of the particles will be discussed. All particles are assumed to be spherical and soft. This way a particle accelerates in translational and rotational degrees of freedom (DOF) due to the total force and total torque acting on a particle respectively.

Symbol	Description
r_i	Radius of particle i
r_l	Radius of the large particles
r_s	Radius of the small particles
d_l	Diameter of the large particles
d_s	Diameter of the small particles
N	Total number of particles
N_{large}	Number of large particles
N_{small}	Number of small particles
\mathbf{r}_i	Position vector of particle i
$\boldsymbol{\omega}_i$	Angular velocity vector of particle i
\mathbf{v}_i	Velocity vector of particle i
m_i	Particle mass
I_i	Particle moment inertia
$\hat{\mathbf{n}}_{ij}$	Unit normal pointing from particle j to i
\mathbf{f}_i	Total force acting on particle i
\mathbf{f}_{ij}	Force acting on particle i resulting from the collision with particle j
\mathbf{f}_{ij}^n	Normal component of \mathbf{f}_{ij} with respect to $\hat{\mathbf{n}}_{ij}$
\mathbf{f}_{ij}^t	Tangential component of \mathbf{f}_{ij} with respect to $\hat{\mathbf{n}}_{ij}$
\mathbf{q}_i	Torque acting on particle i
\mathbf{g}	Gravitational acceleration
\mathbf{b}_{ij}	Branch vector, pointing from particle i to the <i>contact point</i> with particle j
$k^{n,t}$	Normal or tangential spring stiffness
$\gamma^{n,t}$	Normal or tangential dissipation
μ^p	Particle contact friction coefficient
δ_{ij}^n	Normal overlap between particle i and j
$\boldsymbol{\delta}_{ij}^t$	Tangential displacement vector between particle i and j

Table 2.1: Symbol table

The meaning of all symbols used can be found in table 2.1 ; furthermore a single index denotes a property of particle i , e.g particle mass m_i . A double index denotes a relative quantity $\mathbf{v}_{ij} = \mathbf{v}_i - \mathbf{v}_j$, unless defined otherwise. Given a pair of two particles i and j , the relative distance vector is given by:

$$\mathbf{r}_{ij} = \mathbf{r}_i - \mathbf{r}_j. \quad (2.137)$$

The length of this vector is the scalar distance between the two particles:

$$r_{ij} = |\mathbf{r}_{ij}|. \quad (2.138)$$

If \mathbf{r}_{ij} is normalised with r_{ij} , one gets the unit normal pointing from particle j to i :

$$\hat{\mathbf{n}}_{ij} = \frac{\mathbf{r}_{ij}}{r_{ij}}. \quad (2.139)$$

To check whether particles are in contact the (normal) *overlap* is defined as:

$$\delta_{ij}^n = \max(0, r_i + r_j - r_{ij}). \quad (2.140)$$

Particle i and j are in contact if $\delta_{ij}^n > 0$. Next the force \mathbf{f}_{ij} is defined to be the force acting on particle i due to the collision with particle j , and in general it can be decomposed in a tangential and normal component (relative to unit normal $\hat{\mathbf{n}}_{ij}$):

$$\mathbf{f}_{ij} = \mathbf{f}_{ij}^n + \mathbf{f}_{ij}^t. \quad (2.141)$$

Considered are elastic, dissipative and frictional contact forces (no adhesion or long-range interaction forces), thus particle pairs only interact if they are in contact. So for the normal direction, given a damping constant γ^n and spring stiffness k^n the normal force component \mathbf{f}_{ij}^n is given by:

$$\mathbf{f}_{ij}^n = k^n \delta_{ij}^n \hat{\mathbf{n}}_{ij} - \gamma^n \mathbf{v}_{ij}^n. \quad (2.142)$$

In which \mathbf{v}_{ij}^n is the normal component of the relative velocity vector $\mathbf{v}_{ij} = \mathbf{v}_i - \mathbf{v}_j$:

$$\mathbf{v}_{ij}^n = (\mathbf{v}_{ij} \cdot \hat{\mathbf{n}}_{ij}) \hat{\mathbf{n}}_{ij}. \quad (2.143)$$

Although in the DPM simulations the particles are assumed to be smooth and spherical, in general every real particle will have some surface roughness. This causes particles in contact to resist relative tangential displacement at the contact. To model this behaviour a tangential spring and dashpot are introduced. Similar as with the normal force the tangential force consists of an elastic and a dissipative part:

$$\mathbf{f}_{ij}^t = -k^t \boldsymbol{\delta}_{ij}^t - \gamma^t \mathbf{v}_{ij}^t. \quad (2.144)$$

First, the relative tangential surface velocity at the contact point \mathbf{v}_{ij}^t is given as the relative velocity minus its normal component, plus the contributions due to the angular velocity of both particles:

$$\mathbf{v}_{ij}^t = \mathbf{v}_{ij} - \mathbf{v}_{ij}^n + \mathbf{b}_{ij} \times \boldsymbol{\omega}_i - \mathbf{b}_{ji} \times \boldsymbol{\omega}_j. \quad (2.145)$$

with $\boldsymbol{\omega}_i$ being the angular velocity of particle i , and \mathbf{b}_{ij} the branch vector from the centre of particle i to the contact point:

$$\mathbf{b}_{ij} = -(r_i - \delta_{ij}^n/2) \hat{\mathbf{n}}_{ij}, \quad (2.146)$$

The tangential displacement is slightly more complicated compared to the normal displacement, since it cannot be computed directly from particle positions and sizes. Instead, the tangential displacement is set to zero the moment two particles first touch, and its value is updated every timestep as the contact endures, given the relative tangential velocity of the particles. This is described by the simple ODE:

$$\frac{d\boldsymbol{\delta}_{ij}^t}{dt} = \mathbf{v}_{ij}^t - \frac{(\boldsymbol{\delta}_{ij}^t \cdot \mathbf{v}_{ij}) \hat{\mathbf{n}}_{ij}}{r_{ij}}. \quad (2.147)$$

Since the last term in equation (2.147) is perpendicular to the tangential direction it has no contribution to the magnitude of the tangential displacement, it only rotates it to keep it tangential. This however would allow two particles in contact to ‘wind up’ the tangential spring infinitely, which is not physical. Real particles will start slipping when the ratio of the tangential and normal force becomes larger than the particle contact friction coefficient, μ^p . Therefore a yield criterion for the tangential spring is used: the moment that $|\mathbf{f}_{ij}^t| > \mu^p |\mathbf{f}_{ij}^n|$ the magnitude of the tangential displacement $|\boldsymbol{\delta}_{ij}^t|$ is truncated such that the yield criterion $|\mathbf{f}_{ij}^t| = \mu^p |\mathbf{f}_{ij}^n|$ is satisfied. Now, with the force exerted by particle j on particle

i defined, one can construct the total force \mathbf{f}_i (where gravitational acceleration is included as a body force) and torque \mathbf{q}_i on particle i :

$$\mathbf{f}_i = m_i \mathbf{g} + \sum_{j=1, j \neq i}^N \mathbf{f}_{ij}, \quad (2.148)$$

$$\mathbf{q}_i = \sum_{j=1, j \neq i}^N \mathbf{b}_{ij} \times \mathbf{f}_{ij}. \quad (2.149)$$

Finally, Newton's second law is used to describe the rotational and translational degrees of freedom for particle i as a result of the forces and torques acting on it:

$$m_i \frac{d^2 \mathbf{r}_i}{dt^2} = \mathbf{f}_i, \quad (2.150)$$

$$I_i \frac{d\boldsymbol{\omega}_i}{dt} = \mathbf{q}_i. \quad (2.151)$$

2.4.2 Contact laws for bi-dispersed flows

Since this thesis focuses on bidispersed flows it is important to define how the two species differ from each other. In this research the focus is on size-segregation, therefore the goal is to make the two species as equal as possible in every aspect other than their size. Like stated in the section on contact laws 2.4.1, there are several particle properties which determine the way two particles in contact behave. In the contact model used there are two key quantities defining the contact behaviour during a collinear collision, being the collision time t_c and the restitution coefficient e . The collision time is the duration of a normal (collinear) collision, and the restitution coefficient gives the ratio of the (normal) velocities of the particles before and after the collision. Both depend on the normal contact stiffness k^n , the reduced particle mass m_{ij} and the amount of damping applied γ^n . As described in [14] these quantities are given by:

$$t_c = \frac{\pi}{\sqrt{\frac{k^n}{m_{ij}} - \left(\frac{\gamma^n}{2m_{ij}}\right)^2}}, \quad (2.152)$$

$$e = \exp\left(-\frac{\gamma^n}{2m_{ij}} t_c\right), \quad (2.153)$$

$$\text{Where: } m_{ij} = \frac{m_i m_j}{m_i + m_j}. \quad (2.154)$$

Next to the collisional timescale there is another important timescale to consider, being the gravitational timescale t_g . This t_g denotes the time it takes a particle to fall down its own diameter due to gravity:

$$t_g = \sqrt{\frac{d}{g}}. \quad (2.155)$$

Furthermore, it is important to note that these stiffness, reduced mass and damping variables are properties of the *contact*, and not of the particle itself. In a bi-dispersed system there are three types of contacts, being *small-small*, *large-large* and *large-small*. For all contacts the spring-constant and damping have to be defined, both in tangential and normal directions. First for the *small-small* and *large-large* contacts. The particle properties are set such that a 1D system with mono-dispersed particles of either size would behave the same dynamically. The 1D equation of motion for a single particle i is given by (only normal contacts possible):

$$\ddot{x} - \sum_j \frac{k_i^n}{m_i} \left(x_{ij} - \frac{d_i + d_j}{2}\right) + \frac{\gamma_i^n}{m_i} \dot{x}_{ij} + g. \quad (2.156)$$

Here j iterates over all particles in contact with particle i , note that the double indices indicate relative quantities, i.e $x_{ij} = x_i - x_j$. Then dimensionless quantities for distance and time are defined in relation

to the particle size and the gravitational timescale:

$$\begin{aligned} x_i &= d_i \tilde{x}_i, \\ t &= \sqrt{\frac{d_i}{g}} \tilde{t}. \end{aligned}$$

Substituting this in the equation of motion:

$$\frac{\partial^2(d_i \tilde{x}_i)}{\partial \left(\sqrt{\frac{d_i}{g}} \tilde{t}\right)^2} - \sum_j \frac{k_i^n}{m_i} \left(d_i \tilde{x}_{ij} - \frac{d_i + d_j}{2}\right) + \frac{\gamma_i^n}{m_i} \frac{\partial d_i \tilde{x}_i}{\partial \sqrt{\frac{d_i}{g}} \tilde{t}} + g. \quad (2.157)$$

If one now assumes a mono-dispersed system it is possible to rewrite (using that for mono-dispersed $\frac{d_i + d_j}{2} = d_j = d_i$):

$$\frac{\partial^2 \tilde{x}_i}{\partial \tilde{t}^2} - \sum_j \frac{d_i k_i^n}{g m_i} (\tilde{x}_{ij} - 1) + \frac{\gamma_i^n}{m_i} \sqrt{\frac{d_i}{g}} \frac{\partial \tilde{x}_i}{\partial \tilde{t}} + 1. \quad (2.158)$$

So to make two systems behave the same, one has to make sure that this equation is identical for both systems. For two systems, one with large particles of diameter d_l and one with small particles of diameter d_s this gives relations for the spring constants k_l and k_s , and the damping coefficients γ_l and γ_s :

$$\frac{d_l k_l^n}{g m_l} = \frac{d_s k_s^n}{g m_s} \rightarrow \frac{k_l^n}{m_l} = \sigma \frac{k_s^n}{m_s}, \quad (2.159)$$

$$\frac{\gamma_l^n}{m_l} \sqrt{\frac{d_l}{g}} = \frac{\gamma_s^n}{m_s} \sqrt{\frac{d_s}{g}} \rightarrow \frac{\gamma_l^n}{m_l} = \sqrt{\sigma} \frac{\gamma_s^n}{m_s}. \quad (2.160)$$

Or in terms of the collision time t_c and restitution coefficient e :

$$t_c^l = \frac{\pi}{\sqrt{\frac{2k_l^n}{m_l} - \left(\frac{\gamma_l^n}{m_l}\right)^2}} = \frac{\pi}{\sqrt{\sigma \frac{2k_s^n}{m_s} - \left(\sqrt{\sigma} \frac{\gamma_s^n}{m_s}\right)^2}} = \sqrt{\sigma^{-1}} t_c^s, \quad (2.161)$$

$$e^l = \exp\left(\frac{-\gamma_l^n}{m_l} t_c^l\right) = \exp\left(\frac{-\gamma_s^n}{m_s} \sqrt{\sigma} t_c^l\right) = \exp\left(\frac{-\gamma_s^n}{m_s} t_c^s\right) = e^s. \quad (2.162)$$

In the bi-dispersed simulations the variables are non-dimensionalised with the diameter of the large particles:

$$x_i = d_l \tilde{x}_i, \quad (2.163)$$

$$t = \sqrt{\frac{d_l}{g}} \tilde{t}. \quad (2.164)$$

With the equations above it is possible to compute the properties for the small particles that will make them behave the same as the large particles, but at a different time and length-scale:

$$k_s^n = \sigma^{-1} \frac{m_s}{m_l} k_l^n, \quad (2.165)$$

$$\gamma_s^n = \frac{m_s}{m_l} \sqrt{\sigma^{-1}} \gamma_l^n. \quad (2.166)$$

Finally also a spring stiffness and damping coefficient have to be assigned for the mixed collisions. Therefore one should note that it is necessary to keep the restitution coefficient as well as the ratio between the gravitational time and the collision time constant for all collisions:

$$e^s = e^l = e^{ls}, \quad (2.167)$$

$$\frac{\sqrt{\frac{d_l}{g}}}{t_c^l} = \frac{\sqrt{\frac{d_s}{g}}}{t_c^s} = \frac{\sqrt{\frac{d_{ls}}{g}}}{t_c^{ls}}. \quad (2.168)$$

To complete the equations d_{ls} needs to be defined (then it is possible to compute t_c^{ls} and solve for k_{ls} and γ_{ls}). The choice for d_{ls} is made based on a geometrical argument. The gravitational timescale represents the time it takes for a particle to fall its own diameter given a certain gravitational acceleration g . For an agglomerate of a large and a small particle, the average diameter is:

$$d_{ls} = \frac{d_l + d_s}{2}. \quad (2.169)$$

This gives t_c^{ls} :

$$t_c^{ls} = t_c^l \frac{\sqrt{\frac{d_{ls}}{g}}}{\sqrt{\frac{d_l}{g}}}. \quad (2.170)$$

To keep e constant for all types of collisions e_{ls} needs to satisfy:

$$e_{ls} = \exp\left(\frac{-\gamma_{ls}^n t_c^{ls}}{2m_{ls}}\right) = e_l = \exp\left(\frac{-\gamma_l^n t_c^l}{m_l}\right), \quad (2.171)$$

$$\gamma_{ls}^n = 2 \frac{m_{ls}}{m_l} \frac{t_c^l}{t_c^{ls}} \gamma_l^n. \quad (2.172)$$

Finally it is also possible solve for k_{ls} :

$$t_c^{ls} = \frac{\pi}{\sqrt{\frac{k_{ls}^n}{m_{ls}} - \left(\frac{\gamma_{ls}^n}{2m_{ls}}\right)^2}}, \quad (2.173)$$

$$\frac{k_{ls}^n}{m_{ls}} - \left(\frac{\gamma_{ls}^n}{2m_{ls}}\right)^2 = \left(\frac{\pi}{t_c^{ls}}\right)^2, \quad (2.174)$$

$$k_{ls}^n = m_{ls} \left(\left(\frac{\pi}{t_c^{ls}}\right)^2 + \left(\frac{\gamma_{ls}^n}{2m_{ls}}\right)^2 \right). \quad (2.175)$$

Note however that this is not a unique choice (we for example could also set $d_{ls} = \frac{d_l d_s}{d_l + d_s}$), therefore the influence of these *mixed-contact* properties will be further investigated in 3.2.4.

2.4.3 Time integration

The time-integration of the equations of motion in Mercury DPM is done using a Velocity Verlet scheme, which is second order accurate in time and has a constant time-increment Δt . The Velocity Verlet scheme has the advantage that it computes velocities directly, which are needed to compute the forces due to damping between particles. First, the half-step velocity is computed from a simple second order Taylor expansion:

$$\dot{\mathbf{r}}_i(t + \Delta t/2) = \dot{\mathbf{r}}_i(t) + \frac{1}{2} \ddot{\mathbf{r}}_i(t) \Delta t + O(\Delta t^2) \quad (2.176)$$

Next, the new particle positions are computed:

$$\mathbf{r}_i(t + \Delta t) = \mathbf{r}_i(t) + \dot{\mathbf{r}}_i(t) \Delta t + \frac{1}{2} \ddot{\mathbf{r}}_i(t) \Delta t^2 + O(\Delta t^3) \quad (2.177)$$

Then, the contact laws as defined in 2.4.1 are used to compute the forces acting on each particle, which depend on both the particle position and velocity. The total force acting on a particle then, given the mass of each particle, gives the particle acceleration. This can be used to compute the particle velocity at the new timestep:

$$\dot{\mathbf{r}}_i(t + \Delta t) = \dot{\mathbf{r}}_i(t + \frac{1}{2} \Delta t) + \frac{1}{2} \ddot{\mathbf{r}}_i(t + \Delta t) \Delta t + O(\Delta t^2) \quad (2.178)$$

2.5 Coarse graining

One of the key aspects of working with particle systems is the translation from the discrete particle based data to the continuum domain. To obtain macroscopic, continuous fields from the results of the DPM simulations a *coarse graining* method is used, which is thoroughly discussed by Goldhirsch [9], and extended by Weinhart *et al* [28]. In its most general form the coarse graining method *smooths* out discrete data over space. It will be used to construct continuum fields for quantities like velocity, density and stress, out of discrete particle quantities like particle-mass, velocity and collisional forces.

2.5.1 Theory

In statistical mechanics the microscopic mass density $\rho^{mic}(\mathbf{r}, t)$ at a point \mathbf{r} and time t is given by:

$$\rho^{mic}(\mathbf{r}, t) \equiv \sum_i^N m_i \delta(\mathbf{r} - \mathbf{r}_i(t)). \quad (2.179)$$

In which $\delta(\mathbf{r})$ is the Dirac-delta function, which ensures that the integral of the density over a volume gives the total mass in that volume, but it also makes ρ^{mic} a singular quantity. This singularity can be overcome by replacing the Dirac-delta with a non-singular ‘coarse graining’ or smoothing function:

$$\rho(\mathbf{r}, t) \equiv \sum_i^N m_i \phi(\mathbf{r} - \mathbf{r}_i(t)). \quad (2.180)$$

To satisfy the continuity equation the integral of $\phi(\mathbf{r})$ over the domain should be unity. Given that requirement there are still infinitely many possible coarse graining functions, but some are more convenient than others. In general a smoothing function can be characterised by a smoothing length or variance w . This w controls the amount of smoothing applied, and for the limit $w \rightarrow 0$ the microscopic definition is found again. For our simulations a simple Gaussian kernel will be used, which produces smooth fields:

$$\phi(\mathbf{r}) = \frac{1}{(\sqrt{2\pi}w)^3} \exp\left(-\frac{|\mathbf{r}|^2}{2w^2}\right). \quad (2.181)$$

The continuous fields of interest are mainly the density, velocity and stress fields. The first is defined above, and the velocity field is defined as the ratio of the momentum and density fields:

$$\textbf{Momentum: } \mathbf{p}(\mathbf{r}, t) \equiv \sum_i^N m_i \mathbf{v}_i \phi(\mathbf{r} - \mathbf{r}_i(t)), \quad (2.182)$$

$$\textbf{Velocity: } \mathbf{V}(\mathbf{r}, t) \equiv \frac{\mathbf{p}(\mathbf{r}, t)}{\rho(\mathbf{r}, t)}. \quad (2.183)$$

Although it may seem more natural to directly coarse grain the particle velocities (i.e $\mathbf{V}(\mathbf{r}, t) = \sum_i^N \mathbf{v}_i \phi(\mathbf{r} - \mathbf{r}_i(t))$) the above definition is guaranteed to satisfy the continuity equation. This can be seen if one writes down the temporal derivative of the density field:

$$\frac{\partial \rho(\mathbf{r}, t)}{\partial t} = \frac{\partial}{\partial t} \sum_i^N m_i \phi(\mathbf{r} - \mathbf{r}_i(t)) = \sum_i^N m_i \frac{\partial}{\partial t} \phi(\mathbf{r} - \mathbf{r}_i(t)). \quad (2.184)$$

This can be rewritten with the chain rule (note the use of Einstein’s summation convention for the β -index, denoting spatial directions x,y,z):

$$\frac{\partial \rho(\mathbf{r}, t)}{\partial t} = - \sum_i^N m_i \frac{\partial r_{i\beta}}{\partial t} \frac{\partial}{\partial r_\beta} \phi(\mathbf{r} - \mathbf{r}_i(t)). \quad (2.185)$$

Now the particle velocity, $\frac{\partial r_{i\beta}}{\partial t} = v_{i\beta}$ is substituted:

$$\frac{\partial \rho(\mathbf{r}, t)}{\partial t} = - \sum_i^N m_i v_{i\beta} \frac{\partial}{\partial r_\beta} \phi(\mathbf{r} - \mathbf{r}_i(t)). \quad (2.186)$$

Note that both m_i and $v_{i\beta}$ are particle properties, and do not depend on the spatial coordinate r_β , so the spatial derivative can be brought outside the summation, and the coarse grained momentum field, \mathbf{p} is recovered:

$$\frac{\partial \rho(\mathbf{r}, t)}{\partial t} = -\frac{\partial}{\partial r_\beta} \sum_i^N m_i v_{i\beta} \phi(\mathbf{r} - \mathbf{r}_i(t)) = -\frac{\partial p_\beta(\mathbf{r}, t)}{\partial r_\beta}. \quad (2.187)$$

Which gives the classical definition of the continuity equation if equation (2.183), $\mathbf{p}(\mathbf{r}, t) = \rho(\mathbf{r}, t)\mathbf{V}(\mathbf{r}, t)$ is substituted:

$$\frac{\partial \rho}{\partial t} = -\frac{\partial(\rho V_\beta)}{\partial r_\beta}. \quad (2.188)$$

2.5.2 Coarse grained stress tensor

The coarse graining method has an elegant, analytical definition of the stress tensor, which is thoroughly treated in [28]. Although the derivation will not be repeated here, it is important to note that the stress tensor has three different mechanisms which contribute to the stress-field. There is σ^b , the bulk contact stress, σ^w , the stress due to interactions with (fixed) wall-particles, and σ^k , the stress due to velocity fluctuations. It is thus assumed there are two types of particles, being N flowing particles $1, 2, \dots, N$ and K fixed base particles $N+1, N+2, \dots, N+K$. The stress tensor is then defined as the sum of its three components:

$$\sigma_{\alpha\beta} = \sigma_{\alpha\beta}^b + \sigma_{\alpha\beta}^w + \sigma_{\alpha\beta}^k. \quad (2.189)$$

The first, the contact stress for the bulk flow particles is given by:

$$\sigma_{\alpha\beta}^b = -\sum_{i=1}^N \sum_{j=i+1}^N f_{ij\alpha} r_{ij\beta} \int_0^1 \phi(\mathbf{r} - \mathbf{r}_i + s\mathbf{r}_{ij}) ds. \quad (2.190)$$

Note that as before, \mathbf{r} is the position of the coarse graining point, \mathbf{r}_i is the position of particle i , $\mathbf{r}_{ij} = \mathbf{r}_i - \mathbf{r}_j$, and finally the Greek indices α and β denote the component of the specific tensor or vector. Next, the stress due to interactions with the boundaries is modified in [28] compared to the definition in [9]. Instead of evaluating the stress along the line between the fixed particle and the flow particle, it evaluates the stress along the line from the flow particle to the contact point. Let the contact point between flow particle i and basal particle k be denoted as \mathbf{c}_{ik} , then the vector \mathbf{a}_{ik} pointing from flow particle i to the contact point is defined as:

$$\mathbf{a}_{ik} = \mathbf{r}_i - \mathbf{c}_{ik}. \quad (2.191)$$

So the definition of σ^w , the stress due to interactions with the fixed base particles becomes:

$$\sigma_{\alpha\beta}^w = -\sum_{i=1}^N \sum_{k=N+1}^{N+K} f_{ij\alpha} a_{ik\beta} \int_0^1 \phi(\mathbf{r} - \mathbf{r}_i + s\mathbf{a}_{ik}) ds. \quad (2.192)$$

Finally, there is also a contribution to the stress due to the particle velocities fluctuating with respect to the bulk velocity field. This contribution is given in terms of the fluctuating velocity \mathbf{v}'_i , which is defined as the difference between the velocity of particle i and the coarse grained velocity field (as defined in (2.183)) evaluated at the coarse graining point \mathbf{r} (note that the time dependence is omitted):

$$\mathbf{v}'_i = \mathbf{v}_i - \mathbf{V}(\mathbf{r}). \quad (2.193)$$

Given this definition the kinetic part of the stress tensor is defined as in [25]:

$$\sigma_{\alpha\beta}^k = -\sum_{i=1}^N m_i v'_{i\alpha} v'_{i\beta} \phi(\mathbf{r} - \mathbf{r}_i). \quad (2.194)$$

To underline the importance of including the kinetic stress contribution, a comparison has been made using a steady flow. The system consists of a periodic box as defined in 3.2, and hold 3.000 large and 6.000 small particles with a sizeratio $\sigma^{-1} = 1.26$. The friction coefficient μ^m is measured both with

and without including σ^k , and the results are depicted in 2.3. The flow is in steady state, and the chute has an inclination $\theta = 26^\circ$.

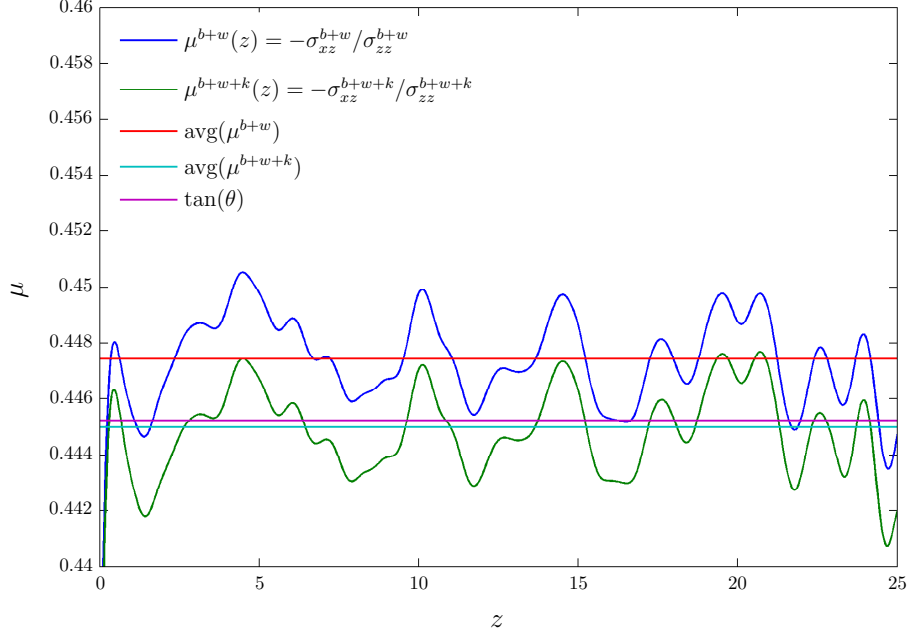


Figure 2.3: DPM results that are coarse grained with $w = 0.3$, showing $\mu^m = -\frac{\sigma_{xz}}{\sigma_{zz}}$ with and without including the kinetic stress. The red and purple curves are the averages of respectively the blue and green profiles.

Examining figure 2.3 it is clear that with the inclusion of the kinetic contribution to the stress tensor the measured friction coefficient μ^m is approaching the steady state value of $\mu = \tan(\theta)$ much more accurately. Therefore all coarse grained stress fields will include this kinetic contribution.

2.5.3 Spatial averaging

Since the flows considered in this work are always uniform in one or more directions it is possible to improve the quality of the coarse grained statistics by averaging over those directions. For instance, all flows considered are periodic in y -direction, so the y -dependence can be averaged out in the statistics. The coarse graining method as described in the previous section allows for a relatively simple analytical derivation of spatially averaged fields due to the usage of the Gaussian coarse graining kernel. Let for example the density field averaged in y -direction in the domain $y \in [y_0, y_1]$ be defined as:

$$\langle \rho(x, z, t) \rangle_y = \frac{1}{y_1 - y_0} \int_{-\infty}^{\infty} \rho(\mathbf{r}, t) dy = \frac{1}{y_1 - y_0} \int_{-\infty}^{\infty} \sum_i^N m_i \phi(\mathbf{r} - \mathbf{r}_i(t)) dy. \quad (2.195)$$

Note that since the coarse graining function can be non-zero throughout the entire domain (and the Gaussian indeed has this property) it is needed to integrate from minus infinity to plus infinity to satisfy mass conservation. This integral however is divided by the length of the averaging domain, being $y_1 - y_0$. Next ϕ is replaced with the Gaussian, and of course it is possible to write \mathbf{r} and \mathbf{r}_i explicitly in terms of x, y, z :

$$\langle \rho(x, z, t) \rangle_y = \frac{1}{y_1 - y_0} \int_{-\infty}^{\infty} \sum_{i=1}^N m_i \frac{1}{(\sqrt{2\pi}w)^3} \exp\left(-\frac{|\mathbf{r} - \mathbf{r}_i(t)|^2}{2w^2}\right) dy, \quad (2.196)$$

$$\langle \rho(x, z, t) \rangle_y = \frac{1}{y_1 - y_0} \int_{-\infty}^{\infty} \sum_{i=1}^N m_i \frac{1}{(\sqrt{2\pi}w)^3} \exp\left(-\frac{(x - x_i)^2 + (y - y_i)^2 + (z - z_i)^2}{2w^2}\right) dy. \quad (2.197)$$

Next the order of summation and integration can be switched and the terms not depending on y can be factored out:

$$\langle \rho(x, z, t) \rangle_y = \frac{1}{y_1 - y_0} \frac{1}{(\sqrt{2\pi}w)^3} \sum_{i=1}^N m_i \exp\left(-\frac{(x - x_i)^2 + (z - z_i)^2}{2w^2}\right) \int_{-\infty}^{\infty} \exp\left(-\frac{(y - y_i)^2}{2w^2}\right) dy. \quad (2.198)$$

The integral on the righthand side can be thought of as the surface of the one-dimensional (non normalised) Gaussian. It can be computed with a simple change of variable:

$$u(y) = \frac{y - y_i}{\sqrt{2}w}, \quad dy = \sqrt{2}w du, \quad (2.199)$$

$$\int_{-\infty}^{\infty} \exp\left(-\frac{(y - y_i)^2}{2w^2}\right) dy = \int_{u(-\infty)}^{u(\infty)} \exp(-u^2) \sqrt{2}w du = \sqrt{2}w \int_{-\infty}^{\infty} e^{-u^2} du. \quad (2.200)$$

This integral is known as the Gaussian Integral, and it is equal to $\sqrt{\pi}$, so the integral becomes:

$$\int_{-\infty}^{\infty} \exp\left(-\frac{(y - y_i)^2}{2w^2}\right) dy = \sqrt{2\pi}w. \quad (2.201)$$

Which can be plugged in (2.198):

$$\langle \rho(x, z, t) \rangle_y = \frac{1}{y_1 - y_0} \frac{1}{(\sqrt{2\pi}w)^3} \sum_{i=1}^N m_i \exp\left(-\frac{(x - x_i)^2 + (z - z_i)^2}{2w^2}\right) \sqrt{2\pi}w, \quad (2.202)$$

$$\langle \rho(x, z, t) \rangle_y = \frac{1}{y_1 - y_0} \frac{1}{(\sqrt{2\pi}w)^2} \sum_{i=1}^N m_i \exp\left(-\frac{(x - x_i)^2 + (z - z_i)^2}{2w^2}\right). \quad (2.203)$$

So in the end, the result of averaging out the y -direction is that the prefactor for the coarse grained density field is changed, and that the distance between the particle i and the point \mathbf{r} in the exponential is now calculated without including the y -direction. Since also flows which are uniform in the x -direction will be considered, often statistics averaged in both x - and y -directions are used. Being just a repetition of steps the entire derivation is not repeated, it can easily be seen that the density field averaged over both $x \in [x_0, x_1]$ and $y \in [y_0, y_1]$ is given by:

$$\langle \rho(z, t) \rangle_{xy} = \frac{1}{(y_1 - y_0)(x_1 - x_0)} \frac{1}{\sqrt{2\pi}w} \sum_{i=1}^N m_i \exp\left(-\frac{(z - z_i)^2}{2w^2}\right). \quad (2.204)$$

2.5.4 Smoothing length w

As most smoothing methods the coarse graining method has a characteristic length scale w , which determines the amount of smoothing applied. This w should be chosen such that smooth continuous fields are found, but interesting ‘small’-scale phenomena are not completely smoothed out. Figure 2.4 shows the influence of w on the density profile for a flow of height $12d_l$.

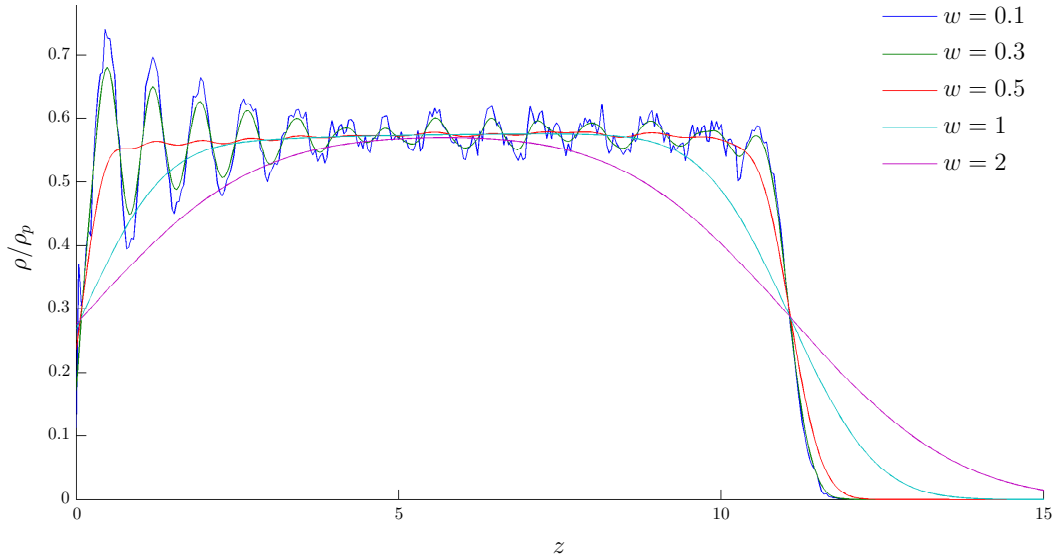


Figure 2.4: Profiles for the density field divided by the particle density, for various coarse graining widths. For $w < 0.5$ the microscopic layering effects are clearly visible, and for $w > 0.5$ macroscopic gradients are smeared out.

From figure 2.4 it can be seen that for $w \geq 0.5$ the macroscopic gradients are affected by the coarse graining, which is undesired. Also, for $w = 0.1$ the statistics gain a significant amount of noise. For $w = 0.3$ the statistics are smooth and still show the layering at the bottom layers. Therefore, unless stated otherwise, all coarse graining statistics in this research will be done with $w = 0.3$, which is 30% of a large particle diameter. Finally, since the infinite reach of the Gaussian kernel is a severe hit on computational times (since for all coarse graining points \mathbf{r} , all particles have to be summed over), a cutoff-length is implemented. A coarse graining point \mathbf{r} only considers particles which are within $5w$ of that point. Since the averaging volume is corrected for this step, it does not introduce a systematic error, it merely reduces the quality of the statistics (i.e the number of particles each point computes statistics over).

2.6 Flow height and Froude number

Although not directly obvious, one of the first problems one encounters when dealing with chute flows is the definition of the flow height h . Since the flows move over rough bottoms (made out of fixed particles) the exact z -location of this bottom is not clearly defined. Also the free surface of the flow has this problem, making the definition of the flow-height h rather cumbersome. First, a simple approximation of the flow height is given, which assumes that all particles are on a rectangular grid. In this way, since the large particles have unity diameter, they contribute a volume of a cube of $1 \times 1 \times 1$ to the total occupied volume V_{total} , and the height of the flow for a rectangular domain of $0 < x < 20$ and $0 < y < 10$ is given by:

$$h_{approx} = \frac{V_{total}}{Area} = \frac{V_l/\eta}{Area} = \frac{N_l}{200\eta} \quad (2.205)$$

This approximated height will often be used to characterise a flow, since the real height is not known on beforehand (it depends for example on the velocity of the flow). To compute this real height however there is an elegant solution if it is assumed that the density ρ is constant in z -direction (within the flow), and that the downward normal stress σ_{zz} is lithostatic and thus balances the force resulting from gravity. In this way the downward normal component of the stress tensor is given by:

$$\sigma_{zz}(z) = \begin{cases} \rho g \cos(\theta)(h - z), & \text{if } 0 \leq z \leq h \\ 0, & \text{otherwise} \end{cases} \quad (2.206)$$

Such that it is easy to integrate σ_{zz} over the entire z -domain:

$$\hat{\sigma}_{zz} = \int_{-\infty}^{\infty} \sigma_{zz}(z) dz = \int_0^h \sigma_{zz}(z) dz = \left[\rho g \cos(\theta) \left(hz - \frac{z^2}{2} \right) \right]_0^h = \rho g \cos(\theta) \frac{h^2}{2}. \quad (2.207)$$

In a similar fashion one can integrate the density field over z :

$$\hat{\rho} = \int_{-\infty}^{\infty} \rho(z) dz = \int_0^h \rho(z) dz = \rho h. \quad (2.208)$$

Now equation (2.207) and (2.208) can be combined into an expression for the flow-height h :

$$\frac{\hat{\sigma}_{zz}}{\hat{\rho}} = \frac{\rho g \cos(\theta) \frac{h^2}{2}}{\rho * h} = \frac{g \cos(\theta) h}{2}, \quad (2.209)$$

$$h = \frac{2}{g \cos(\theta)} \frac{\hat{\sigma}_{zz}}{\hat{\rho}}. \quad (2.210)$$

Since the depth-integrated variables ($\hat{\rho}$ and $\hat{\sigma}$) differ only with a constant pre-factor from the averaged (depth integrated) coarse grained quantities defined in (2.195) it is possible express the flow height in terms of spatially-averaged coarse grained quantities:

$$h = \frac{2}{g \cos(\theta)} \frac{\langle \sigma_{zz}(z, t) \rangle_z}{\langle \rho(z, t) \rangle_z}. \quad (2.211)$$

Note that for the ratio of two spatially averaged coarse grained fields, the averaging intervals cancel out, therefore, for example the depth-averaged velocity in x -direction becomes:

$$\bar{u} = \frac{\langle p_x \rangle_z}{\langle \rho \rangle_z}. \quad (2.212)$$

With both the flow-height and the depth-averaged velocity available the Froude number can be defined as: (combining equation (2.116) with (2.211) and (2.212)):

$$F(x, y, t) = \frac{\bar{u}}{\sqrt{g \cos(\theta) h}} = \frac{\frac{\langle p_x \rangle_z}{\langle \rho \rangle_z}}{\sqrt{2 \frac{\langle \sigma_{zz}(z, t) \rangle_z}{\langle \rho(z, t) \rangle_z}}}. \quad (2.213)$$

In which $\langle p_x \rangle_z$ denotes the depth-averaged momentum in x -direction, and $\langle \rho \rangle_z$ is the depth-averaged density Note that one can of course also average over the x - and y -direction for steady flows, which means actually all spatial dimensions are averaged over:

$$F(t) = \frac{\frac{\langle p_x \rangle_{xyz}}{\langle \rho \rangle_{xyz}}}{\sqrt{2 \frac{\langle \sigma_{zz} \rangle_{xyz}}{\langle \rho \rangle_{xyz}}}}. \quad (2.214)$$

Chapter 3

Simulation setup

In this chapter the numerical DPM simulations that were performed with MercuryDPM will be discussed. There are steady-state simulations which are performed in a periodic box that is periodic in both x and y -direction. These are used to construct the h_{stop} -curves, measuring the stopping heights for different flows at a range of inclinations. Second, steady flow simulations are performed, to fit the linear Froude relation for varying η and σ . Also the influence of the mixed contact-properties will be investigated. In addition to the steady simulations, there are quasi 2D simulations, which are done in a domain that is periodic in y -direction, but not in x . This allows for the simulation of developing avalanches with a flow-front. First however, the simulation parameters will be discussed.

3.1 Simulation parameters

In this section all parameters needed for the simulations are summarised. The parameters for the simulations are non-dimensionalised, such that $d_l = 1$, $m_l = 1$, $g = 1$. This way a flow of height 20 has a height of $20d_l$ and time is given in nondimensional timeunits $\sqrt{d_l/g}$. As stated the large particles will have exactly the same properties as the mono-dispersed particles in [27], and subsequently the small particle properties are set with the relations derived in 2.4.2. Note that in this thesis all quantities will be non dimensional, so units are omitted. The simulation parameters are listed in table 2.1.

Symbol	Value	Description
ρ_p	$\frac{3}{4\pi r_l^3}$	Particle density
r_l	$1/2$	Large particle radius
r_s	σr_l	Small particle radius
μ^p	$1/2$	Microscopic particle friction
γ_l^n	50	Normal damping coefficient large particles
γ_l^t	$\gamma_l^t = \gamma_l^n = 50$	Tangential damping coefficient large particles
k_l^n	$2 \cdot 10^5$	Normal spring constant large particles
k_l^t	$\frac{2}{7}k_l^n$	Tangential spring constant large particles
γ_s^n	Defined in (2.166)	Normal damping coefficient small particle collision
γ_s^t	$\gamma_s^t = \gamma_s^n$	Tangential damping coefficient small particle collision
k_s^n	Defined in (2.165)	Normal spring constant small particle collision
k_s^t	$\frac{2}{7}k_s^n$	Tangential spring constant small particle collision
γ_{ls}^n	Defined in (2.172)	Normal damping coefficient large-small collision
γ_{ls}^t	$\gamma_{ls}^t = \gamma_{ls}^n$	Tangential damping coefficient large-small collision
k_{ls}^n	Defined in (2.175)	Normal spring constant large-small collision
k_{ls}^t	$\frac{2}{7}k_{ls}^n$	Tangential spring constant large-small collision
g	1	Gravity (direction varies with chute-angle θ)
Δt	$\Delta t \approx t_{c,large}/50 \approx 1 \cdot 10^{-4}$	Time integration timestep

Table 3.1: Particle and contact properties

Note that the contact properties for the large particle are chosen to resemble the experiments from Silbert *et al* [21], similarly as in [27]. In the experiments in [21], glass beads were used, with a

dimensional diameter of $d^* = 0.1\text{mm}$, which gives a dimensional timescale of $t^* = \sqrt{\frac{0.1\text{mm}}{9.8\text{ms}^{-2}}} = 3.2\text{ms}$. The dimensional velocity then becomes $V^* = \sqrt{d^*g^*} = 0.031\text{ms}^{-1}$. This being merely an example how to translate the non-dimensional results to dimensional quantities, in the rest of the thesis the nondimensional units will be used.

3.2 Simulations in the periodic box

In a similar fashion as in [27], the research will start with the simulation of a periodic box, depicted in figure 3.1. First goal of this simulations is to obtain the h_{stop} -curve for bi-dispersed flows, which relates the height of the flow (in z -direction) to the chute-angle at which the flow arrests. It was found in [7] that this h_{stop} -curve can be used to derive a friction law to be used by the depth-averaged shallow-layer equations. Secondly, steady flows are needed to verify the applicability of the flowrule (2.123) for $\mu(F, h)$ to bi-dispersed flows. As in [27], MercuryDPM will be the simulation package of choice for the simulations, and a coarse-graining method is used to obtain macroscopic fields from the DPM-simulations, as described in 2.5.

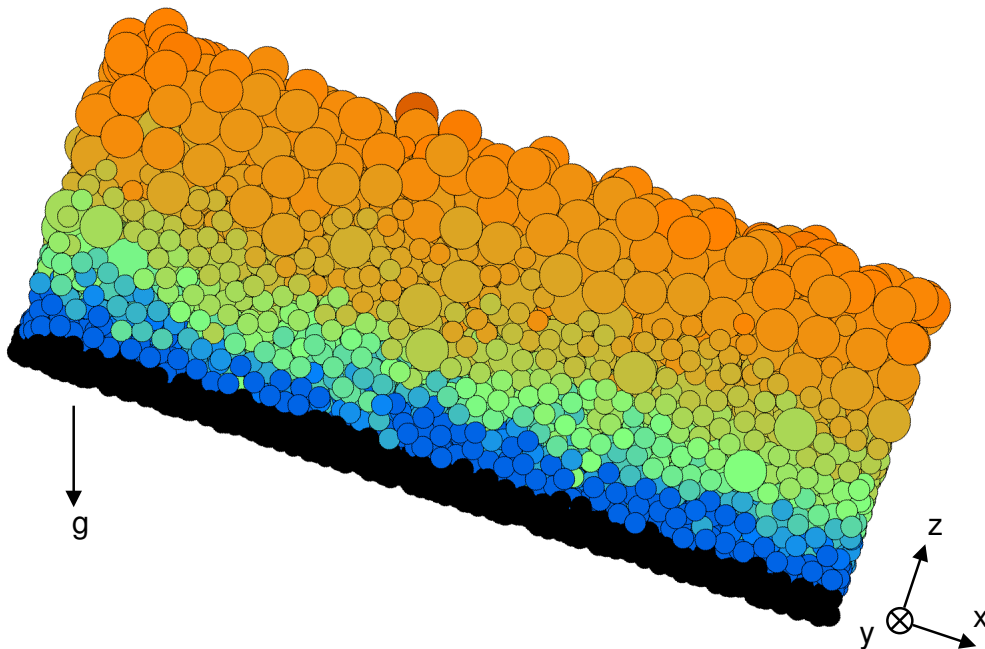


Figure 3.1: Periodic box for steady flow simulations, the colorcode shows the velocity of each particle, with blue being the slow particles and orange the fast particles.

The simulation domain is periodic in both the x and y directions, meaning that particles leaving the domain on one side flow back into the domain on the other side. This periodic behaviour allows to simulate steady flows with much less particles than a full 3D flow (it can be thought of as a simulation of a small part of an infinitely wide and long steady chute flow that is uniform in both x - and y -direction). As opposed to the mono-dispersed flows considered in [27], here bi-dispersed particles are used, with radii r_{large} and r_{small} . The direction of gravity is rotated to simulate different chute inclinations. Note that the z -direction is always perpendicular to the chute. The bottom itself is made out of fixed particles, which have the same size as the small particles, as explained in 3.2.2. Since in general small particles will go to the bottom of the flow, this way the size ratio between the flowing particles colliding with the fixed bottom-particles will equal unity (equivalent to $\lambda = 1$ in [27]). The size of the periodic box is equal to that of the box used in [27], i.e. 20×10 large particle diameters in $x \times y$. To characterise a flow, often the approximated height will be used (as defined in (2.205)), combined with the chute-inclination θ , the large particle volume fraction η (2.126) and the particle size ratio $\sigma = \frac{r_{small}}{r_{large}}$.

3.2.1 h_{stop} -algorithm

Goal of this part of the research is the obtaining of the h_{stop} -curve, the demarcation line between the flowing-regime and the arresting-regime. The angle at which a flow of height h arrests is found by a simple iterative algorithm. The algorithm starts from a flowing steady state, and iteratively decreases the chute inclination θ until flow arrests. The complete flowchart is printed in figure 3.2, and the symbols used are clarified in table 3.2. Walking through the flowchart from the top, the algorithm starts with the generating of a steady flow from which the iterations can be started. This involves inserting the particles in a specific large/small mixture and setting the angle of the chute such that the flow will converge to a steady flowing state. Since the initial flow needs to be steady, one has to wait until both the segregation and the kinetic energy of the flow have steadied out. These two time-scales are studied more in-depth in 3.2.3.

When a steady initial flow is generated the simulation is started and runs for $t_{duration}$ time units, after which the resulting flow is identified as either *flowing* or *arrested*. This is done based upon a minimum kinetic-energy criterion, if the kinetic energy of the flow is below a certain critically low value it is considered to be arrested. When a flow is in the flowing state, simulation is continued in the right branch of the flowchart, in which the angle is saved to θ_{flow} , which represents the lowest angle at which there is a flowing state. Next, the chute inclination is decreased and simulation is continued for $t_{duration}$ seconds. If the flow has arrested the *angle decrement* $\Delta\theta$ is reduced, and if the *stop condition* is not yet satisfied the simulation is restarted from the last flowing-state (θ_{flow}) and then the angle is reduced with the new (lower) angle decrement. The *stop condition* checks whether the angle decrement is above a certain threshold $\Delta\theta_{min}$, if the angle decrement gets below this threshold the simulation is stopped and the arresting angle θ_{stop} is saved. Therefore $\Delta\theta_{min}$ determines the accuracy of the h_{stop} -algorithm.

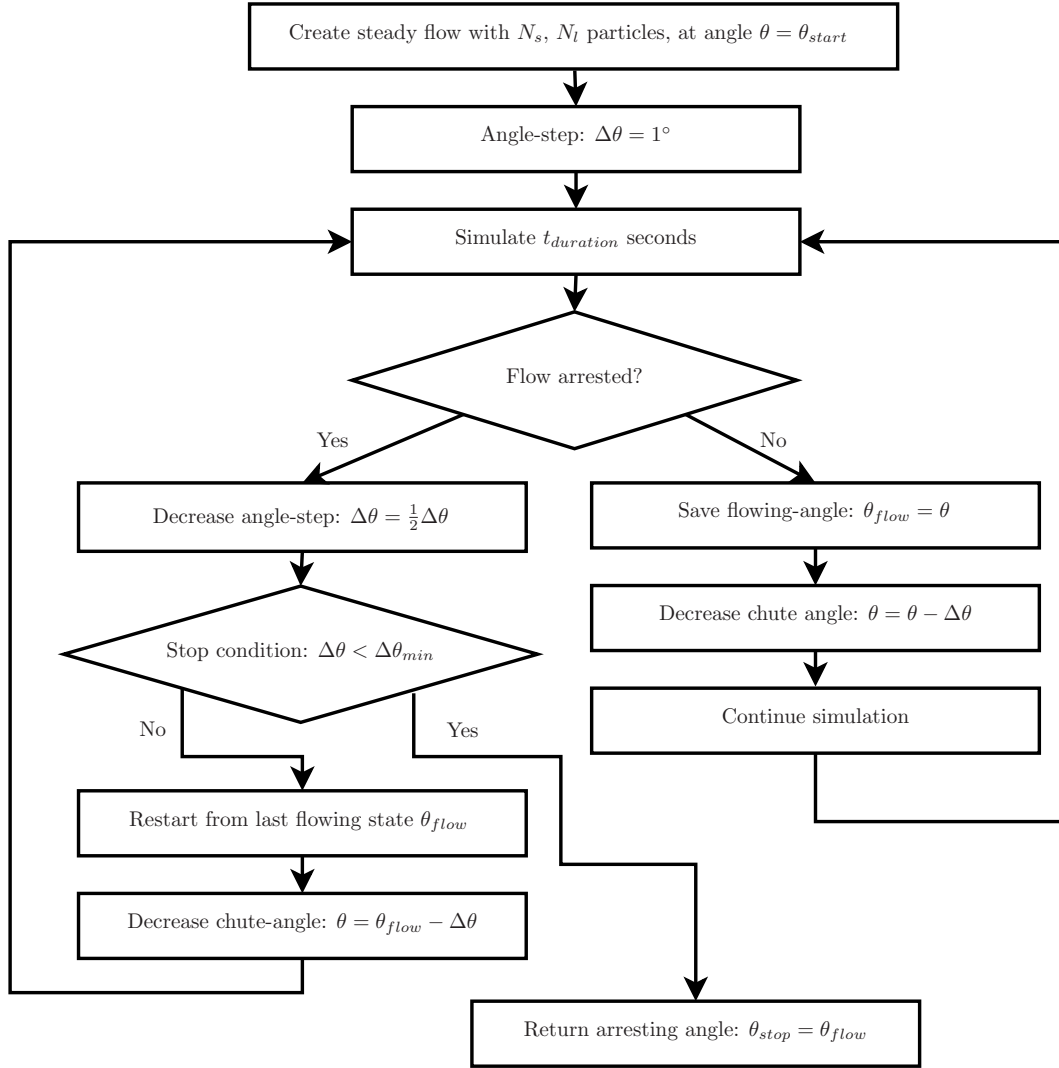


Figure 3.2: h_{stop} -algorithm flowchart

Symbol	Description
N_s	Number of small particles
N_l	Number of large particles
θ	Chute inclination
θ_{start}	Chute inclination at which the initial steady flow is generated
θ_{stop}	Lowest chute inclination at which steady flow is possible
$\Delta\theta$	Decrement with which the chute inclination will be lowered (starting at θ_{start})
$t_{duration}$	The amount of seconds that the chute will be held at θ , after which it is checked whether the flow has arrested or is flowing.
$\Delta\theta_{min}$	The minimal decrement for θ , if it is reached the algorithm is stopped. Hence, it controls the accuracy with which θ_{stop} is obtained
θ_{flow}	The lowest inclination at which there is steady flow

Table 3.2: Symbol table

3.2.2 Initial packing and generation of the rough bottom

As pointed out in the previous section, simulations are started with a ‘steady’ flow. In this section the process of obtaining this flow is discussed. First of all, the bottom of the chute has to be constructed, which consists of fixed particles of radius r_{small} . The bottom itself is created by filling the periodic box with small particles, with the chute angle set to zero. After some time a static packing will form, from which a slice of particles of approximately three particle diameters thick is cut out. This slice is then moved down in z -direction, such that the centre of each particle is below $z = 0$. This way a rough bottom is constructed. Now for the initiation of the flow, the chute is set to an angle which is known to be in the flowing regime. Next, the particles are inserted in a completely segregated packing from the bottom up. This is done as follows: the particle insertion algorithm starts at the bottom, at $z = 0$. It generates a random position in the xy -plane, and checks whether it can insert a small particle without it overlapping with another particle. If it can, the particle is inserted and then it tries to insert the next randomly positioned particle. If however, the particle overlaps with an already existing particle the insertion is rejected and the xy -plane is moved up a distance Δz . When N_{small} particles are inserted, the algorithm continues with the large particles. The particle insertion algorithm is written out in listing Algorithm 1. Note that this way the initial packing is almost perfectly segregated, i.e all large particles are on top of the small particles. The packing however is less dense than the random packing density, so the particles will *compact* (i.e fall down) a little when simulation is started. This will introduce some kinetic energy and immediately diffusion will cause some mixing of the two phases.

Algorithm 1 Initial particle insertion

```
Require:  $N_{large}, N_{small}, \Delta z$   
 $count = 0, insertionHeight = 0$   
while  $count < N_{small}$  do  
   $position.x = rand([x_{min}, x_{max}])$   
   $position.y = rand([y_{min}, y_{max}])$   
   $position.z = insertionHeight$   
  if  $isInsertable(position, r_{small})$  then  
     $insertParticle(r_{small}, position)$   
     $count = count + 1$   
  else  
     $insertionHeight = insertionHeight + \Delta z$   
  end if  
end while  
 $count = 0$   
while  $count < N_{large}$  do  
   $position.x = rand([x_{min}, x_{max}])$   
   $position.y = rand([y_{min}, y_{max}])$   
   $position.z = insertionHeight$   
  if  $isInsertable(position, r_{large})$  then  
     $insertParticle(r_{large}, position)$   
     $count = count + 1$   
  else  
     $insertionHeight = insertionHeight + \Delta z$   
  end if  
end while
```

3.2.3 Steady flow generation

In the h_{stop} -algorithm described 3.2.1 steady-flows are considered, meaning that the flow features do not change over time. In the simulations this mainly concerns the kinetic energy of the flow and the segregation profile. Since the simulation starts with *perfect segregation*, i.e a pure phase of large particles on top of a pure phase of small particles there will be some mixing of the two phases due to diffusion as kinetic energy increases. Also the particles are inserted with zero velocity, and they fall down and accelerate until the flow reaches the steady velocity (i.e the gravitational acceleration is balanced by the drag generated by the rough bottom and the friction of particle-particle collisions).

As mentioned in 2.3 the rate of segregation strongly depends on the size-ratio σ , and the time it takes for the kinetic energy to steady out strongly depends on the number of particles. Now since the flows need to be steady as a starting point for the h_{stop} -algorithm, it is important to know how long it takes until a flow is steady. As a measure for the steadiness of the flow kinetics it is easiest to look at the total kinetic energy, and for the segregation the ratio between the centre-of-mass of the large and small phases is a nice measure (equation (2.128)).

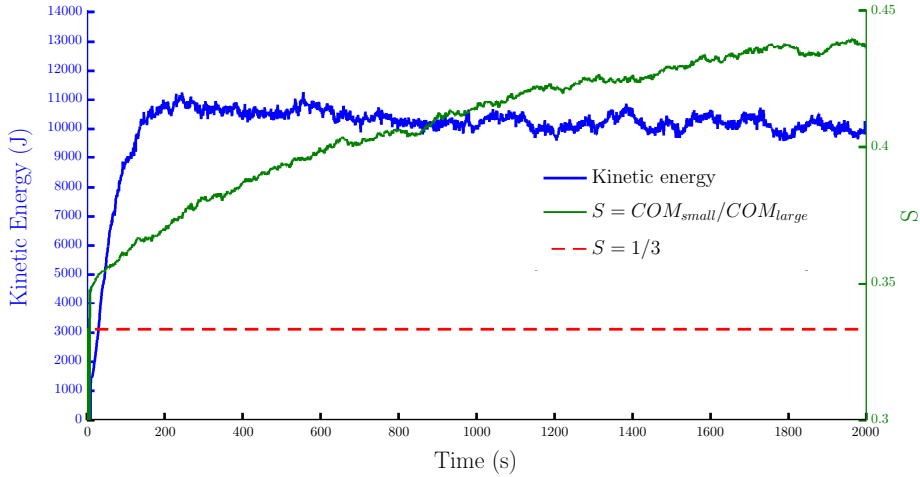


Figure 3.3: Developing segregation and kinetic energy profiles for a flow of height 10, with equal volume for the large and the small phase (i.e $\eta = 0.5$). The chute inclination was $\theta = 24^\circ$ and $\sigma^{-1} = \sqrt[3]{2}$. Initially the flow was completely segregated, which gives $S = 1/3$, marked by the red dotted line. Over time however the diffusion will cause S to increase, with a perfectly mixed flow being $S = 1$.

In figure 3.3 both the kinetic energy and the ratio between the centre-of-mass of the large and small phases are graphed for the first 2000 seconds of a developing flow. The dotted red line marks the ratio $\frac{COM_{small}}{COM_{large}} = 1/3$, which is the case for completely segregated flow. As time progresses the mixing (diffusion) continues such that the ratio of the centre of masses increases (small particles going up, large particles going down). Also it should be noted that the kinetic energy converges to the steady regime much faster than the segregation, which raises the question whether it is actually necessary to wait for the segregation profile to become steady. This will be further assessed in section 4.1.1.

Another important time-scale effect can be seen in figure 3.4. In this figure the total kinetic energy of a flow with 4,000 large particles and 8,000 small particles is shown, which was initially flowing at a 20° chute angle. At $t=0$ the chute-angle is decreased to $\theta = 19^\circ$, and the flow can be seen slowing down and going into another steady flowing state. However, the flow suddenly arrests at $t = 650$ s.

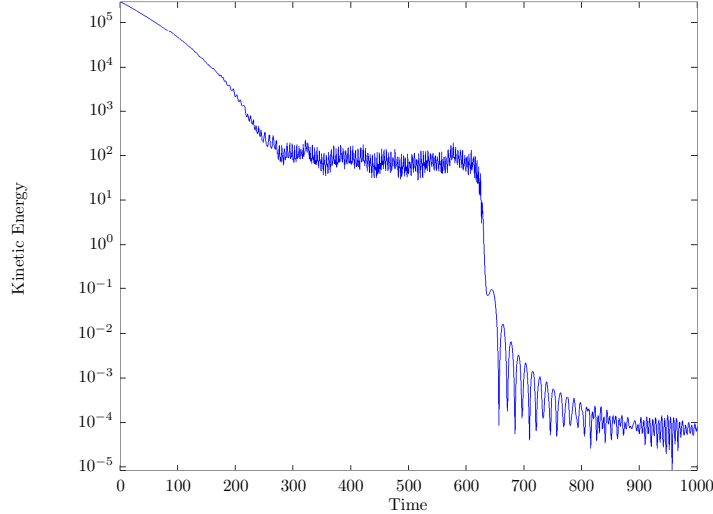


Figure 3.4: An apparently steady flow with $N_l = 4000$, $N_s = 8.000$ and $\sigma^{-1} = \sqrt[3]{2}$ at a chute of inclination $\theta = 19^\circ$. The flow first reaches a meta-stable state ($300 < t < 600$) and then suddenly arrests.

This shows that the simulation timescales have to be picked carefully, since apparently steady flow might arrest when simulated long enough. Due to the nature of the h_{stop} -algorithm however this is not likely to be a problem, since the simulation is always continued from the last flowing state, such that the final, minimal flowing angle is in fact one long simulation. The nice thing about the h_{stop} -algorithm is that statistics of flow variables are not needed (i.e no density, stress and velocity profiles), one only needs to assess whether the flow has arrested, which can be seen from the total kinetic energy and is computed directly within Mercury DPM during the simulation, removing the need for (post processed) coarse grained statistics. For the next step, the fitting of the Froude flowrule to equation (2.117) the depth-averaged velocity and the height of the flow are needed (equation (2.212) and (2.211)), which are extracted from depth averaged, coarse grained statistics as explained in section 2.6. Also, to verify whether the friction coefficient $\mu(F, h)$ resulting from the flowrule (equation (2.123)) is correct, the stress tensor needs to be computed, so it can be compared with $\mu = -\sigma_{xz}/\sigma_{zz}$. To obtain statistics, steady flows are generated and time-averaged statistics are computed over 1.000 timesteps spanning 100 time units.

3.2.4 Mixed contact properties

In 2.4.2 relations for the contact properties for contacts between particles of the two different species have been derived. As stated however the definition of these mixed properties is not unique, and based on a (natural but arbitrary) geometrical argument. Therefore it is necessary to investigate the sensitivity of the obtained results to these mixed contact properties. In this section simulations will be set up to compare the influence of this contact properties with the influence of the *initial conditions* of the flow, the latter meaning a different base and different initial particle positions, which is a result of using a different *random seed* in the generation of the base and initial particle packing. In section 2.4.2 expressions have been derived for the spring-stiffness k and damping-constant γ of a contact in both tangential and normal directions:

$$\gamma_{ls}^n = 2 \frac{m_{ls}}{m_l} \frac{t_c^l}{t_c^{ls}} \gamma_l^n, \quad (3.1)$$

$$k_{ls}^n = m_{ls} \left(\left(\frac{\pi}{t_c^{ls}} \right)^2 + \left(\frac{\gamma_{ls}^n}{2m_{ls}} \right)^2 \right), \quad (3.2)$$

$$\gamma_{ls}^t = \gamma_{ls}^n, \quad (3.3)$$

$$k_{ls}^t = \frac{2}{7} k_{ls}^n \quad (3.4)$$

Note that the tangential properties are set in agreement with [27]. Due to the way the contact properties are set, it is known that a (normal) collision of two large particles has a longer collision-time than a collision of two small particles. Therefore, for a collision of two differently sized particles the collision time t_c^{ls} has a lower-bound t_c^s and an upper-bound t_c^l , i.e $t_c^s < t_c^{ls} < t_c^l$. So to investigate the sensitivity of the choice for t_c^{ls} , simulation results with t_c^{ls} set to its minimum (t_c^s) and maximum (t_c^l) can be compared. Since a DPM simulation is a chaotic system (i.e small perturbations can give a completely different result in terms of individual particle positions and velocities), it is necessary to look at time-averaged quantities (e.g the total kinetic energy of the flow and the centres of mass for both species, a measure for the segregation). These quantities are compared to simulations for which the initial particle packing (different initial positions and different base by using a different random seed) and the initial segregation state (normally graded vs segregated) are changed. This gives eight different simulations:

Simulation	1	2	3	4	5	6	7	8
Mixed collision time t_c^{ls}	t_c^l	t_c^l	t_c^l	t_c^l	t_c^s	t_c^s	t_c^s	t_c^s
Initial state (S=perfectly segregated, N=normally graded)	S	S	N	N	S	S	N	N
Random seed	1	2	1	2	1	2	1	2

Table 3.3: Mixed contact property test simulations

The simulations each contain 1.000 large particles and 2.000 small particles, with a size-ratio $\sigma^{-1} = \sqrt[3]{2}$, giving $\eta = 0.5$, i.e the large and the small phase have equal total volume. The height of the flow is approximately 10 large particle diameters, and the chute has an inclination of $\theta = 24^\circ$. All simulations are run for 4000 seconds, allowing to reach a steady state, which can be seen from the evolution of the total kinetic energy (Figure 3.5) and the centre's of mass for both species (Figure 3.6). Also visible in the kinetic energy plot is the difference between the initially segregated flows and the initially normally graded flows. For the latter all large particles start at the bottom, and have to travel all the way up to the top half of the flow. This explains the 'lag' in the development of the steady state for the kinetic energy. The segregating behaviour can be seen even better when looking at the centre of mass (COM) for both different species, shown in figure 3.6. Two distinct paths are clearly visible, the initially normally graded flow for which the COM-profiles cross at approximately $t=500s$, and the initially segregated flow for which the COM's move slightly towards each other over time, which is due to the diffusive mixing of the flows (initially they are completely segregated). As expected however both initial states converge to the same steady state flow.

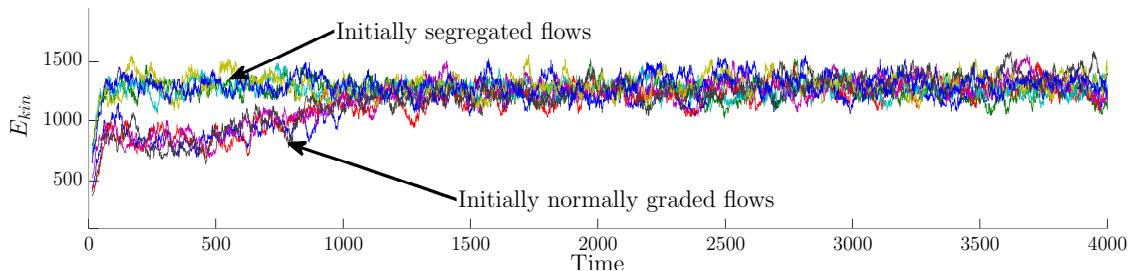


Figure 3.5: Total kinetic energy for all eight test simulations. The kinetic energy for the initially normally graded flows develops much slower than for the initially segregated flows. This is due to the segregation, which takes much longer than the development of the kinetic steady state.

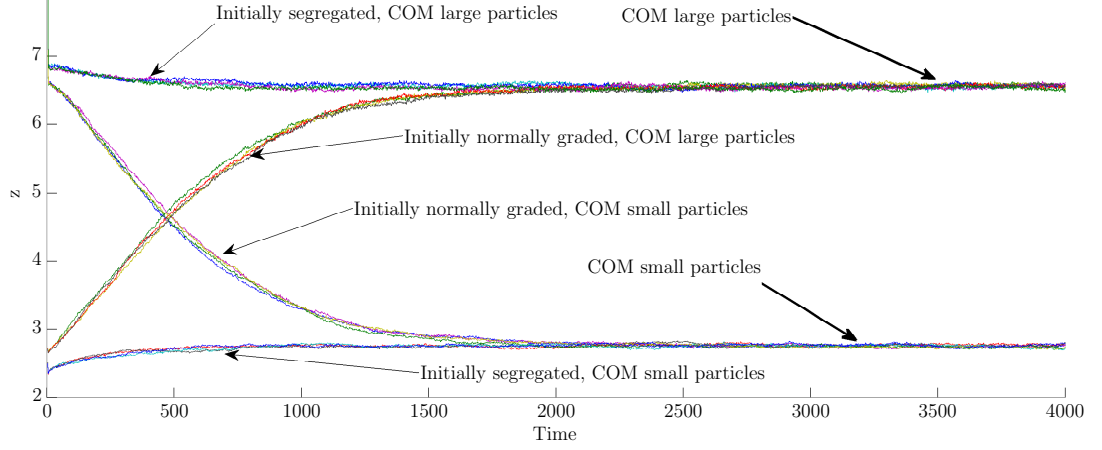


Figure 3.6: Centre of mass for both large and small species, for all eight test simulations

From the figures above it can also be observed that there are no large differences between the flows with different mixed contact properties or random configurations (Note that all eight simulations are plotted, but since all profiles are on top of each other a legend has been omitted). A more quantified way to compare the influence of the different random seeds with the influence of the mixed contact properties is to look at the *time averaged kinetic energy* for the different simulations. If now the simulations are grouped by either their random set or by the mixed contact properties, then the average kinetic energy for such a group can be compared with the average kinetic energy of all groups, to compare the influence of the random-seed with that of the mixed contact properties. Let E_{kin}^i be defined as the time-averaged kinetic energy of the last 1.000 dimensionless seconds of simulation i from table 3.3, then the total average kinetic energy for all simulations is defined as:

$$E_{kin}^{total} = \frac{1}{8} \sum_{i=1}^8 E_{kin}^i = 1.2928 \cdot 10^3 \quad (3.5)$$

Now the relative difference between the total average and the average kinetic energies for the groups based on either the random seed or on the mixed contact properties is given by:

$$\text{Different random seed:} \quad (3.6)$$

$$\text{Set 1: } \frac{|E_{kin}^{total} - E_{kin}^{Random1}|}{E_{kin}^{total}} = \frac{|E_{kin}^{total} - \frac{E_{kin}^1 + E_{kin}^3 + E_{kin}^5 + E_{kin}^7}{4}|}{E_{kin}^{total}} = 0.0257, \quad (3.7)$$

$$\text{Set 2: } \frac{|E_{kin}^{total} - E_{kin}^{Random2}|}{E_{kin}^{total}} = \frac{|E_{kin}^{total} - \frac{E_{kin}^2 + E_{kin}^4 + E_{kin}^6 + E_{kin}^8}{4}|}{E_{kin}^{total}} = 0.0257. \quad (3.8)$$

$$\text{Different mixed contact properties:} \quad (3.9)$$

$$\text{Set 1 } (t_c^{ls} = t_c^l): \frac{|E_{kin}^{total} - E_{kin}^{t_c^l}|}{E_{kin}^{total}} = \frac{|E_{kin}^{total} - \frac{E_{kin}^1 + E_{kin}^2 + E_{kin}^3 + E_{kin}^4}{4}|}{E_{kin}^{total}} = 0.0056, \quad (3.10)$$

$$\text{Set 2 } (t_c^{ls} = t_c^s): \frac{|E_{kin}^{total} - E_{kin}^{t_c^s}|}{E_{kin}^{total}} = \frac{|E_{kin}^{total} - \frac{E_{kin}^5 + E_{kin}^6 + E_{kin}^7 + E_{kin}^8}{4}|}{E_{kin}^{total}} = 0.0056. \quad (3.11)$$

Clearly, the influence of the initial random positions is larger (though still small) than the influence of the mixed contact properties. This supports the conclusion that the choice of the mixed collision parameters is of minor influence on the behaviour of the system as a whole.

Finally, also the influence of both parameters on the velocity profile of the flow in z -direction is analysed. This profile is obtained by the coarse graining method as described in 2.5, and averaged both spatially (in x and y -direction, using 1.000 coarse graining points in the z -direction) and in time (over the last 1000 time units). To show the influence of the different parameters (mixed collision

properties and random initial conditions) the four profiles for these parameters are plotted. Note that this means that each velocity profile is the average of four simulations, so if $v_i(z)$ is the velocity profile as a function of z belonging to a simulation i from table 3.3 the four different averaged samples are:

$$\text{Random set 1 : } v_{avg} = \frac{1}{4}(v_1 + v_3 + v_5 + v_7), \quad (3.12)$$

$$\text{Random set 2 : } v_{avg} = \frac{1}{4}(v_2 + v_4 + v_6 + v_8), \quad (3.13)$$

$$t_c^{ls} = t_c^l : v_{avg} = \frac{1}{4}(v_1 + v_2 + v_3 + v_4), \quad (3.14)$$

$$t_c^{ls} = t_c^s : v_{avg} = \frac{1}{4}(v_5 + v_6 + v_7 + v_8). \quad (3.15)$$

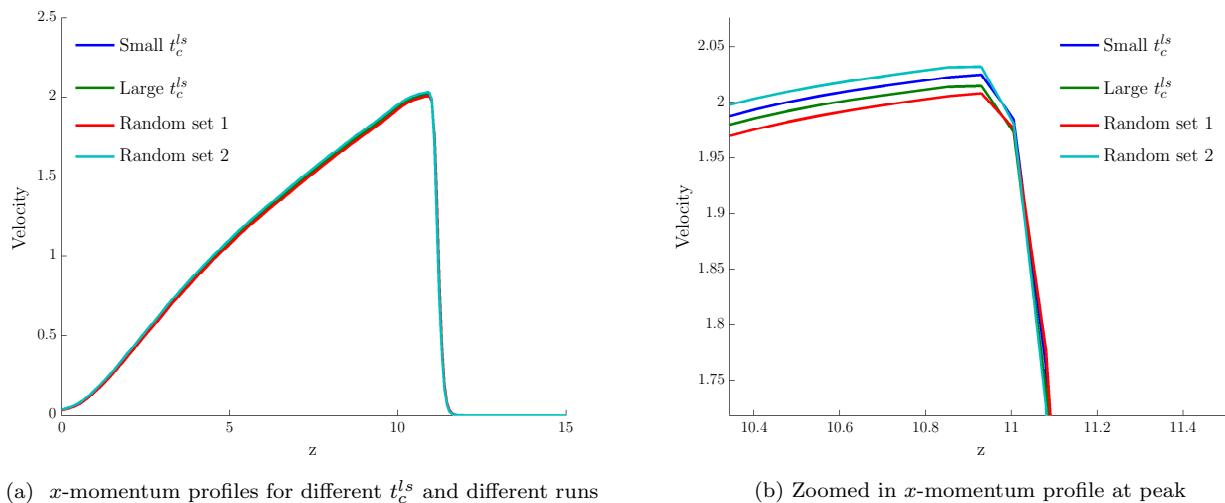


Figure 3.7: Profiles showing momentum in x -direction, for different t_c^{ls} and different random sets

First of all, in figure 3.8a it is clear that the velocities all match to the same profile, so the influence of both parameters is small. If one zooms in on the plot, as in figure 3.8b it can also be seen that in fact the difference in the average velocity for the different random initial conditions is more pronounced than the difference between the two different mixed collision properties. This is in line with the comparison based on the kinetic energy (3.11). Also, Silbert *et al* [21] found that the depth velocity profiles vary only slightly when the normal spring constant for a contact was varied over as much as two orders of magnitude. This shows that the system is not sensitive to the choice for the mixed collision properties, and thus the definition from 2.4.2 can be used.

3.2.5 Varying volume-ratio η

To study the influence of the relative volume fraction of the large phases η (2.126) on the friction law, this ratio is varied over a range of values. Note that with η known, the volume of large and small particles is known. So, it can be thought of as a concentration, describing the relative volume of the both phases present in the mixture. This is an important parameter, since different parts of a developing bi-dispersed chute flow will have different mixtures (i.e only large particles in front, a mixture in the steady bulk, and the transition in between). From literature ([29], [18]) it is known that this parameter will affect the frictional behaviour of the flow. So if one wants to use steady state results to predict properties of the chute flow, then one needs steady state results for the different η

regimes in the avalanche. Therefore simulations with five different values for η will be compared:

$$\eta_1 = 0 \text{ (only small particles)} \quad (3.16)$$

$$\eta_2 = 1/4 \quad (3.17)$$

$$\eta_3 = 1/2 \text{ (both phases equal in volume)} \quad (3.18)$$

$$\eta_4 = 3/4 \quad (3.19)$$

$$\eta_5 = 1 \text{ (only large particles)}. \quad (3.20)$$

This will give an idea of the effect of the different mixtures on the behaviour of the flow. Note that the extreme cases $\eta = 0$ and $\eta = 1$ have particles of only one size (except for the bottom particles, which are always of radius r_{small}). Next the size ratio σ needs to be set for this case. There are two important effects playing a role here, first of all, as stated, the segregation features are more pronounced for higher size ratios thus: faster segregation rates and a sharper segregation in the steady state. Note that for $\sigma > 2.5$ additional physics start playing a role, since then small particles will be able to reside in between the gaps of the large particles [23]. Second, a higher size ratio increases the computation time, since there will be more (small) particles needed for the same flow-height (since the diameter of the large particles is fixed at unity). Therefore σ is set based on the steady-state segregation profiles in [23], such that there will develop an (almost) pure layer on the top and bottom of the flow and the segregation will be clearly visible. Following this argument the default size ratio becomes $\sigma = \sqrt[3]{1/2}$, such that for small and large phases of equal volume ($\eta = 1/2$) one gets:

$$N_{small} = \frac{N_{large}}{\sigma^3} \frac{1 - \eta}{\eta}, \quad (3.21)$$

$$r_{small} = \sigma r_{large} = \sqrt[3]{1/2} r_{large} \approx 0.397. \quad (3.22)$$

3.2.6 Varying size-ratio σ

Another key parameter in bi-dispersed flows is the size ratio σ (2.125), which relates the diameters of the large and small particles. The effect of this parameter on the h_{stop} -curves will be investigated by varying it over a range of values:

$$\sigma^{-1} = \frac{d_l}{d_s} \in [1.1, \sqrt[3]{2}, 1.5, 2] \quad (3.23)$$

Note that the second σ^{-1} is the choice $\sigma^{-1} = \sqrt[3]{2} \approx 1.26$ of the previous section, which makes the volume of a small particle half that of a large particle. For this case the volume fraction ratio is fixed at $\eta = 1/2$, this way the segregation interface is nicely centred in the middle of the flow.

3.3 Quasi 2D simulations

The ultimate goal of this research is to use the Pouliquen friction law to predict the friction for non steady, non uniform chute flows. However, particle numbers for full 3D chute flows would be far greater than the maximum number of particles that is feasible to simulate with a non-parallel code on the computers presently available (the upper limit is approximately 10^6 flow particles). Therefore, a compromise is sought, in which the periodicity in the x -direction is removed, but the flow remains periodic in y -direction. This means that this quasi 2D flow does develop a front, with the accompanying segregation features (i.e large particles will accumulate at the front), but it will not be able to develop any gradients in the y -direction. The bottom is taken from the periodic box simulations, and then copied a hundred times in x -direction to create a chute of 2000 units long. The chute is fixed at an angle of $\theta = 24^\circ$, and the particle size ratio is set to $\sigma^{-1} = \sqrt[3]{2}$. An example snapshot of such an avalanche is depicted in figure 3.8, in which the inclination is not shown. Also, it should be noted that the markers represent particle positions, and not shape, since the aspect ratio of the plot is far from unity the spherical particles would look like extremely squeezed spheres.

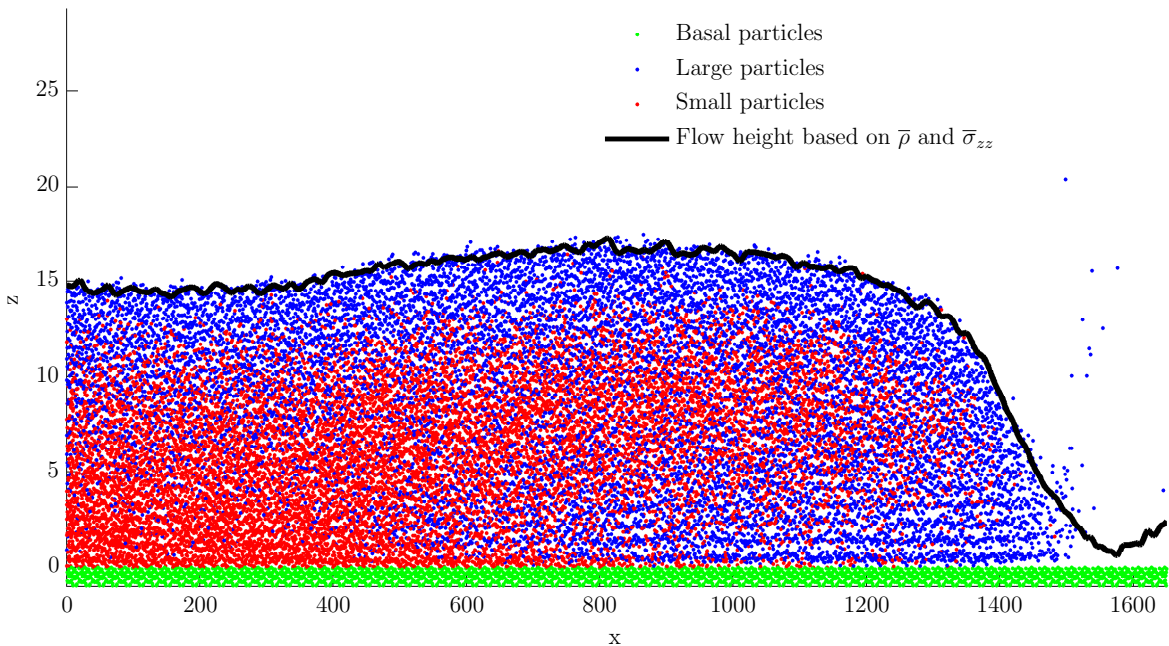


Figure 3.8: Example quasi 2D avalanche with particle positions and flow-height computed from equation (2.211). The chute-inclination $\theta = 24^\circ$, $\mu_s^p = \mu_l^p/2$ and the inflow has a height of approximately 15 large particle diameters. The snapshot is taken at $t = 800$. Note that the vertical axes is stretched by approximately a factor 40.

Please note the extreme aspect ratio of the plots for the rest of this thesis, the avalanches are long and shallow, which is not directly obvious from the pictures. The typical height of the avalanche is approximately 10 large particle diameters, whereas typical lengths are of the order of 1.000 large particle diameters. For reference a snapshot of the avalanche depicted in figure 3.8 with equally scaled x and z -axis is plotted in figure 3.9.

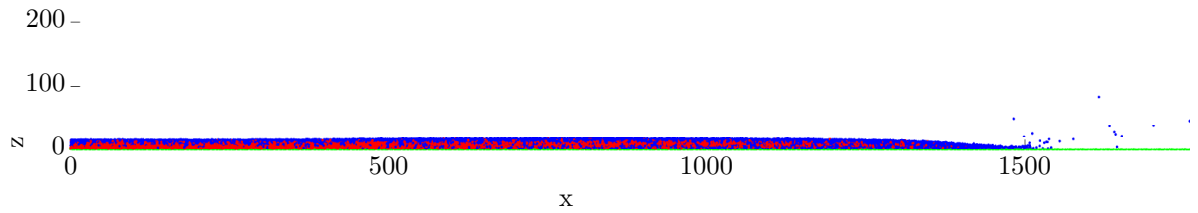
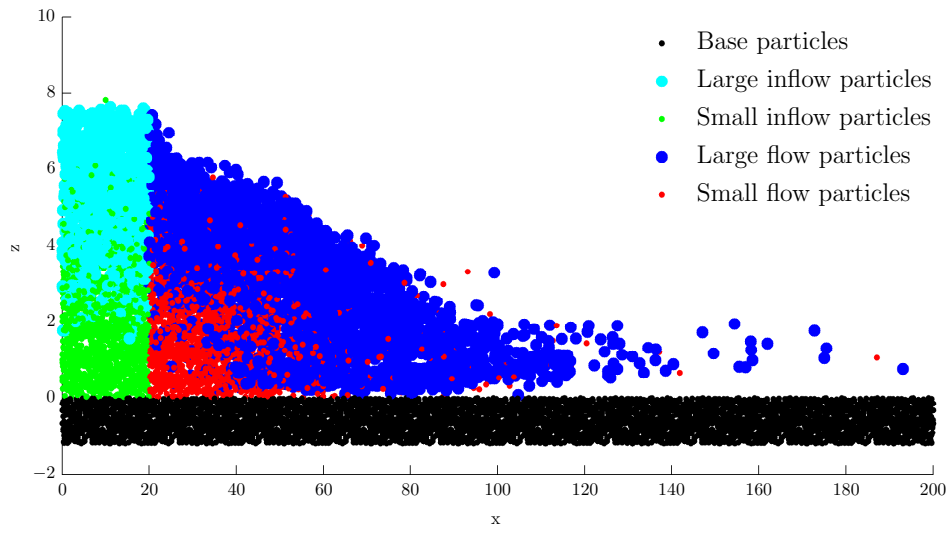


Figure 3.9: Flow snapshot with a equal axis scaling. Since this is the same snapshot as in figure 3.8, the shallowness of the flow becomes obvious

It is evident that graphing the flows in their real aspect-ratio is not feasible. In the following sections the simulation of these quasi 2D flows will be discussed. The evolution of flows like these depend heavily on the way the inflow particles are generated, which is discussed in section 3.3.1. Also the particle friction coefficients of the two different particle types play an important role, which are treated in 3.3.2. Finally, the unsteady nature of the avalanches complicates obtaining statistics (i.e, time-averaging is no longer possible), which is dealt with in section 3.3.3.

3.3.1 Inflow

Whereas the generation of steady flow for the periodic box is just a matter of waiting until the flow features have steadied out, the generation of a steady inflow for the quasi 2D avalanche has a bit more to it. A classical approach would be to simulate a *hopper*, i.e a big bucket filled with particles which flow out through a funnel and thus ensure a constant supply of material. Making this inflow steady however is not easy, since the flow will only be steady far from the inflow. This is because also inside the hopper there will be segregation phenomena, and hence the mixture is difficult to control. Therefore a trick is being used; since a steady state periodic box is already available, particles are simply allowed to flow out of the box when they reach the periodic wall at $x = 20$, but also a periodic copy back to the back of the periodic box is made. This splits the system in *flow particles*, that have flown out, and *inflow particles* which are inside the periodic box. Now it has to be made sure that *flow particles* don't interact with periodic copies of *inflow particles*, since the moment a inflow particle becomes a flow particle, it will have 100% overlap with the periodic copy of the inflow particle from which it originates, which of course is un-physical and would cause the system to explode. Given this limitation (which is countered by a simple check in the collision check routine of Mercury DPM), this type of inflow has proven to be very stable and effective.



(a) $t=100$

Figure 3.10 shows the inflow for two different snapshots. Note the different scales for the x - and y -axis, therefore the particles are not correctly sized, they are just simple markers for the positions and sizes of the particles. It is possible however to see how the inflow over time develops a steady avalanche flow. For all quasi 2D avalanches the volume fraction for the inflow domain is fixed at $\eta = 0.5$, note however that since the flow is segregated and the upper half of the flow is faster than the bottom half, this causes the number of large particles entering the domain to be much higher than the number of small particles. This is also clearly visible from figure 3.10.

3.3.2 Particle friction

In nature and industry avalanches show specific features which are the result of the large particles being relatively ‘slow’ compared to the small particles. Due to segregation the large particles get transported to the front of the flow, where they will slow down and get recirculated as the avalanche flows over them. From literature [18] it is known that to have pronounced segregation effects, the particle friction of the large particles should be high compared to that of the small particles. For example for mud-slides this is often the case, large rocks are rougher (less spherical) than small pebbles. To investigate this roughness effect, two different systems are simulated in which the particle friction coefficients of the two different phases are changed (large and small particles). In the first system both the small and the large particle friction coefficients (μ_s^p and μ_l^p) are kept constant at $\mu_s^p = \mu_l^p = 0.5$. For the second system however the particle friction for the small particles is reduced, effectively making the large particles relatively frictional. The values for the system with reduced friction for the small particles are:

$$\mu_l^p = 0.5, \tag{3.24}$$

$$\mu_s^p = 0.25, \tag{3.25}$$

$$\mu_{ls}^p = 0.375. \tag{3.26}$$

Hence the particle friction for a collision of a small and large particle μ_{ls}^p is set as the mean of the two different coefficients.

3.3.3 Statistics

A major complication involving the quasi 2D chute flows, is the fact that it is not a steady system. With the periodic box simulations, it was possible to improve the statistics as needed by time-averaging. With the transient flow-front of the quasi 2D avalanche this is not possible. Even averaging in a frame moving with the flow-front is no clear solution since the avalanche will develop a head that grows in time, as more and more large particles will accumulate at the front. Therefore, statistics are computed from high time-resolution data, and then time-averaged over a short timespan. Given that typical flow-speeds are of order unity, whereas collision times are of order 10^{-3} (in dimensionless simulation time units) it is chosen to average over 1.000 timesteps recorded in a timespan of 10 time units. This way enough data is recorded to get proper statistics, but the front will not be ‘smeared out’ to much, since the distance travelled by the front in 10 seconds is small compared to the length of the system (typically a 1.000 units). One should also note that due to the aspect ratio of the different figures printed the front of the avalanche looks rather steep. This is however not the case, the gradient of the height $\frac{\partial h}{\partial x}$ is always small, since the flows are very shallow (this can be seen from 3.9). Also, for the quasi 2D avalanche coarse grained statistics will be computed. However, when depth averaging is applied (which still allows to compute important variables like the Froude number and the flow-height as a function of x), the coarse graining width does not effect statistics in the z -direction any more, and hence w can be increased. Since the x -direction has a length of typically 1.000 units, even with $w = 5$ it is still possible to get statistics with proper resolution. The only drawback of this high value for w is the loss of observability of oscillations on the particle scale [25].

Chapter 4

Results

Having established the necessary theoretical base in chapter 2 and the experimental simulation procedures in chapter 3, in this section the results will be presented. The global outline will be the following: First, a series of h_{stop} -curves will be measured for arresting flows in the periodic box in 4.1.1. These h_{stop} -curves then are used to check whether the Froude-flowrule (equation (2.117)), which is needed for the Pouliquen friction law, holds for bi-dispersed flows in section 4.1.2. If both the h_{stop} -results and the Froude-flowrule are established, the friction law can be used to predict the friction for steady flows in the periodic box. Finally, the friction law can be used to try to predict the friction coefficient in a developing, transient quasi 2D chute flow in 4.2.

4.1 Periodic box simulations

In this chapter the results for the bi-dispersed simulations in the periodic-box are presented. First of all the h_{stop} -curve itself will be measured in section 4.1.1, for cases with varying η and σ . To obtain this curve the h_{stop} -algorithm as described in 3.2.1 is used. The stopping angles for flow-heights ranging roughly from 3 large particle diameters (note: $d_{large} = 1$) up to $30d_{large}$ are measured. In addition to that, every flow-height is ran multiple times, with different initial particle positions and a different (random) bottom. This ensures the stability of the result. With the h_{stop} data available, it is possible to see whether the Froude-flowrule ((2.117)) also holds for bi-dispersed data. This will be treated in section 4.1.2. In this section also the validity of the friction law for bi-dispersed flows will be tested. Both the h_{stop} -curves and the steady state Froude simulations will be done for three different cases, investigating the influence of the bi-dispersity.

System	η	σ	Particle friction
1: Varying η	$\eta \in [0, 1/4, 1/2, 3/4, 1]$	$\sqrt[3]{2} \approx 1.26$	$\mu_s^p = \mu_l^p$
2: Varying η , $\mu_s^p < \mu_l^p$	$\eta \in [0, 1/4, 1/2, 3/4, 1]$	$\sqrt[3]{2} \approx 1.26$	$\mu_s^p = \mu_l^p/2$
3: Varying σ	0.5	$\sigma^{-1} \in [1.1, \sqrt[3]{2}, 1.5, 2]$	$\mu_s^p = \mu_l^p$

Table 4.1: Simulation system parameters for which h_{stop} and Froude data will be measured.

The different systems are listed in table 4.1. The first system investigates the effect of the relative volume fraction of the large particles, η , while keeping the size ratio constant. The second system does the same, but with a reduced small particle friction coefficient, which as explained in 3.3.2 makes the segregation features more pronounced. Finally, the third system varies the size ratio σ .

4.1.1 h_{stop} simulations

In this section the obtained h_{stop} -curves for the different systems are discussed. They relate the height at which a flow will arrest to the chute inclination. For each case a set of h_{stop} -curves is measured, each characterised by the three fitting parameters A , δ_1 and δ_2 . First however an example h_{stop} -run is dissected and some important points of attention and caveats are discussed in section 4.1.1. Next the fitting method is discussed shortly in section 4.1.2, after which the results are printed for the three different cases.

Sample run

First an example h_{stop} -run is treated. It consists of the preparation of the initial steady flow, and then the gradually lowering of the chute angle θ until the flow arrests. Plotted in figure 4.1 are both the total kinetic energy of the flow and the angle of the chute versus time for a flow of 3200 large particles. Since $\sigma^{-1} = \sqrt[3]{2}$, this gives 6400 small particles given that $\eta = 0.5$.

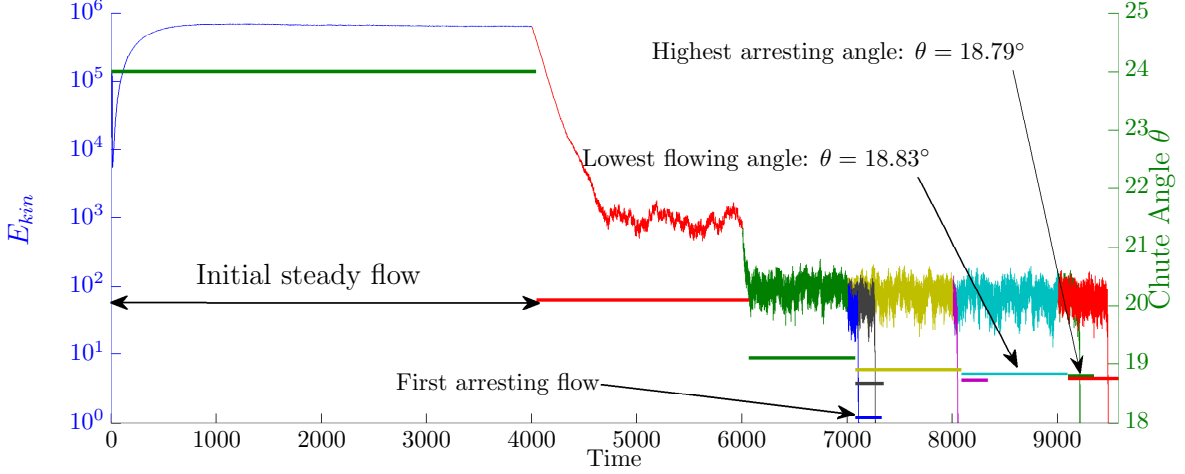


Figure 4.1: Total kinetic energy and the chute angle θ for a sample h_{stop} -run

The first 4.000 time units consists of the preparation of the initially steady flow at $\theta = 24^\circ$. Next, the angle is lowered to $\theta = 20^\circ$ and simulation is continued, since the flow is still flowing (the red part of the curve), the angle is lowered again to $\theta = 19.0^\circ$, and then again to $\theta = 18.0^\circ$, which causes the flow to arrest (the dark blue part, the kinetic energy goes down dramatically). Then the flow is restarted from the flowing state ($\theta = 19.0^\circ$), and the angle is decreased with a smaller decrement. This is repeated until a certain minimum angle decrement is reached (so a maximum number of arresting flows). Then the lowest flowing angle is saved. Note that this way the lowest flowing angle belongs to a continuous simulation started at $t = 0$, such that steady flow is ensured. Although, in figure 4.1 only the total kinetic energy is graphed, there is also developing segregation. Since the flows are meant to be steady, also the segregation profile should be steady. To measure the segregation state, the ratio S of the vertical centre-of-mass (COM) of the small and the large phase from equation (2.128) is used. As the segregation approaches a steady state, this quantity should become constant. The COM-ratio S is plotted for the same h_{stop} -run for which the kinetic energy has been plotted in figure 4.1:

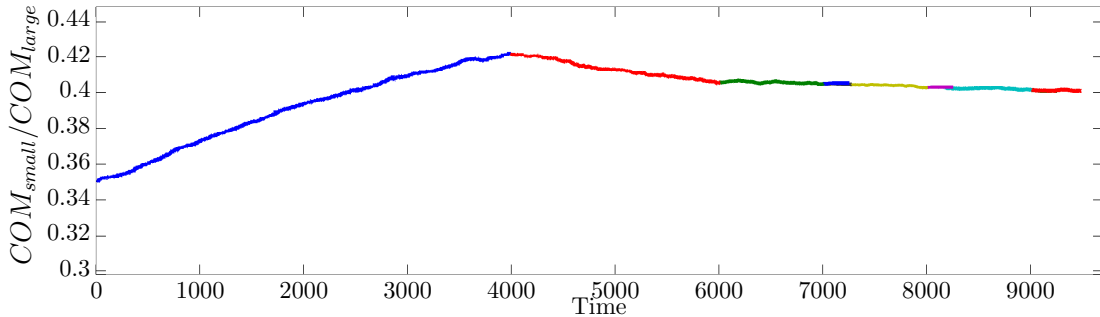


Figure 4.2: COM-ratio for a sample h_{stop} -run

An interesting phenomena appears, as mentioned in section 3.2.3, it is clear that the segregation (or in this case actually de-segregation, i.e diffusive mixing) takes much more time to develop than the kinetic profile. In fact, it does not even reach a steady state in the first 4000 seconds of the simulation.

However, since over time the flow approaches the arrested regime (i.e lowering the angle and thus decreasing the kinetic energy) this will also cause diffusion to decrease, and it can be seen that the steady segregation state is (almost) reached after 6,000 seconds.

Fitting h_{stop}

Runs like depicted in 4.1.1 were done for a a range of flow heights, and the resulting stopping angles give the h_{stop} -curve. With this h_{stop} -data the same function as used in [17] and [27] will be fitted:

$$h_{stop}(\theta) = Ad_{large} \frac{\tan(\delta_2) - \tan(\theta)}{\tan(\theta) - \tan(\delta_1)} \quad (4.1)$$

The function was fitted to the h_{stop} -data resulting from the DPM-simulations with MATLAB's non-linear least-squares fitting function with fitting parameters A, δ_1, δ_2 . The first attempt for the fit was by choosing A, δ_1 and δ_2 to minimise the most simple error norm, the sum of the error squared of N_p fitting points (stopping angles):

$$E = \sum_{i=1}^{N_p} (h_{stop}(\theta_i) - h_i)^2 \quad (4.2)$$

This however does struggle to come to a good fit at both the left and right limit (δ_1 and δ_2) of the h_{stop} -curve, since the error will be much higher for a small deviation in the fit close to δ_1 . Therefore a weighted fit was introduced, in which the error is weighted with the angle θ :

$$E_{weighted} = \sum_{i=1}^{N_p} \theta_i (h_{stop}(\theta_i) - h_i)^2 \quad (4.3)$$

As this still did not give satisfactory results, it was observed that the angle θ spanned only a small range compared to its magnitude. To overcome this problem the weight is shifted, such that values are almost zero close to δ_1 , and increases quadratically with increasing θ . Since the minimum of δ_1 that was observed was approximately 18 degrees, the weighting factor was shifted by 16 degrees, to prevent the weight factor from reaching zero:

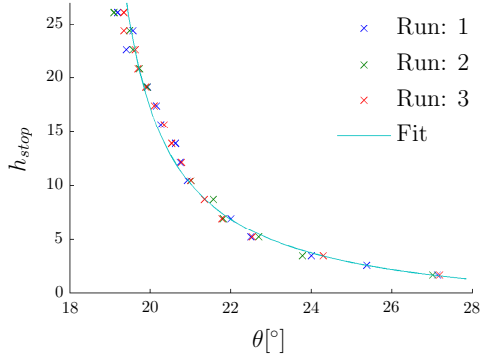
$$E_{shifted} = \sum_{i=1}^{N_p} (\theta_i - 16^\circ)^2 (h_{stop}(\theta_i) - h_i)^2 \quad (4.4)$$

This fit gave results that followed the data at both extremes. Finally, to asses the quality of the fit one can look at the norm of the residual, divided by the number of fitting data points. So for N_p simulations, giving N_p stopping angles θ_i and heights h_i , the relative residual error E_h is defined as:

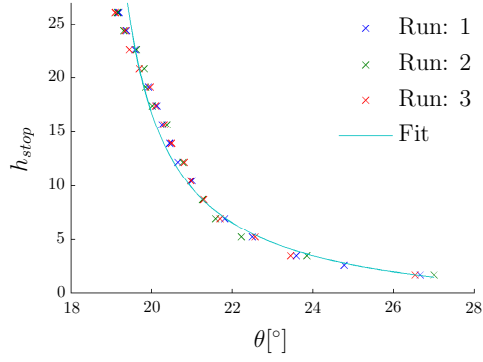
$$E_h = 1/N_p \sum_{i=1}^{N_p} (\theta_i - 16^\circ)^2 (h_{stop}(\theta_i) - h_i)^2 \quad (4.5)$$

System 1: Varying volume-ratio η

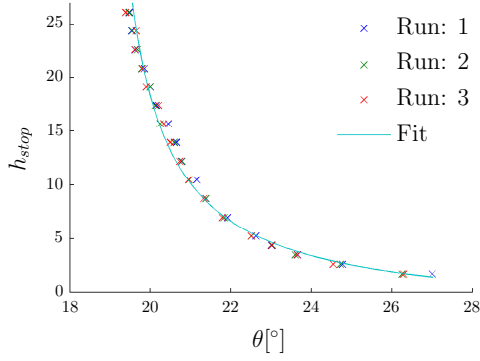
The first results presented are the h_{stop} curves for System 1, with varying volume ratio η . Here the particle size ratio σ is kept constant at $\sigma^{-1} = \sqrt[3]{2}$, such that the small particles have half the volume (and mass) of the large particles. The reason η and σ are not varied both, is to keep the parameter-space reasonably small. Already a typical h_{stop} -curve like below is constructed with over 3.000 simulations, taking almost two weeks and using approximately 150 CPU-cores.



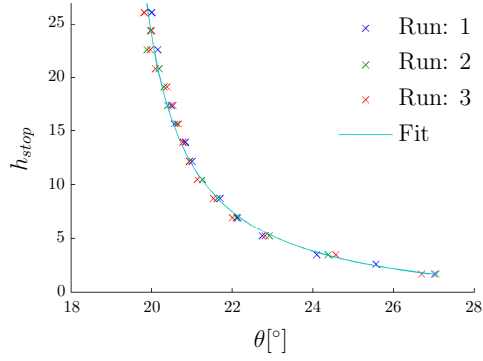
(a) h_{stop} for $\eta = 0$, fit to eq. (4.1):
 $A = 1.88, \delta_1 = 18.25^\circ, \delta_2 = 34.03^\circ, E_h = 5.93$



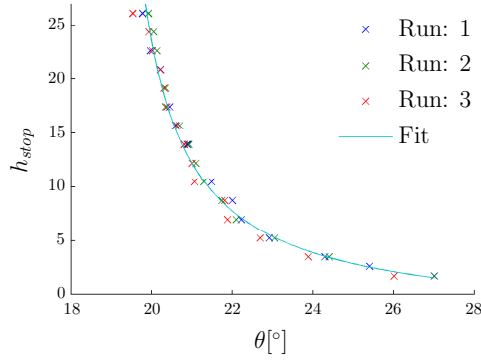
(b) h_{stop} for $\eta = 1/4$, fit to eq. (4.1):
 $A = 1.96, \delta_1 = 18.28^\circ, \delta_2 = 33.02^\circ, E_h = 8.34$



(c) h_{stop} for $\eta = 1/2$, fit to eq. (4.1):
 $A = 2.21, \delta_1 = 18.34^\circ, \delta_2 = 31.92^\circ, E_h = 6.76$



(d) h_{stop} for $\eta = 3/4$, fit to eq. (4.1):
 $A = 1.71, \delta_1 = 18.85^\circ, \delta_2 = 34.12^\circ, E_h = 1.40$



(e) h_{stop} for $\eta = 1$, fit to eq. (4.1):
 $A = 2.26, \delta_1 = 18.70^\circ, \delta_2 = 32.17^\circ, E_h = 3.96$

Figure 4.3: Measured h_{stop} curves for System 1 (see table 4.1): $\eta \in [0, 1/4, 1/2, 3/4, 1]$ with $\sigma^{-1} = \sqrt[3]{2}$ and $\mu_s^p = \mu_l^p$. For every η three runs have been simulated, with different random basal geometries.

The first thing one can notice is that the algorithm is stable, for all plots the three different runs converge to almost the same angle. Also the data is fitted very good with equation (4.1), which is a key observation, since this was not known on beforehand for bi-dispersed flow. In addition to that it should be mentioned that equation (4.1) is ‘just’ an equation that happened to fit the experimental data. There is no physical support or derivation available, so whether the fit works should be carefully assessed each time. Next however it is also clear that all the h_{stop} -curves look very similar. To compare them, in plot 4.4 all the fits are plotted in a single figure, together with the average stopping angles of the three runs for each height.

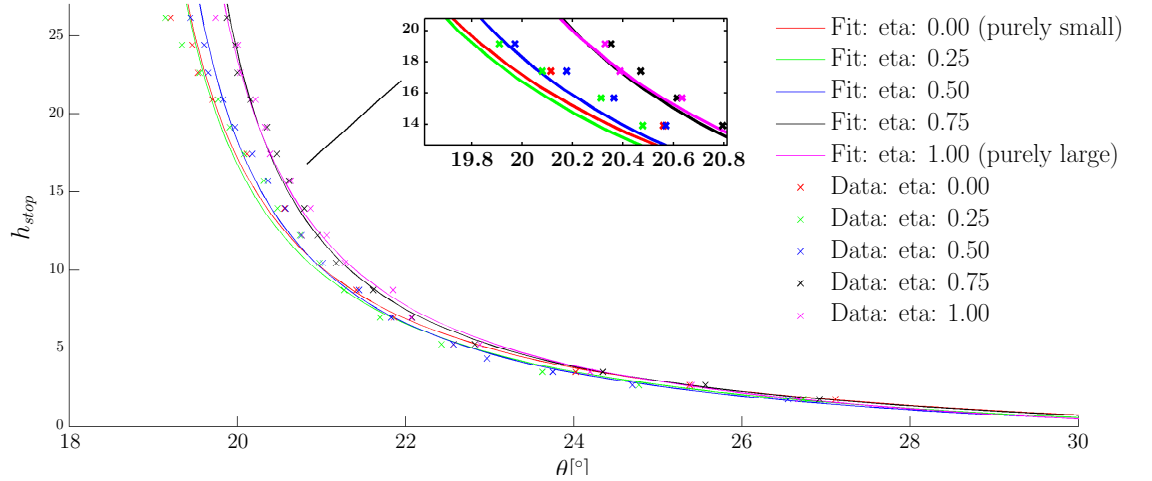


Figure 4.4: h_{stop} -fits for System 1: varying η with $\sigma^{-1} = \sqrt[3]{2}$ and $\mu_s^p = \mu_l^p$, depicted data-points are averages of three runs

Now it is clear how close all the curves are; although (especially for the higher heights) there is a distinct order, it is a very narrow set. The order of the curves is like expected, h_{stop} is higher for higher η , remember that h_{stop} is the height in terms of particle diameters, so a flow of height h of small particles is relatively high compared to a flow with the same (absolute) height with only large particles. Next, since the basal layer is made out of small particles, and for $\eta = 0$ the flow consists of only small particles, that particular system is completely mono-dispersed. Therefore it can be compared with the fit found in [27]. To do this, the fit needs to be scaled, since the particles in [27] have a diameter of unity, whereas small particles in the systems presented here are a factor σ smaller. The resulting scaled fit is plotted together with the fit from [27] in figure 4.5.

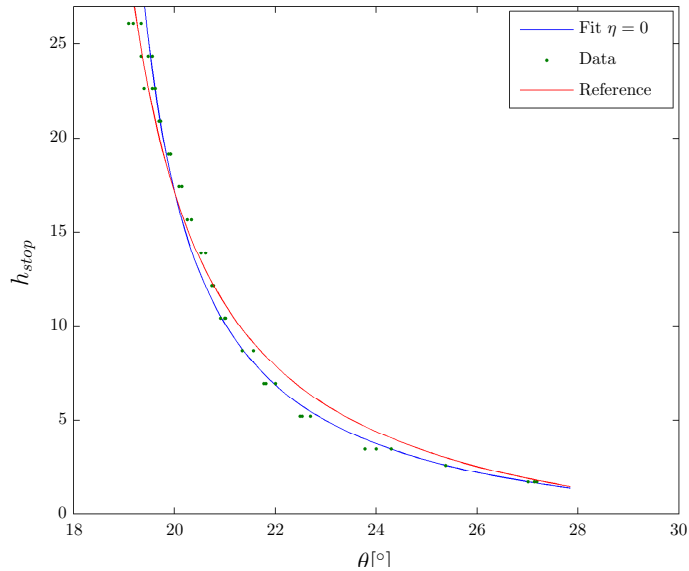
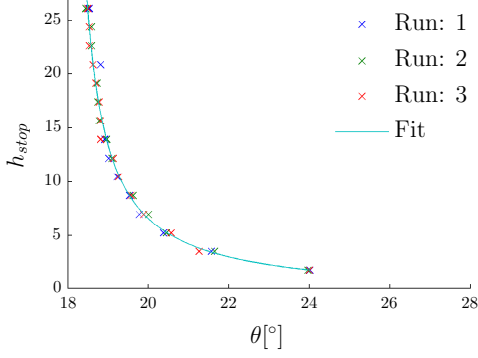


Figure 4.5: h_{stop} fit for $\eta = 0$, the reference fit is from the mono-dispersed system treated in [27]

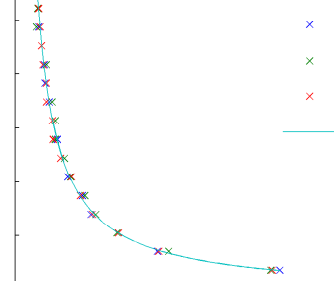
The new results match the results in [27] more or less, which confirms the validity of the h_{stop} -algorithm for bi-dispersed flows.

System 2: Varying volume-ratio η with decreased small particle friction

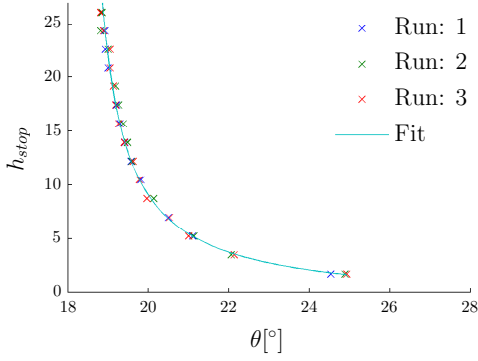
As described in 3.3.2 avalanches with different particle friction coefficients will be compared. So to be able to use the flowrule for the system with a lower particle friction for the small particles, also h_{stop} -curves for that system are required. Therefore, for System 2 (see table 4.1), apart from the different μ_s^p everything is exactly the same as for System 1 in section 4.1.1. The resulting h_{stop} -curves are given in figure 4.6.



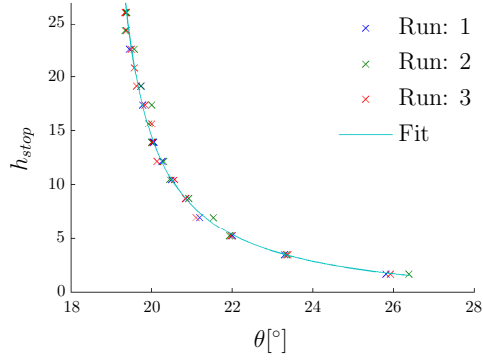
(a) h_{stop} for $\eta = 0$, fit to eq. (4.1):
 $A = 0.67, \delta_1 = 17.92^\circ, \delta_2 = 37.27^\circ, E_h = 1.11$



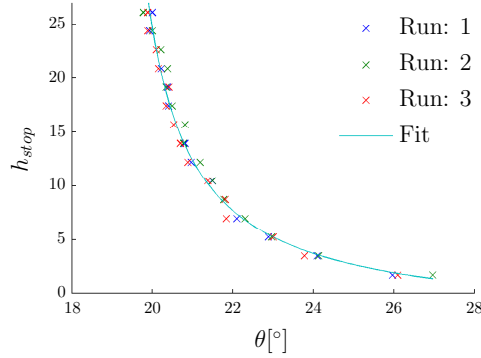
(b) h_{stop} for $\eta = 1/4$, fit to eq. (4.1):
 $A = 0.43, \delta_1 = 18.03^\circ, \delta_2 = 44.26^\circ, E_h = 0.87$



(c) h_{stop} for $\eta = 1/2$, fit to eq. (4.1):
 $A = 0.86, \delta_1 = 18.22^\circ, \delta_2 = 36.02^\circ, E_h = 1.38$



(d) h_{stop} for $\eta = 3/4$, fit to eq. (4.1):
 $A = 1.19, \delta_1 = 18.53^\circ, \delta_2 = 35.47^\circ, E_h = 0.87$



(e) h_{stop} for $\eta = 1$, fit to eq. (4.1):
 $A = 2.45, \delta_1 = 18.78^\circ, \delta_2 = 31.19^\circ, E_h = 1.58$

Figure 4.6: Measured h_{stop} curves for System 2 (see table 4.1): $\eta \in [0, 1/4, 1/2, 3/4, 1]$ with $\sigma^{-1} = \sqrt[3]{2}$ and $\mu_s^p = \mu_l^p/2$.

Again, the fits are remarkably good, the E_h error is even significantly lower compared to the case with equal particle friction coefficients in System 1. The most important effect of changing the particle

friction becomes clear when all fits are plotted together in figure 4.7.

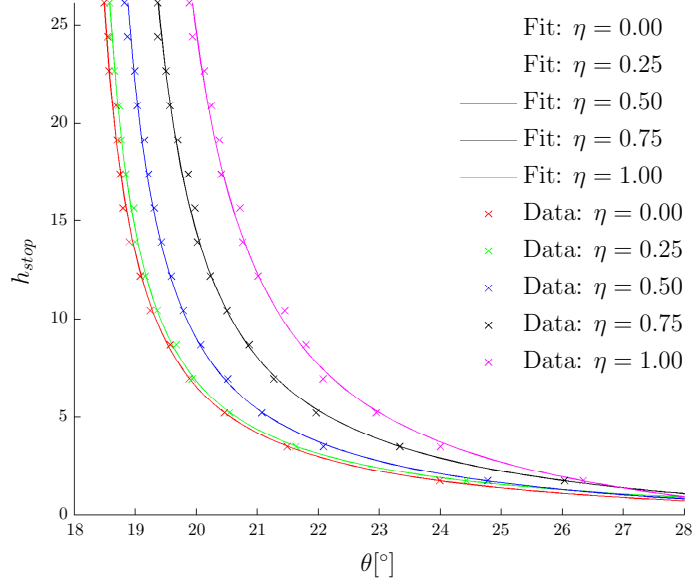
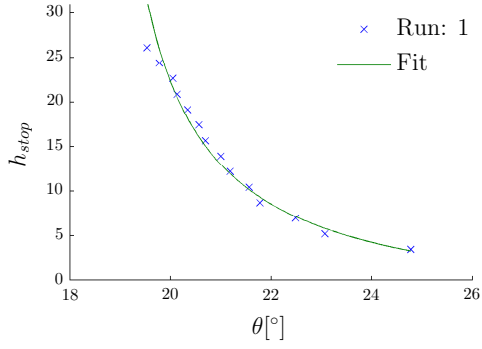


Figure 4.7: h_{stop} -fits for System 2: varying η with $\sigma^{-1} = \sqrt[3]{2}$ and $\mu_s^p = \mu_l^p/2$, depicted data-points are averages of three runs

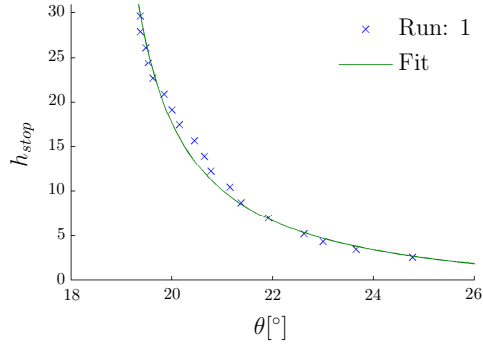
Whereas for the equal friction case in System 1 the spread of the curves was very narrow, now a very clear trend appears. This was expected; with the lowering of μ_s^p the dissipation for the small particles was decreased. Given that the small particles already have a higher flowability than the large particles due to the size difference, the lowering of μ_s^p increases the flowability even further. This explains the now clear distinction between the h_{stop} -curves for different η .

System 3: Varying size-ratio σ

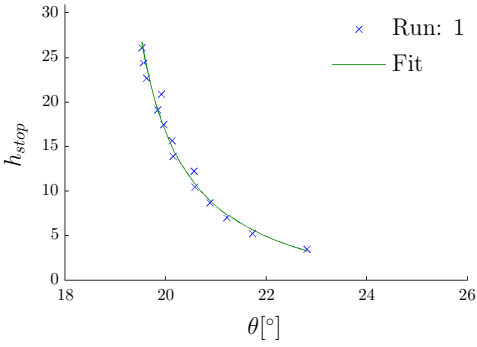
In this section, System 3 is treated, for which instead of η , the size-ratio σ is varied. Again, to limit the parameter space, now $\eta = 1/2$ is fixed. Since this is merely a sidetrack of the thesis (for the quasi 2D avalanche the default $\sigma^{-1} = \sqrt[3]{2}$ is used, hence σ is constant throughout the flow), every height and σ is only ran once. Therefore the fit is less good as for the previous varying η case, it does however give an idea of the general trend.



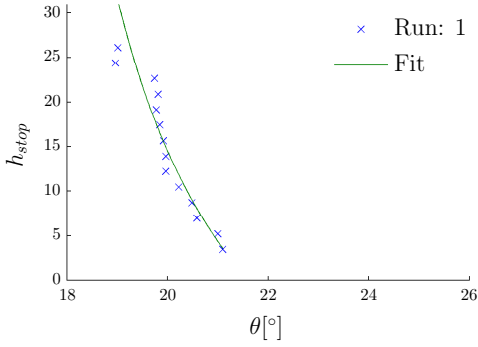
(a) h_{stop} for $\sigma^{-1} = 1.10$, fit to eq. (4.1):
 $A = 3.59, \delta_1 = 18.19^\circ, \delta_2 = 30.30^\circ, E_h = 2.67$



(b) h_{stop} for $\sigma^{-1} = \sqrt[3]{2} \approx 1.26$, fit to eq. (4.1):
 $A = 2.21, \delta_1 = 18.34^\circ, \delta_2 = 31.92^\circ, E_h = 6.76$



(c) h_{stop} for $\sigma^{-1} = 1.5$, fit to eq. (4.1):
 $A = 3.19, \delta_1 = 18.59^\circ, \delta_2 = 26.95^\circ, E_h = 1.13$



(d) h_{stop} for $\sigma^{-1} = 2$, fit to eq. (4.1):
 $A = 34.19, \delta_1 = 16.08^\circ, \delta_2 = 21.61^\circ, E_h = 10.29$

Figure 4.8: Measured h_{stop} curves for System 3 (see table 4.1): $\sigma^{-1} \in [1.1, \sqrt[3]{2}, 1.5, 2]$ with $\eta = 0.5$ and $\mu_s^p = \mu_l^p$.

Although not nearly as good as the fits for the varying η case, there is trend visible when all h_{stop} -curves are plotted in a single figure:

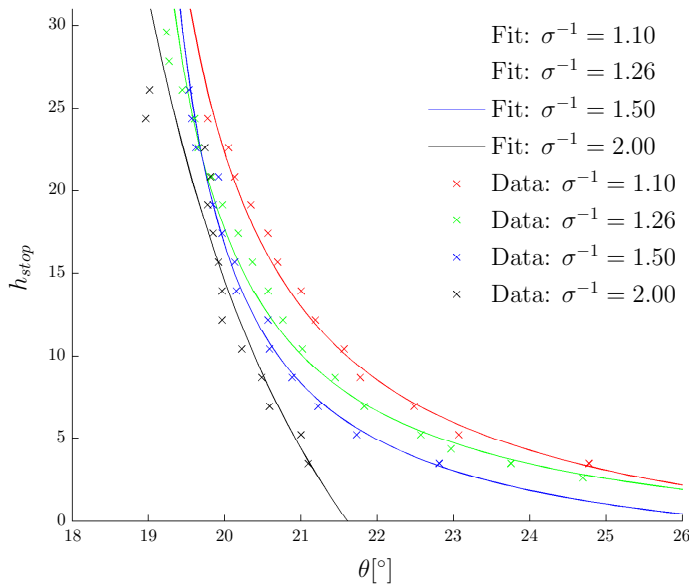


Figure 4.9: h_{stop} -fits for System 3: varying σ with $\eta = 0.5$ and $\mu_s^p = \mu_l^p/2$

As expected, the h_{stop} is higher (the flow is less ‘flowable’) for lower σ^{-1} , which means ‘larger’ small particles. It should be noted however that the fits are not very solid, especially for $\sigma^{-1} = 2$ and for $\theta > 22$ the data is very limited.

Conclusion

Reviewing the results of the h_{stop} algorithm it can be concluded that there is no reason to assume it breaks down for bi-dispersed flows. Also, the decreasing of small particle friction coefficient μ_s^p has a distinct effect on the influence of the concentration η on the h_{stop} -curve. The only problems encountered are with the h_{stop} -curves for varying σ , which is merely a sidetrack of this research. The found h_{stop} -curves do give an idea of the influence of σ , but the data resolution is too low to draw solid conclusions.

4.1.2 Froude flowrule

The next step, having obtained the h_{stop} -curves, is to investigate whether the linear Froude relation of the flowrule, equation (2.117) holds for bi-dispersed flows as well. For this a few steps are required, besides obtaining the h_{stop} -data. First of all, the flowrule should hold for steady flows, so a set of steady flows at different angles and of various heights is needed. These simulations will be done in the same periodic box as the h_{stop} -runs, and for the same three different systems (see table 4.1). The flows will be ran until both the kinetic energy and the segregation profile remain steady (which can take up to 4.000 time units for some flows). Next, both the depth-averaged velocity and the height of these flows are needed to compute the Froude number. Both are easily extracted from the coarse grained statistics, as shown in 2.5.3 and 2.6. In fact, since both the Froude number and flow height can be based on depth-averaged quantities, the statistics are averaged over all three spatial directions (note that the flow is uniform in x and y). The Froude number can then be computed with:

$$F = \frac{\bar{u}}{\sqrt{g \cos(\theta) h}}. \quad (4.6)$$

With this data available it can be investigated whether the Froude number indeed scales linearly with the flow-height divided by h_{stop} :

$$F = \beta \frac{h}{h_{stop}(\theta)} - \gamma. \quad (4.7)$$

And then finally, it is checked whether the flowrule predicts the correct friction coefficient μ , through equation (2.123).

Lithostatic assumption

First of all, for the computation of the flow height as defined in (2.211) to be valid, the downward normal stress component σ_{zz} needs to be lithostatic (i.e the downward normal stress follows equation (2.206)). Since this is not generally true for granular flows, it needs to be checked whether this holds for these chute flows. Therefore, two heights at two different angles are simulated and the stress tensor is observed as a function of z . The statistics are averaged over both x and y , since the latter two dimensions are periodic and hence everything is uniform. The resulting profiles for σ_{zz} and the lithostatic profile are plotted in figure 4.10. Note that the flow height is normalised to unity by scaling the z -direction with the height h .

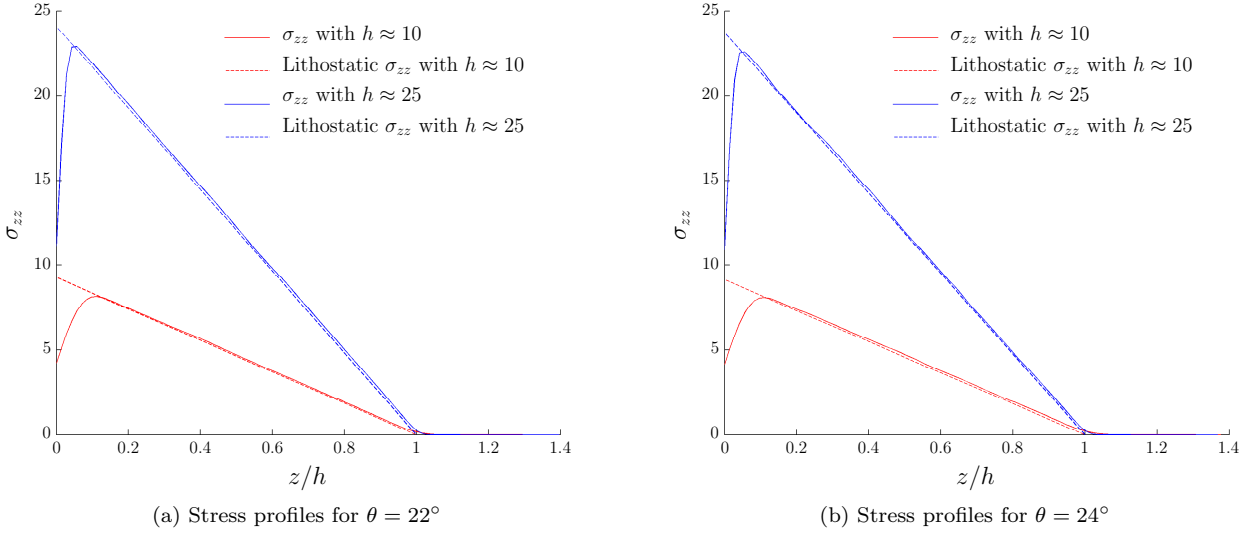


Figure 4.10: Downward normal stress for different flow heights ($h \approx 10$ and $h \approx 25$) at $\theta = 22^\circ$ and $\theta = 24^\circ$. The lithostatic profiles are computed with equation (2.206).

It is clear that the coarse grained statistics nicely capture the lithostatic σ_{zz} component of the stress tensor in the bulk. It is only at the bottom boundary that the coarse graining width w manifests itself through the smearing out of the sharp peak. A smaller w would decrease the smearing out of the peak, but it would also introduce more noise in the bulk. Since the boundary effects do not play a role in the bulk of the flow (i.e. far away from the boundary), it can be concluded that the lithostatic stress assumption is valid.

Fitting the Froude flowrule

As explained in section 2.2, it is expected that the h_{stop} -curve scales the Froude numbers plotted versus $\frac{h}{h_{stop}}$ such that they collapse to a single line for different inclinations and heights. To fit the flowrule MATLAB's `lsqcurvefit()` is used, which simply minimises the sum of the squared residuals for all N_p fitting points:

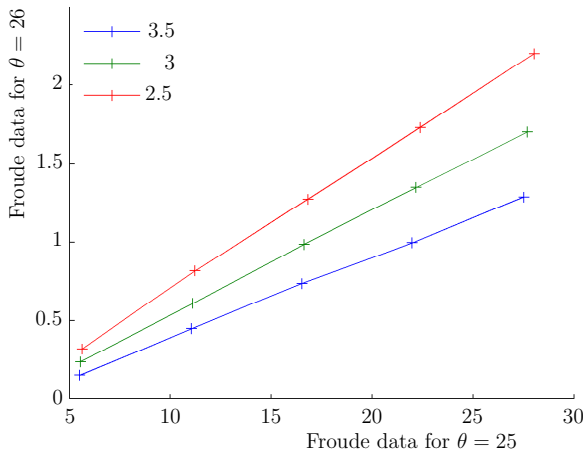
$$E_{total} = \sum_{i=1}^{N_p} (F(h_i) - F_i)^2. \quad (4.8)$$

In this error norm $F(h_i)$ is the Froude number computed with the flowrule $F(h_i) = \beta \frac{h_i}{h_{stop,i}(\theta_i)} - \gamma$, and F_i is the Froude number measured with $F_i = \frac{\bar{u}_i}{\sqrt{g \cos(\theta_i) h_i}}$. To be able to compare the quality of different fits, one can look at the relative error E_f , which is defined as the total error, divided by the number of fitting points (Froude measurements):

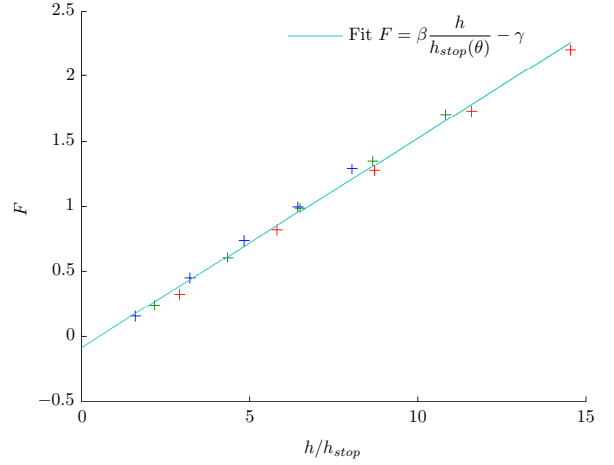
$$E_f = \frac{1}{N_p} \sum_{i=1}^{N_p} (F(h_i) - F_i)^2. \quad (4.9)$$

Sample run Froude simulation

As stated, steady flows will be generated for all three systems in table 4.1 (varying η , varying σ and varying η with reduced μ_s^p), at different heights and chute inclinations. In this section a small example run is shown, which consists of flows of heights ranging from 6 up to 30 large particle diameters, at 24° , 25° and 26° chute angles. The result is a set of Froude numbers, depicted in figure 4.11. The data is from a case with $\eta = 0.5$, $\sigma^{-1} = \sqrt[3]{2}$ and equal particle friction coefficients.



(c) Froude numbers versus flow-height



(d) Scaled Froude numbers and a linear fit

Figure 4.11: Example Froude flowrule data for steady flows with different heights and inclinations and with $\eta = 0.5$, $\sigma^{-1} = \sqrt[3]{2}$, as in System 1 from table 4.1

It is clear that in figure 4.11c the Froude numbers scale linearly with the height, just as has been found for the mono-dispersed case. Also the Froude numbers increase with increasing inclination, as expected. Finally, in figure 4.11d it can be seen that if the height is scaled with the appropriate h_{stop} -curve, the Froude numbers collapse to a linear function. In the following sections the results for the three systems are presented and discussed.

System 1: Varying volume-ratio η

For this case simulations are done at $\theta = [24^\circ, 25^\circ, 26^\circ]$ at heights ranging from approximately 6 up to 30 large particle diameters. Note, the height is an approximation, since the real flow height will depend (slightly) on the flow velocity, which of course depends on the inclination. The real height is computed by equation (2.211). The volume ratio η is varied over the same five values as for the h_{stop} simulations, and all plots are scaled with the appropriate h_{stop} -curve (note that each η has a different h_{stop} -fit). The results are shown in figure 4.12.

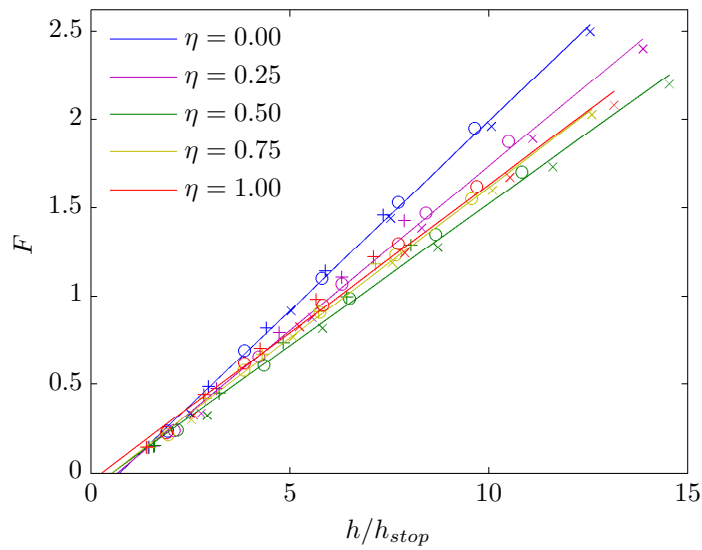


Figure 4.12: System 1: Froude numbers versus flow-height scaled with h_{stop} , colors denote different η , all with $\mu_s^p = \mu_l^p$. Markers denote different chute inclinations: \times : $\theta = 26^\circ$, \circ : $\theta = 25^\circ$ and $+$: $\theta = 24^\circ$

The fit parameters and errors of the different fits are given in table 4.2.

Run	β	γ	E_f
$\eta = 0$	0.251	0.154	$8.9 \cdot 10^{-4}$
$\eta = 1/4$	0.186	0.122	$1.9 \cdot 10^{-3}$
$\eta = 1/2$	0.161	0.084	$1.9 \cdot 10^{-3}$
$\eta = 3/4$	0.170	0.088	$6.8 \cdot 10^{-4}$
$\eta = 1$	0.167	0.044	$2.4 \cdot 10^{-4}$

Table 4.2: Froude fit parameters for varying η

Just as with the h_{stop} -curves in section 4.1.1 the results are rather cluttered. Especially when one notes that a change in h_{stop} directly translates in an equal change in β , and considering that the h_{stop} -curves in figure 4.4 have almost collapsed to a single curve in the region between $\theta = 24^\circ$ and $\theta = 26^\circ$, it is hard to draw any conclusions. However, one can observe that γ is small, and will vanish for $h \gg h_{stop}$ (given equation (4.7): $F = \beta \frac{h}{h_{stop}(\theta)} - \gamma$). Despite the unclear trends in the fit, everything is in place to compute $\mu(F, h)$ for each of the five η cases (i.e all coefficients are known: the A , δ_1 and δ_2 from the h_{stop} -fits, and the β and γ from the Froude-fits). These results are printed in 4.13.

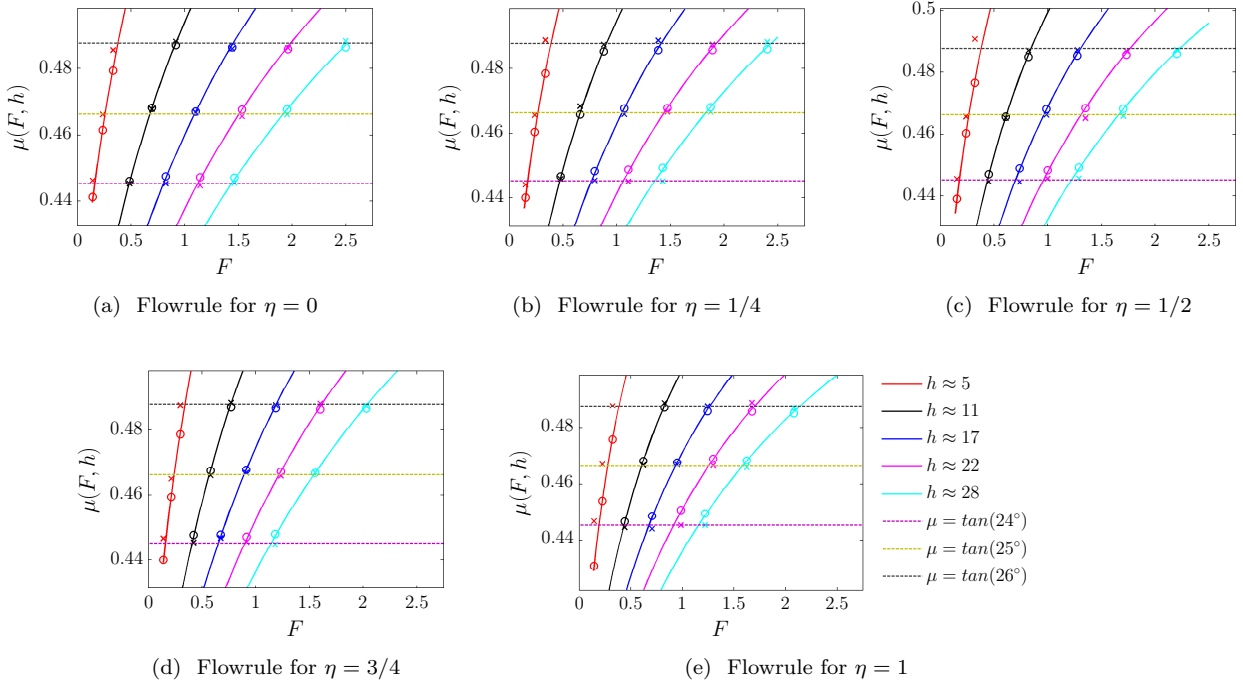


Figure 4.13: Friction law results for varying η and $\mu_s^p = \mu_l^p$, the \times -markers denote measured values for the friction coefficient μ^m , computed as $\mu^m = -\frac{\sigma_{xz}}{\sigma_{zz}}$ (for the definition of the stress tensor see 2.5.2), \circ -markers show $\mu(F, h, \eta)$ computed with the flowrule (which is different for each η and defined in (2.136)). Solid lines show the flowrule $\mu(F, h, \eta)$ for different heights as a function of F , dashed lines show the expected steady state friction coefficient from $\mu = \tan(\theta)$. Also note that the flow height will be slightly different for each inclination, therefore the height used to plot the solid lines $\mu(F, h, \eta)$ is the mean height of the three inclinations used.

The plots above contain a lot of information, but it is clear that the friction coefficients measured from the stress tensor (i.e $\mu^m = -\frac{\sigma_{xz}}{\sigma_{zz}}$) are almost exactly on the lines for $\mu = \tan(\theta)$, the horizontal, dotted lines. That being said, the values for the friction coefficient computed with the flowrule for $\mu(F, h, \eta)$ very closely match the measured values, except for the lowest height. Also important to note is that all figures look very similar, the Froude number belonging to a given height and chute angle

does not differ much for different η . Therefore, for this case with equal particle friction coefficients μ_l^p for the large particles and μ_s^p for the small particles, it can be concluded that the influence of the volume-ratio η is small. This was expected from the fact that in figure 4.4 the h_{stop} -curves for different η are very close together.

System 2: Varying volume-ratio η with decreased small particle friction

This section contains the flowrule results for the second system, in which η is varied and the particle friction of the small particles, μ_s^p is reduced. Given the h_{stop} -curves fitted in 4.1.1, the Froude numbers for a set of steady flows ranging in height from 6 up to 30 and at angles of 24° , 25° and 26° are computed and scaled with the appropriate h_{stop} -fit. The Froude-fit is depicted in figure 4.14, and the corresponding fit-parameters are given in table 4.3.

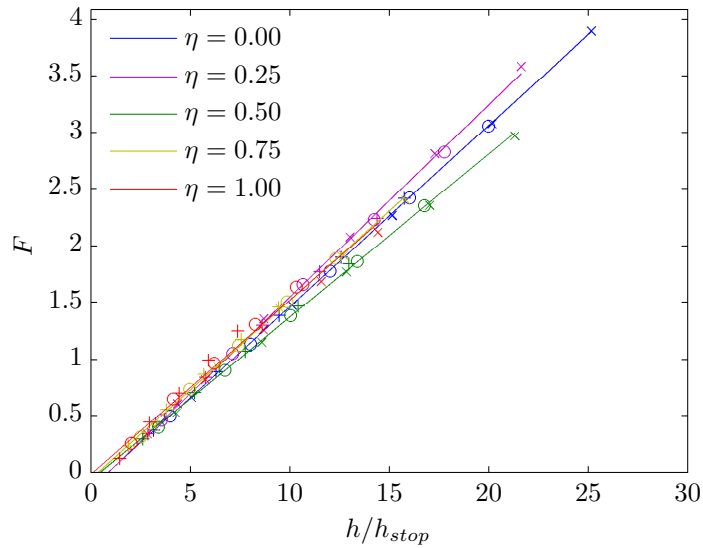


Figure 4.14: Froude numbers versus flow-height, colours denote different η , all with $\mu_s^p = \mu_l^p/2$. Markers denote different angles: \times : $\theta = 26^\circ$, \circ : $\theta = 25^\circ$ and $+$: $\theta = 24^\circ$

Run	β	γ	E_f
$\eta = 0$	0.160	0.139	$1.7 \cdot 10^{-4}$
$\eta = 1/4$	0.169	0.154	$8.7 \cdot 10^{-4}$
$\eta = 1/2$	0.143	0.067	$5.1 \cdot 10^{-4}$
$\eta = 3/4$	0.153	0.057	$5.9 \cdot 10^{-4}$
$\eta = 1$	0.154	0.019	$4.7 \cdot 10^{-3}$

Table 4.3: Froude fit parameters for varying η with $\mu_s^p = \mu_l^p/2$

Here an interesting phenomena can be observed; the h_{stop} -curves for this case are better fitted than for the first system, and they show a wider spread for varying η (figure 4.7). The Froude-fit however, collapses almost to a single line. Whereas the β values (the slope of the linear fit) showed a little spread for the first case with equal particle friction coefficients, the curves are now very close. Although this is an interesting result it is difficult to draw any conclusions, since the exact physical meaning of the β parameter is poorly understood.

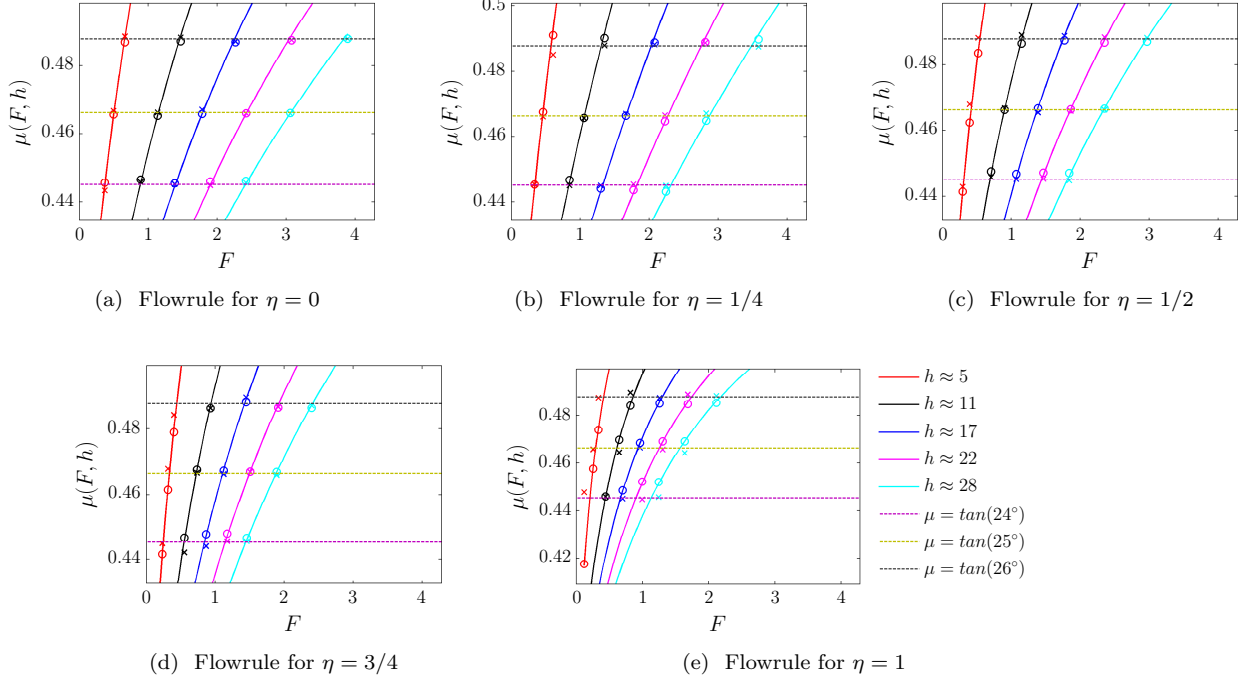


Figure 4.15: Friction law results for varying η and $\mu_s^p = \mu_l^p/2$, the \times -markers denote measured values for the friction coefficient μ^m , computed as $\mu^m = -\frac{\sigma_{xz}}{\sigma_{zz}}$ (for the definition of the stress tensor see 2.5.2), \circ -markers show $\mu(F, h, \eta)$ computed with the flowrule (which is different for each η and defined in (2.136)). Solid lines show the flowrule $\mu(F, h, \eta)$ for different heights as a function of F , dashed lines show the expected steady state friction coefficient from $\mu = \tan(\theta)$. Also note that the flow height will be slightly different for each inclination, therefore the height used to plot the solid lines $\mu(F, h, \eta)$ is the mean height of the three inclinations used.

Again, just as for the first case the friction law shows rather good agreement with the measurements. The results for $\eta = 1$ diverge for the lowest height, which is explainable since this case did have the largest error in the Froude-fit (table 4.3). Also, similarly as for the case with equal particle friction, the results for the lowest heights are off. That being said, the results are still very close to the measured values for μ^m . Another interesting point is that the curves differ significantly for varying η . Unlike for the case with equal particles friction coefficients μ_s^p and μ_l^p in section 4.1.2, here the decreased small particle friction μ_s^p has made the influence of the volume ratio of the two phases much more pronounced. Of course this was expected from the h_{stop} -curves for this case (figure 4.7), which also showed a very clear trend for varying η . Given this result, it is expected that for the quasi 2D avalanches the case with the low μ_s^p will give the most interesting results.

System 3: Varying size-ratio σ

For the case with varying size-ratio σ there is a problem, since the h_{stop} curves obtained are not fitted very well (see figure 4.8). Especially in the range of angles used for the steady flows in this section (24° , 25° and 26°) the available h_{stop} -data is just not sufficient, most noticeable for the $\sigma^{-1} = 2.0$ case, where $\delta_2 = 21.61^\circ$, such that h_{stop} is not even defined for the angles used. From figure 4.16 however, it can be seen that steady flow is possible for these angles and $\sigma - 1 = 2$: the flow does not accelerate indefinitely and the segregation becomes steady as well.

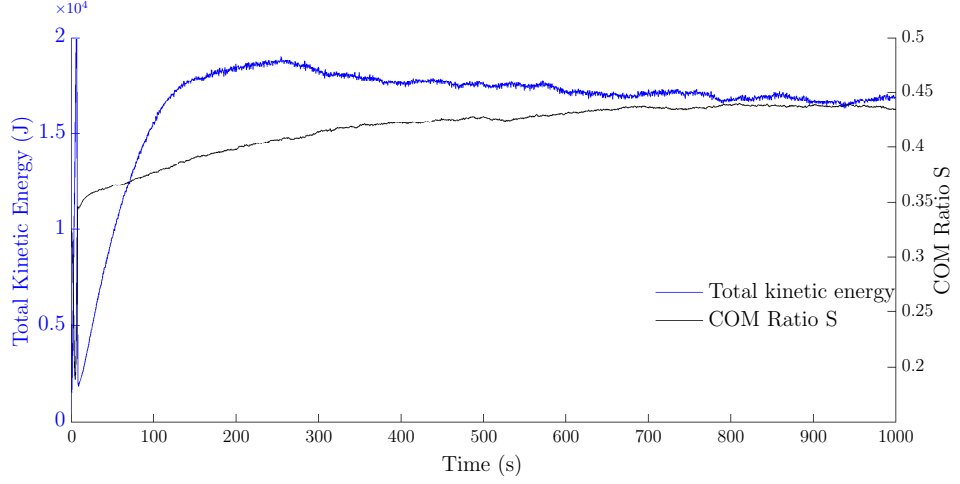


Figure 4.16: Total kinetic energy and volume ratio S for a flow with $\sigma^{-1} = 2$ and $\theta = 26^\circ$ the height is approximately 12 large particle diameters.

Therefore the case with $\sigma^{-1} = 2$ will be discarded, and analysis will be continued with the other three cases, even though there as well the h_{stop} -data is not as good as for the two cases for varying η . The procedure is exactly similar to the previous sections, steady flows are generated for the different σ values, keeping the volume-ratio constant at $\eta = 1/2$. The resulting Froude-fit is shown in figure 4.17, and the fit-parameters are given in table 4.4.

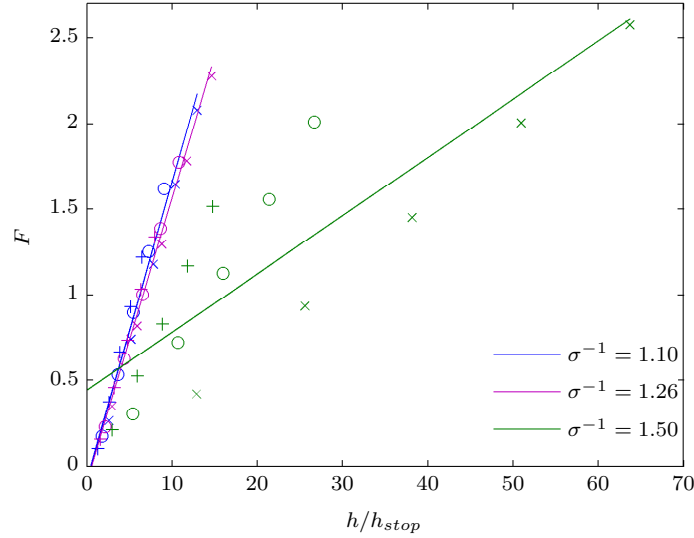


Figure 4.17: Froude numbers versus flow-height scaled with h_{stop} , colours denote different σ , markers denote different angles: \times : $\theta = 26^\circ$, \circ : $\theta = 25^\circ$ and $+$: $\theta = 24^\circ$

Run	β	γ	E_f
$\sigma^{-1} = 1.1$	0.175	0.084	$7.8 \cdot 10^{-3}$
$\sigma^{-1} = \sqrt[3]{2}$	0.166	0.091	$3.1 \cdot 10^{-3}$
$\sigma^{-1} = 1.5$	0.034	-0.430	$1.2 \cdot 10^{-1}$

Table 4.4: Froude fit parameters for varying σ

From the fit parameters and figure 4.17 a couple of things can be noted. First of all, for $\sigma^{-1} = 1.1$ and $\sigma^{-1} = \sqrt[3]{2}$ the fit works rather well. Error norms are in the same range as for the varying η cases, and the Froude numbers nicely collapse to a single line. For the $\sigma^{-1} = 1.5$ case however, things are

different. The Froude numbers do not scale at all to a linear fit, which indicates that not only the magnitude of h_{stop} in the $\theta = 24^\circ \dots 26^\circ$ range is wrong, but that also the shape of the h_{stop} curve is wrong in that area. From figure 4.9 this can be explained, there is simply no h_{stop} data in the $\theta = 24^\circ \dots 26^\circ$ range. A possible solution to work around this problem is to make use of the assumption that the Froude numbers scale linear for the fit of the h_{stop} curves as well. This can be done by fitting both h_{stop} and the Froude-flowrule in one go, minimising errors for both fits. This method is further explained in section 4.1.2.

Combined fit of h_{stop} and the Froude flowrule

From the previous results it can be concluded that the assumption that Froude numbers collapse to a linear function of the height when scaled with h_{stop} still holds for bi-dispersed flows. There were however some issues with the fits, especially for the varying σ case in System 3. In this section a solution for this problem will be presented. This solution is based on the assumption that the Froude-flowrule does hold. So instead of fitting the h_{stop} curves, checking whether that h_{stop} curve does scale the Froude numbers like expected and then fitting a linear Froude versus h/h_{stop} profile, it becomes possible to do both fits in a single step. This way, h_{stop} is fitted with information from the Froude-flowrule as well, i.e. the h_{stop} -fit is curved such that it scales the Froude numbers linearly. It should be emphasised that this is major assumption. However, from the previous results in which the fits were done separately it can be concluded that when the h_{stop} -fit is sufficiently good, the Froude numbers indeed scale linearly with the flow height, and the only deviation from the flowrule that is observed can be explained by a lack of fit quality for the h_{stop} -curve. Therefore, in the results as presented in the previous sections there is no reason to doubt the validity of the Froude-flowrule for bi-dispersed flows. To be able to fit the both profiles in one step a combined error norm is needed, which can be used with MATLAB's minimisation toolbox to compute the optimal fit. Therefore the two different error norms (equations (4.4) and (4.8)) are simply summed:

$$E_{combined} = \sum_{i=1}^{N_h} (\theta_i - 16)^2 (h_{stop}(\theta_i) - h_i)^2 + \sum_{i=1}^{N_f} (F(h_i) - F_i)^2 \quad (4.10)$$

Here N_h denotes the number of h_{stop} data-points, and N_f denotes the number of Froude flowrule fitting points, which of course can and will be different. First, System 2, the case for varying η with reduced small particle friction μ_s^p will be fitted with this combined fit. This case was fitted very good as well with the separate fits, so it can be used to verify whether the combined fit works and gives the same result. The resulting h_{stop} curves for both fit methods are depicted in figure 4.18, and the resulting fit parameters (for both h_{stop} and $F(\frac{h}{h_{stop}})$) are given in table 4.5.

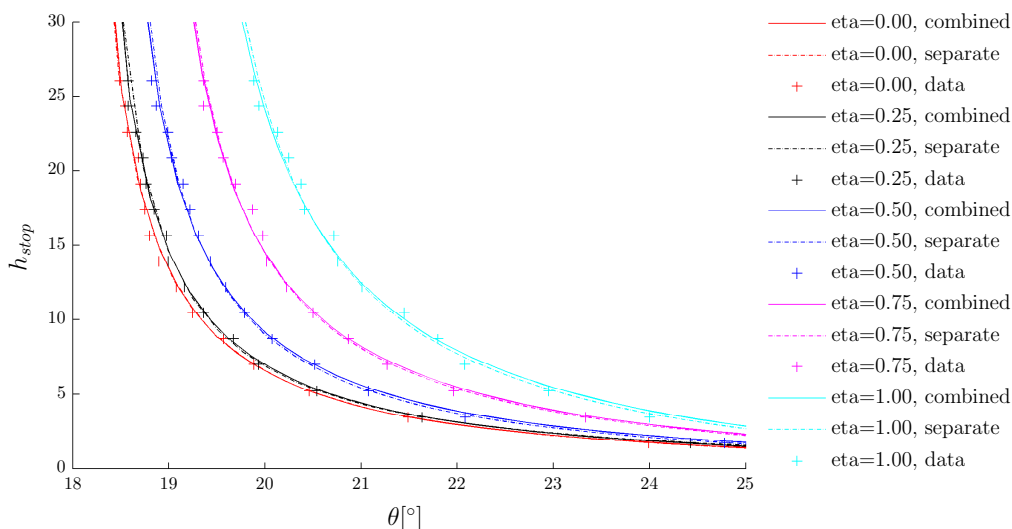
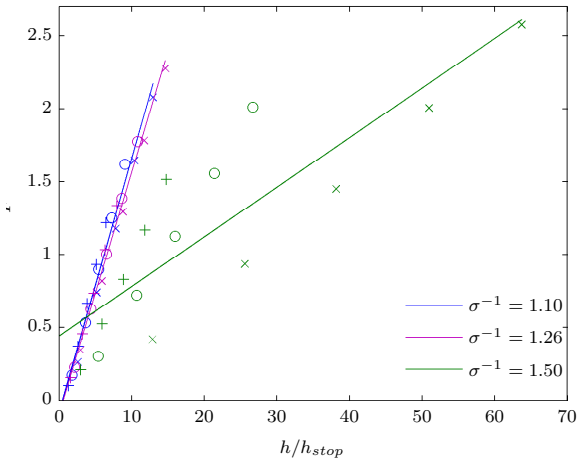


Figure 4.18: h_{stop} -curves for System 2, with varying η and reduced μ_s^p , comparing h_{stop} -curves fitted separately with curves fitted jointly with the Froude fit

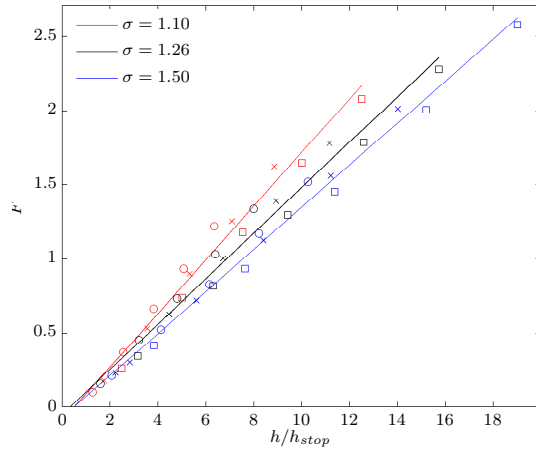
	A	δ_1	δ_2	β	γ	E_h	E_f
η	Separate fits						
0.00	0.67	17.92	37.27	0.160	0.139	0.6119	0.0108
0.25	0.43	18.03	44.26	0.170	0.153	0.5475	0.0242
0.50	0.86	18.22	36.02	0.144	0.067	0.6891	0.0194
0.75	1.19	18.53	35.47	0.157	0.057	0.6053	0.0213
1.00	2.45	18.78	31.19	0.154	0.019	0.8561	0.0618
η	Combined fits						
0.00	0.63	17.93	38.06	0.163	0.146	0.6024	0.0079
0.25	0.57	18.00	39.95	0.163	0.137	0.5440	0.0096
0.50	1.07	18.14	34.18	0.140	0.047	0.5796	0.0368
0.75	1.44	18.45	33.86	0.153	0.042	0.5739	0.0332
1.00	3.08	18.60	30.04	0.144	-0.016	0.7805	0.0834

Table 4.5: h_{stop} and Froude fit parameters for varying η with lower μ_s^p , including error norms E_h and E_f for the h_{stop} -fit and the Froude-flowrule fit respectively.

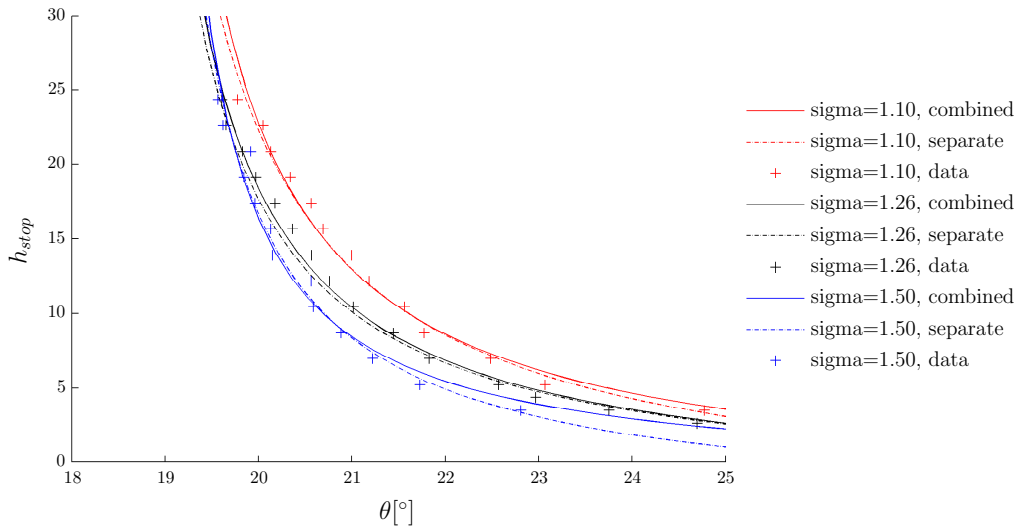
Although there are minor variations in the fit parameters the five coefficients are in general very close. Also one should keep in mind that a small variation in the height of the h_{stop} -curve translates directly in a change in the values for β . Next the combined fitting procedure is tried on the flowrule data for varying σ . Due to a lack of a sufficient number of data points this fit failed for the separate fitting procedure (figure 4.17). The result of the combined fit are given in figure 4.19 and table 4.6.



(a) Froude fits for varying σ , h_{stop} and $F(h/h_{stop})$ are fitted separately



(b) Froude fits for varying σ , h_{stop} and $F(h/h_{stop})$ are fitted combined



(c) h_{stop} -curves for varying σ , comparing h_{stop} -curves fitted separately with curves fitted together with the Froude fit

Figure 4.19: Combined h_{stop} and Froude number fits for System 3, with varying σ , $\eta = 0.5$ and $\mu_s^p = \mu_l^p$. One can see that where the separate fitting procedure fails, the combined fit does work for the $\sigma = 1.5$ case

From 4.19c it can be seen that whereas the combined and separate fitting procedures yield almost identical results for $\sigma^{-1} = 1.1$ and $\sigma^{-1} = 1.26$, the two methods diverge for the $\sigma^{-1} = 1.5$ case for $\theta > 23^\circ$. This is a clear case of the h_{stop} curve ‘bending’, to satisfy the linearity of the Froude flowrule, which is possible since there is no h_{stop} data at $\theta > 23^\circ$. The resulting fitting coefficients are given in table 4.6 below.

	A	δ_1	δ_2	β	γ	E_h	E_f
σ^{-1}	Separate fits						
1.10	3.59	18.19	30.30	0.175	0.084	0.6950	0.0773
1.26	2.21	18.34	31.92	0.166	0.091	0.7498	0.0484
1.50	3.19	18.59	26.95	0.034	-0.440	0.7803	0.2907
σ^{-1}	Combined fits						
1.10	3.48	18.23	30.54	0.181	0.092	0.6059	0.0719
1.26	2.70	18.30	30.60	0.153	0.054	0.6218	0.0740
1.50	1.55	18.73	32.13	0.142	0.072	0.9249	0.0523

Table 4.6: h_{stop} and Froude fit parameters for varying σ , including error norms E_h and E_f for the h_{stop} -fit and the Froude-flowrule fit respectively.

In table 4.6 the fitting coefficients for $\sigma^{-1} = 1.1$ and $\sigma^{-1} = 1.26$ are in general very close, for $\sigma^{-1} = 1.5$ however the fit is completely different, with a huge reduction in the error for the Froude-fit (E_f) for the combined procedure. The conclusion is that the combined fit procedure is a valuable method to improve the h_{stop} -fit in places with little data. An important note however is that the results of the combined fitting procedure do depend on the way the combined error is formulated. If one would weigh E_f and E_h differently, one can in the limit recover the separate fits for either the separate h_{stop} -fit or the separate Froude-fit.

Fit trends

Since the data for the case with varying η and decreased μ_s^p has the most distinct features and the best fit, some interesting trends for this case will be treated in this section. For this the combined fitting procedure is used, since this will yield the most stable results. From the combined fit coefficients in table 4.5 it can be seen that the γ value changes quite a lot. Therefore it is interesting to see what happens when this value is fixed at $\gamma = 0$. Although this is a bit of a shot in the dark, there is a motivation. So far the linear Froude fit work really well, but it is known [27] that the data will diverge for low Froude values. This is because for $h < h_{stop}$ every flow will arrest, such that there are no Froude numbers $F > 0$ for $h/h_{stop} < 1$. Therefore, it is expected that the Froude numbers ‘curve down’ at $h/h_{stop} = 1$, instead of going through the origin. This might be an explanation for the unclear trends in the values for γ , and it is an motivation to try the combined fit with $\gamma = 0$. The results for this new fit (for System 2, with varying η and reduced μ_s^p) are given in table 4.7.

	A	δ_1	δ_2	β	γ	E_h	E_f
η	Combined fits						
0.00	0.71	17.92	36.53	0.148	0.000	0.6113	0.0548
0.25	0.64	17.99	38.41	0.149	0.000	0.5478	0.0489
0.50	1.09	18.14	33.92	0.136	0.000	0.5762	0.0424
0.75	1.45	18.45	33.76	0.148	0.000	0.5731	0.0366
1.00	3.07	18.60	30.06	0.146	0.000	0.7810	0.0840

Table 4.7: h_{stop} and Froude fit parameters for System 2, with varying η and $\gamma = 0$, including error norms E_h and E_f for the h_{stop} -fit and the Froude-flowrule fit respectively.

First the error-norms, for all η the errors E_h in the h_{stop} -fits are almost equal to the errors for the fit including γ in table 4.5. For the error of the Froude fit, E_f , it is only the first two cases ($\eta = 0$ and $\eta = 0.25$) that suffer from the fixing of $\gamma = 0$, the other cases have similar errors as in the fit with γ . This is expected since the first two cases had the largest values for γ . The values for β for the first two cases however did get closer to the other values for β , supporting the hypothesis that for this case β is independent of the volume ratio η . Furthermore, trends in A , δ_1 and δ_2 become more clear. First of all, A seems to increase significantly with increasing η , which is expected, because of the scaling effect (i.e, small particles flow better for the same absolute flow height), which causes the h_{stop} -curve to be shifted up to higher heights for increasing η . Next, there are the two angles δ_1 and δ_2 . Thinking of these, one can think of the left boundary, δ_1 to be kinetic in nature. It is the arresting limit for flows with a high height, in which for most of the particles the rough bottom is ‘far away’ (this can also be seen from table 1 in [27], in which δ_1 is up to far extend almost independent of the bottom

roughness). Therefore, a flow of height h with only small particles ($\eta = 0$), will flow at (slightly) lower angles (again, small particles have better flow-ability for the same height than large particles) than a flow of height h with only large particles. At the upper limit however, at δ_2 , it is the other way around, here large particles flow easier because the rough bottom (of small particles) is relatively smooth for them. Therefore, an imaginary flow with $h \rightarrow 0$ will flow only at $\theta \approx > 36^\circ$ for pure small particles. It will however start to flow already at $\theta \approx > 30^\circ$ for a purely large flow.

Conclusion

Given the results for the Froude-fits it can be concluded that the linear scaling for F with h/h_{stop} works perfectly, not only for mono-dispersed, but also for bi-dispersed, steady flows. It is only for the very low heights and Froude numbers that the results deviate from the fit, which is expected since the flowrule is known to break down here (since there is no flow possible for $h < h_{stop}$ Froude should go to zero as $h/h_{stop} \rightarrow 1$). For the higher heights the Pouliquen law predicts the steady state friction up to a good accuracy.

4.2 Quasi 2D avalanche flow

Where the previous sections focussed on steady flow, in this section developing granular flows are considered. Therefore a quasi 2D domain will be used, as described in 3.3. This section starts with a short insight in the way the flow develops over time in 4.2.1. Thereafter equation (2.211) is used to compute the flow height, and the location of the front is defined in 4.2.2. This gives an insight in the macroscopic shape of the avalanche. Finally, the $\mu(h, F, \eta)$ -flowrule, for which the necessary fit parameters are obtained in sections 4.1.1 and 4.1.2, is used to predict the friction coefficient as a function of the flow variables in section 4.2.3. This gives a friction coefficient as a function of t and x (since the flows are depth-averaged and uniform in y), and the computed friction coefficient $\mu(t, x)$ is compared with the friction coefficient $\mu^m(t, x)$ measured from the stress tensor. For all quasi 2D systems the particle size ratio is fixed at $\sigma^{-1} = \sqrt[3]{2}$ and the relative volume ratio of the large phase is fixed at $\eta = 0.5$ for the steady inflow domain. In this section three different avalanches will be considered: one with equal particle friction coefficients μ_l^p and μ_s^p for the large and small particles, and two with a reduced μ_s^p . The parameters for these three cases are given in table 4.8.

	t_{eval}	h_{inflow}	μ_l^p	μ_s^p	μ_{ls}^p	θ	η_{inflow}	σ^{-1}
Avalanche 1: $\mu_l^p = \mu_s^p$	800	≈ 8	0.5	0.5	0.5	24°	0.5	$\sqrt[3]{2}$
Avalanche 2: $\mu_l^p > \mu_s^p$	800	≈ 8	0.5	0.25	0.375	24°	0.5	$\sqrt[3]{2}$
Avalanche 3: $\mu_l^p > \mu_s^p$, double h_{inflow}	800	≈ 16	0.5	0.25	0.375	24°	0.5	$\sqrt[3]{2}$

Table 4.8: Simulation parameters for the three different quasi 2D avalanches.

The parameter t_{eval} gives the time (in nondimensional simulation time units) at which the statistics are evaluated. The statistics for all avalanches consist of the time-average of 1.000 timesteps, spanning 10 time units, starting at t_{eval} , as explained in 3.3.3.

4.2.1 Developing avalanche fronts

The inflow conditions as defined in 3.3.1 will ‘push’ a steady flow of small and large particles into the avalanche domain. Since the top half of the periodic inflow domain consists mainly of large particles and has a larger velocity than the bottom half, the mass-flux of large particles flowing into the domain will be larger than that of small particles. Also, the large particles will automatically be transported to the front of the flow due to their greater velocity. In this section the development of such flows will be quantitatively visualised. Treated first is Avalanche 1, with equal particle friction coefficients, and the inflow consists of 800 large particles, and 1600 small particles, giving a height at the inflow of approximately 8 large particle diameters. A couple of snapshots of different timesteps for this avalanche are given in figure 4.20.

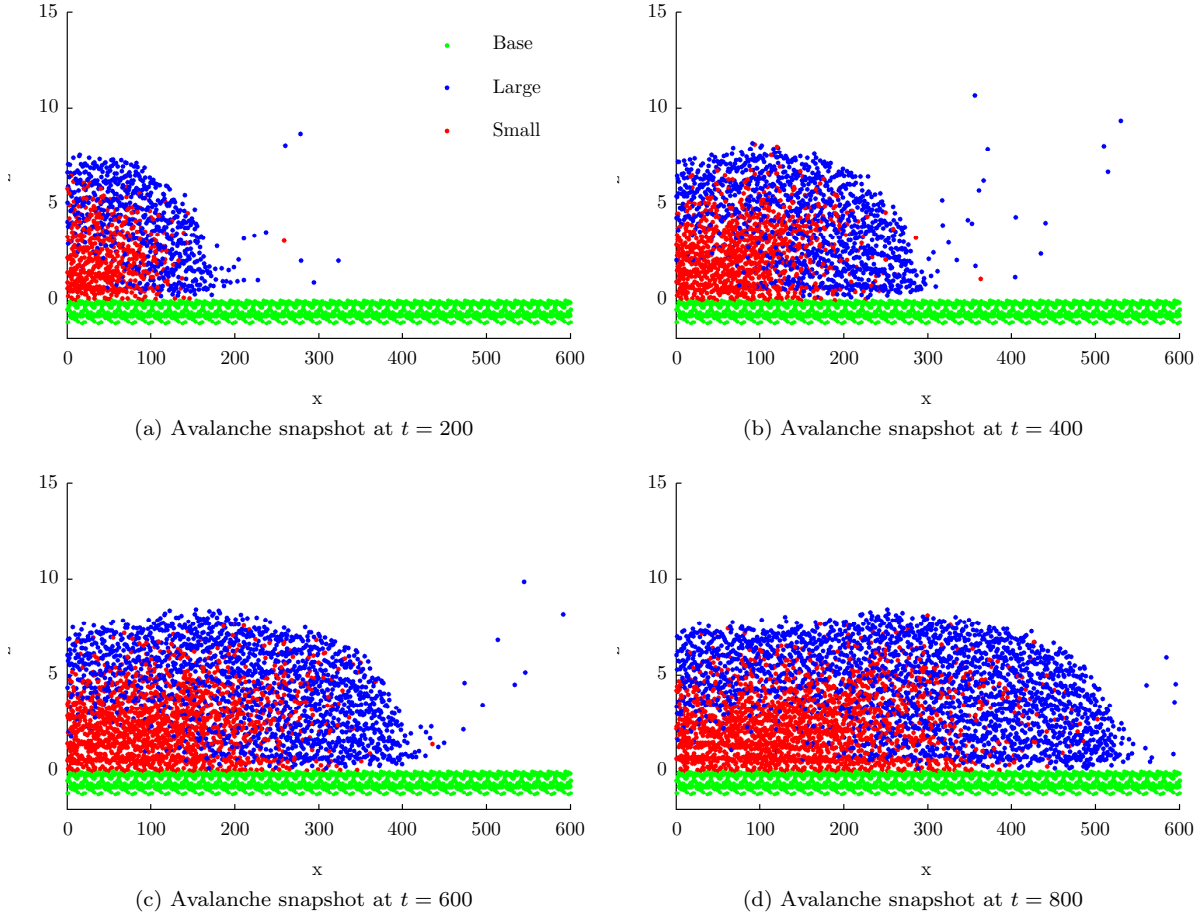


Figure 4.20: Snapshots for Avalanche 1 in table 4.8. Different timesteps are printed, ranging from $t = 200$ up to $t = 800$. Avalanche 1 has equal particle friction coefficients for the large and small particles.

Although these plots only give qualitative results, one can see that the flow develops a ‘bulbous’ head at the front, where the height is slightly larger, and over time the front grows richer and richer of large particles. Just as for the case with equal particle friction coefficients, a similar simulation has been done for Avalanche 2, the case where the small particle friction coefficient μ_s^p is reduced as explained in 3.3.2. For this flow similar snapshots are printed in 4.21.

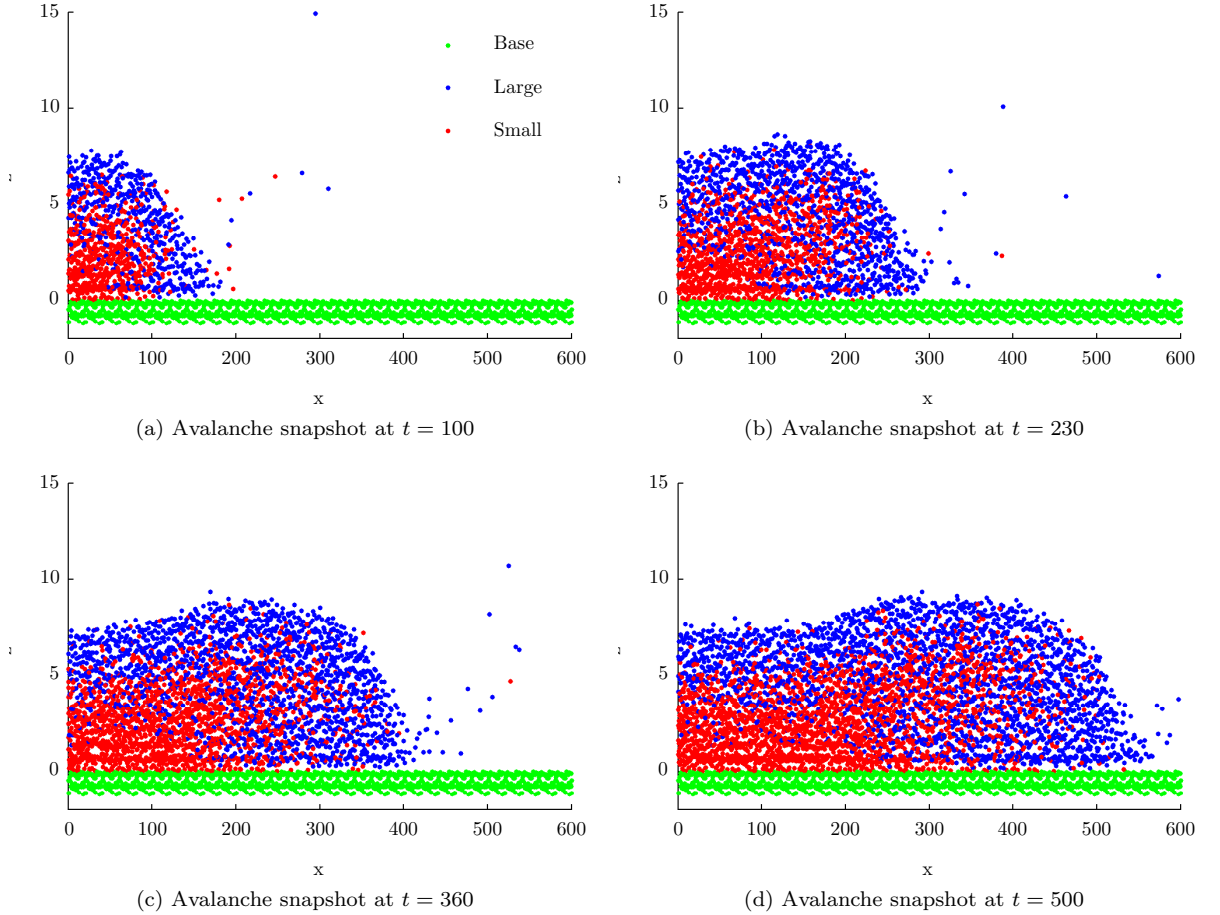


Figure 4.21: Snapshots for Avalanche 2 in table 4.8. Different timesteps are printed, ranging from $t = 100$ up to $t = 500$. Here μ_s^p is reduced, in line with 3.3.2.

First, note the different times at which the snapshots are taken compared to figure 4.20. The reduction of μ_s^p made the flow quicker (less dissipation through friction), so to get the front in (approximately) the same position as in figure 4.20 it is necessary to look at earlier times. Furthermore, the bulbous head is more pronounced for the low μ_s^p case, which is caused by the large particles being relatively more frictional, and thus slowing down the flow when they reach the front. Since the bulk of the flow behind the head wants to go quicker, the height is pushed up there. In the rest of the results this will be the more interesting case since the influence of the concentration is larger due to the relatively high friction for the large particles, which can also be seen from the h_{stop} -results.

4.2.2 Flow height and flow front definition

The flow height is again computed as the ratio of the depth averaged downward normal stress and the depth averaged density, as defined in (2.211). Whereas the periodic box simulations allowed the averaging of the statistics in x -direction, this is not possible for the quasi 2D avalanches. The result is a height profile which is a function of the x -direction. Since the statistics for the periodic box do not only have more data through averaging in x -direction, but also through time-averaging (as explained in 3.3.3), the first thing to assess is the capability of the definition for the flow-height to mark the real height, even with much less data available. Therefore a snapshot of the particle positions and the resulting flow-height is plotted below, such that it can be visually confirmed that the flow-height is correct. Note that the depth averaged normal stress and the depth averaged density are computed with the coarse graining parameters as defined in 3.3.3, with spatial averaging over both the z and y -direction.

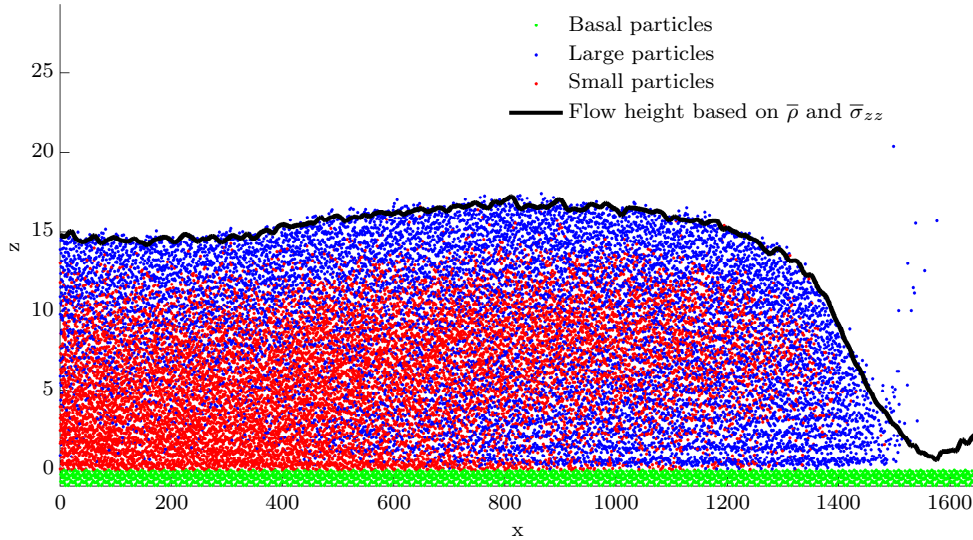


Figure 4.22: Particle positions for a cross-section of an simulation which shows the height as defined in equation (2.211). Parameters are set as defined for Avalanche 3 in table 4.8

From 4.22 it can be seen that the height as defined in (2.211) nicely tracks the free-surface. It is only at the very front, where particles start to saltate, that the definition breaks down. This however is not a problem for the application in this thesis, since the flowrule is only valid inside the flow (for example the density is assumed to be constant, which is not the case for the saltating particles at the front). To demarcate the region in which the flowrule is valid, a definition of the location of the front is needed. Although many definitions are possible, it was chosen to define the front by means of the Froude number. Recall that the Froude number is given in (2.116) as:

$$F = \frac{\bar{u}}{\sqrt{g \cos(\theta) h}}. \quad (4.11)$$

At the very front the particle velocities become very large, and the height goes down sharply. This will yield a sharp increase in the Froude number. An example of the Froude number and the flow-height is depicted in 4.23

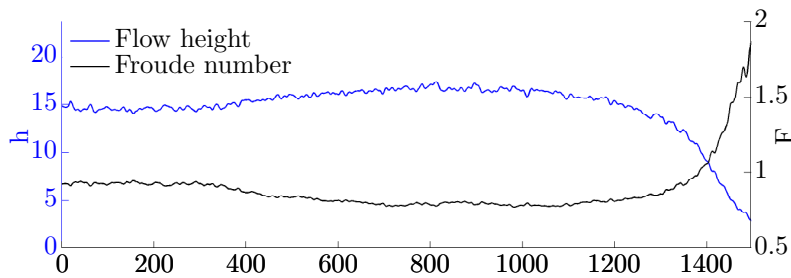


Figure 4.23: Example plot with Froude and the flow height versus x . This is a simulation of Avalanche 3. At the very front of the flow a sharp increase in the Froude number can be observed

In all the following analysis the front is defined to be at the point where the Froude number reaches two times the value of F_{inflow} , being the average Froude number in the inflow-region:

$$x_{front} = \min_{F(x) > 2F_{inflow}}(x). \quad (4.12)$$

4.2.3 Applying the $\mu(h, F, \eta)$ -flowrule

In this section all results come together. With the flowrule $\mu(F, h, \eta)$ in place it is possible to predict the friction coefficient as a function of the flow-variables F , h and η in the quasi 2D flows. Note that

the flowrule is a continuous function of h and F , but not of η . Instead, the fit parameters needed are computed for a discrete set, $\eta \in [0, 1/4, 1/2, 3/4, 1]$. Hence, the dependency on η is through a linear interpolation of the flowrule between values of η for which the flowrule fit coefficients are computed in sections 4.1.1 and 4.1.2. This linear interpolation is given in (2.136). All results are presented in terms of depth-averaged quantities that are plotted against the x -coordinate.

Avalanche 1

The first avalanche that was simulated was that with an inflow height of approximately eight large particle diameters. An intuitive way to look at the evolution of the large and the small phase throughout the avalanche length is to plot the fraction of the height occupied by small particles and large particles respectively. This can be done simply by multiplying the flow height with the local $\eta(x)$ for the large phase, and $1 - \eta(x)$ for the small phase. So the height h_s for the small particles and h_l for the large particles becomes (recall that $\bar{\rho}$ denotes the depth-average density):

$$h_s(x) = (1 - \eta(x))h(x), \quad (4.13)$$

$$h_l(x) = \eta(x)h(x), \quad (4.14)$$

$$\text{With: } \eta(x) = \frac{\bar{\rho}_l(x)}{\bar{\rho}_s(x) + \bar{\rho}_l(x)}. \quad (4.15)$$

This then gives the height occupied by each phase, as depicted in 4.24, note that the height of the large phase is ‘stacked’ on that of the small phase, as if the two are separated by a sharp interface.

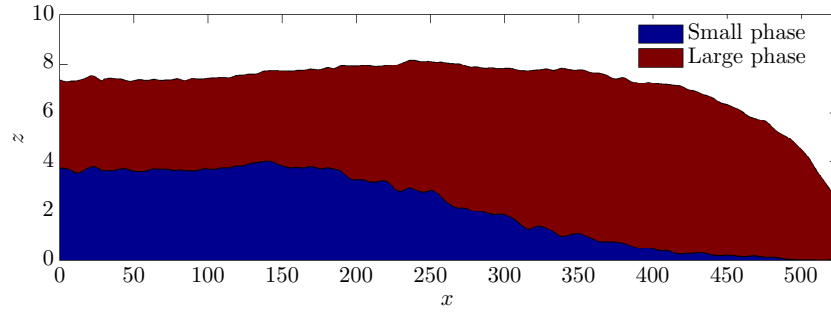


Figure 4.24: Area plot showing the large and small phase for the first avalanche, the large phase is summed on top of the small phase, such that the height in this plot reflects the total height of the flow.

First of all, it is important to keep in mind that in the avalanche the two phases have mixed region. From the plots showing the large and small particles positions (i.e figure 4.22) it is obvious that there is no such thing as a sharp interface between the two phases. However, figure 4.24 does give a nice insight in the development of the relative volume fraction of the both phases throughout the flow. Also, the depth-averaged shallow layer model for which the friction coefficient is needed does not (in its form as presented in 2.1) incorporate the shape of the concentration profile in the z -direction. From figure 4.24 it is clear that the inflow’s $\eta = 0.5$ is advected into the flow domain, and that at the very front the flow develops a pure phase of large particles. Now, for the computation of the friction coefficient it is also meaningful to look at the Froude number and the height versus x , since those are two of the parameters involved in the flowrule for the friction coefficient, as previously defined in equation (2.123):

$$\mu^\eta(F, h) = \tan(\delta_1) + \frac{\tan(\delta_2) - \tan(\delta_1)}{\frac{\beta h}{A * d(F + \gamma)} + 1}, \quad \eta \in [0, 1/4, 1/2, 3/4, 1]. \quad (4.16)$$

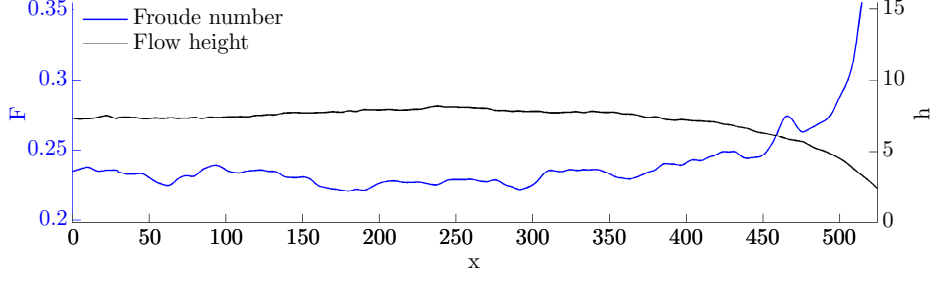


Figure 4.25: Two parameters needed for $\mu(F, h, \eta)$, the Froude number and the height of the flow.

With the height, the Froude number, and the volume ratio η available for every x the friction coefficient can be computed as defined in (2.136):

$$\mu(F, h, \eta) = \frac{\eta_1 - \eta}{\eta_1 - \eta_0} \mu^{\eta_0}(F, h) + \frac{\eta - \eta_0}{\eta_1 - \eta_0} \mu^{\eta_1}(F, h). \quad (4.17)$$

With η being the local volume ratio, and η^0 and η^1 being the two closest volume ratios for which there is flowrule data (i.e $\eta_0, \eta_1 \in [0, 1/4, 1/2, 3/4, 1]$) such that $\eta_0 < \eta < \eta_1$.

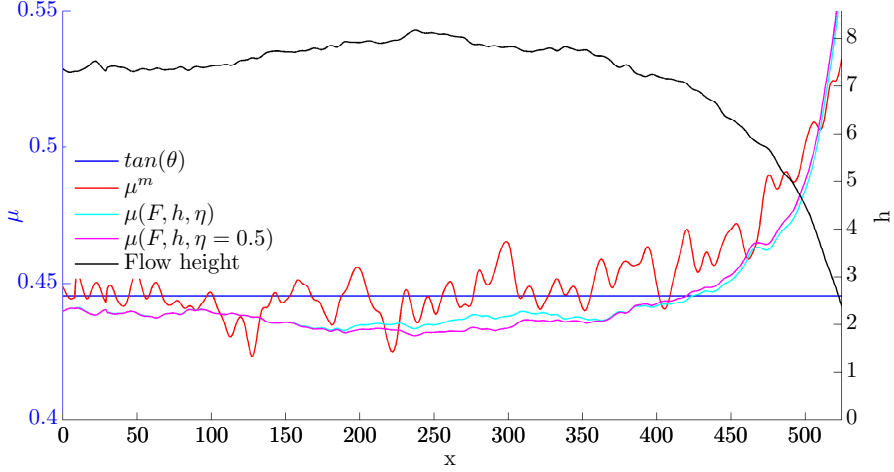


Figure 4.26: Depicted are the values of the friction coefficient throughout the flow for Avalanche 1 with $\mu_s^p = \mu_l^p$. The height is shown as reference, μ^m is the friction as measured from the stress tensor, $\mu(F, h, \eta)$ is the friction predicted with the flowrule. For comparison, $\mu(F, h, \eta = 0.5)$ is the friction as predicted by the flowrule with a fixed volume ratio $\eta = 0.5$, therefore neglecting the influence of the volume-ratio. Lastly, also $\tan(\theta)$ is graphed, the steady state friction for this chute-angle.

The resulting friction coefficient $\mu(F, h, \eta)$ is plotted as a function of x in figure 4.26 and can be compared with the measured friction μ^m . First of all, the flowrule does predict the increase in friction at the flow-front. This can be explained with the Froude and height profiles in 4.25 and equation (4.16): an increasing Froude-number combined with a decrease in height always increases the friction coefficient (if of course the fit parameters are constant, which they are if η is constant, which is the case in the front region $x > 400$, where $\eta \rightarrow 1$ as can be seen from figure 4.24). Second, there is a notable error in the predicted friction coefficient in the steady region for $x < 100$. This can be explained with the steady state friction predictions from section 4.1.2. From figure 4.13c, (reprinted here in figure 4.27), it can be seen that the $\mu(F, h, \eta)$ consequently underpredicts the friction for the lowest height (the left most red curve). Since this lowest height is roughly 5 large particle diameters and the avalanche considered here has an inflow of height 8, the error is to be expected.

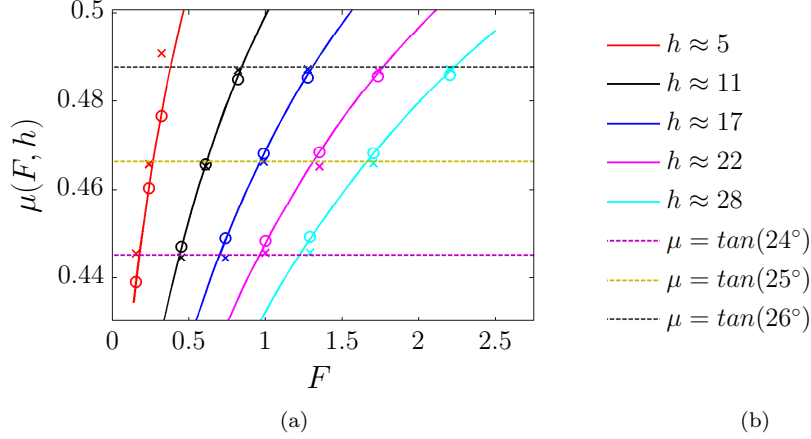


Figure 4.27: Steady state friction coefficient predictions as printed in 4.13, for $\eta = 1/2$. The \times -markers denote measured values for the friction coefficient μ^m , computed as $\mu^m = -\frac{\sigma_{xz}}{\sigma_{zz}}$, \circ -markers show $\mu(F, h, \eta)$ computed with the flowrule. Solid lines show the flowrule $\mu(F, h, \eta)$ for different heights as a function of F , dashed lines show the expected steady state friction coefficient from $\mu = \tan(\theta)$. It can be seen that the error grows pretty large for the lowest height, which is roughly 5 large particle diameters and thus close to the avalanche height of 8 in figure 4.26.

Summarising, it can be concluded that the flow-rule does produce friction coefficients which show similar behaviour as the measured friction, but as a result of the fit inaccuracy due to the low height there is a significant error. Also, for this case with $\mu_l^p = \mu_s^p$ the effect on the friction of the varying concentration in the flow is barely visible.

Avalanche 2

The second avalanche has the same inflow as the first case, but the particle friction for the small particles μ_s^p is reduced. Two effects result from this, first of all the flow is faster, due to a decrease in friction losses. Second, it makes the large particles relatively more frictional, which is shown to increase the effect of η on the flowrule in section 4.1.2.

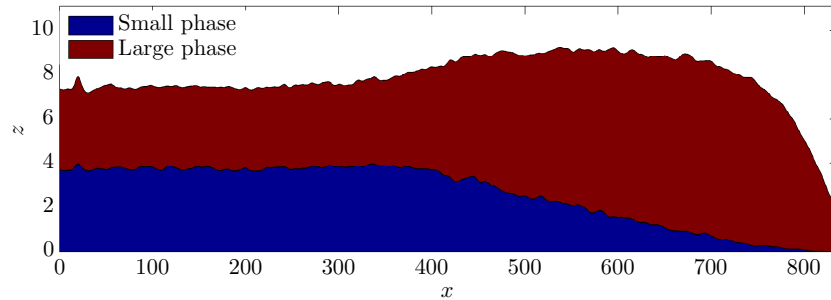


Figure 4.28: Area plot showing the large and small phase for the first avalanche, the large phase is summed on top of the small phase, such that the height in this plot reflects the total height of the flow.

Comparing the area plot in figure 4.28 with that for the second avalanche (figure: 4.24) there are two important differences. First of all there is the location of the front. Noting that both the first and second avalanche are depicted at $t = 800$, it can be seen that the reduction of μ_s^p has made the avalanche significantly quicker (the front for the first avalanche is roughly at $x = 550$, for the second case it is at $x = 850$). Second, the reduction of μ_s^p increased the height of the bulbous head, a result of the large particles at the front being relatively more frictional.

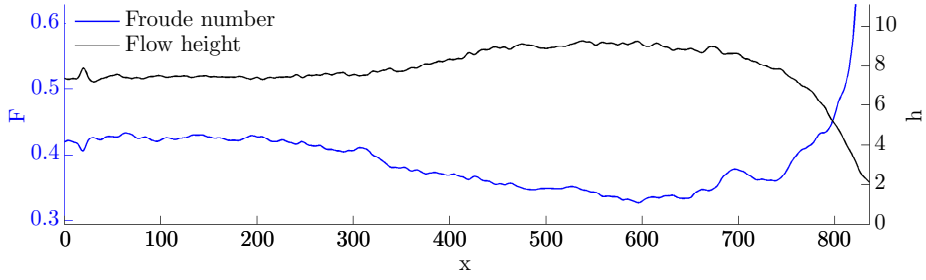


Figure 4.29: Two parameters needed for $\mu(F, h, \eta)$, the Froude number and the height of the flow.

From 4.29 it can be concluded that this case also has a more interesting Froude-profile compared to the first avalanche. It can clearly be seen decreasing as the height increases, this can be explained: as the height increases, the average velocity decreases, both have the effect that the Froude number decreases. However, from equation (4.16) it can be seen that Froude going down and the height going up would yield an immediate decrease in the friction. This would then speed up the flow again, which in turn would lower the height. Since this does not happen, there is something that increases the friction, which supports the weight of the bulbous head. The source of this increase in friction is in the large concentration of (relatively frictional) large particles, keeping the bulbous head in shape.

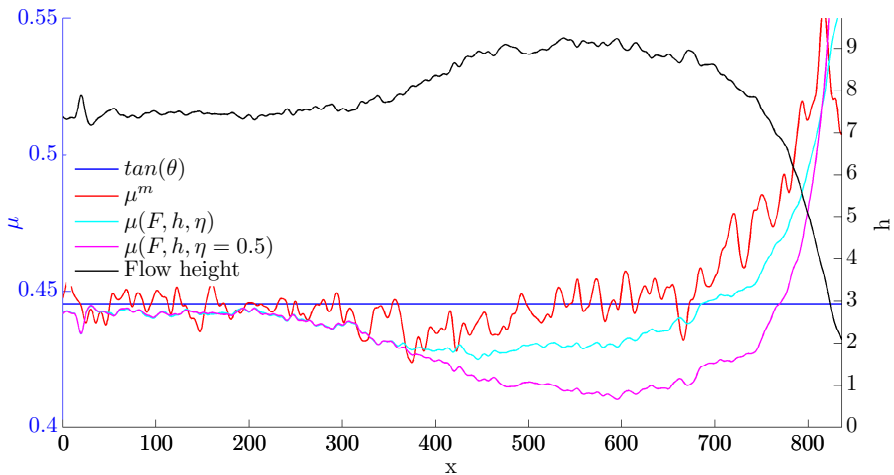


Figure 4.30: Depicted are the values of the friction coefficient throughout the flow for Avalanche 2, with $\mu_s^p = \mu_l^p/2$. The height is shown as reference, μ^m is the friction as measured from the stress tensor, $\mu(F, h, \eta)$ is the friction predicted with the flowrule. For comparison, $\mu(F, h, \eta = 0.5)$ is the friction as predicted by the flowrule with a fixed volume ratio $\eta = 0.5$, therefore neglecting the influence of the volume-ratio. Lastly, also $\tan(\theta)$ is graphed, the steady state friction for this chute-angle.

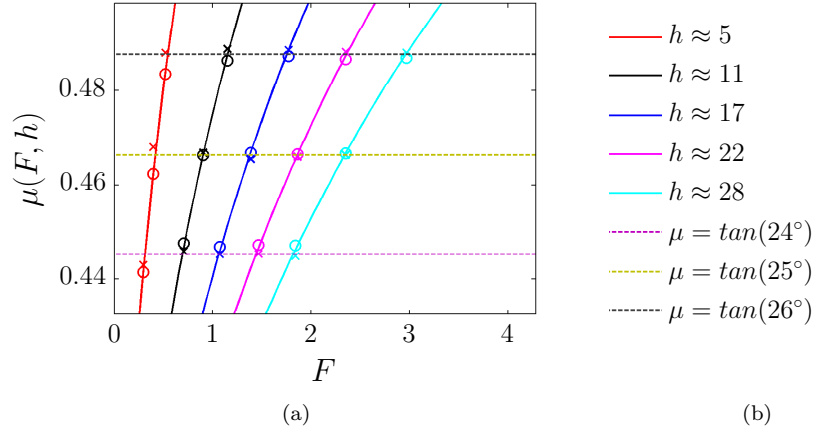


Figure 4.31: Steady state friction coefficient predictions as printed in 4.15, for $\eta = 1/2$ and with reduced μ_s^p . The \times -markers denote measured values for the friction coefficient μ^m , computed as $\mu^m = -\frac{\sigma_{xz}}{\sigma_{zz}}$, \circ -markers show $\mu(F, h, \eta)$ computed with the flowrule. Solid lines show the flowrule $\mu(F, h, \eta)$ for different heights as a function of F , dashed lines show the expected steady state friction coefficient from $\mu = \tan(\theta)$. Comparing with figure 4.27, it can be seen that for this case with $\mu_s^p = \mu_l^p/2$ the predicted friction for a height of 8 (which is in between the red and black curves) is slightly better, explaining why the second avalanche has a better prediction of the friction in the steady region for $x < 200$.

From 4.30, it can be seen that the friction law predicts the measured friction pretty well, and now also the importance of taking the volume ratio into account becomes clear, the predicted friction for constant $\eta = 0.5$ clearly is way to low. However, the predicted value for the friction is still too low compared to the measured value, although it does come close. Also the prediction in the steady region for $x < 200$ is better, which can be seen from the plot in 4.31. Also for the steady state the prediction of the friction coefficient is better for the low heights, compared with 4.27 for the equal particle friction case.

Avalanche 3

The final avalanche has the same particle properties as the second one, but here the inflow has twice as many particles, doubling the avalanche height. Since one of the problems of the first two avalanches was the relatively low height, for which the error in the $\mu(F, h, \eta)$ flowrule is rather large, this avalanche is expected to show a better prediction of the friction. Of course, doubling the height has two effects which increase the computational effort required, it has double the particles in the z -direction, and it is also much quicker, greatly increasing the number of particles flowing into the domain.

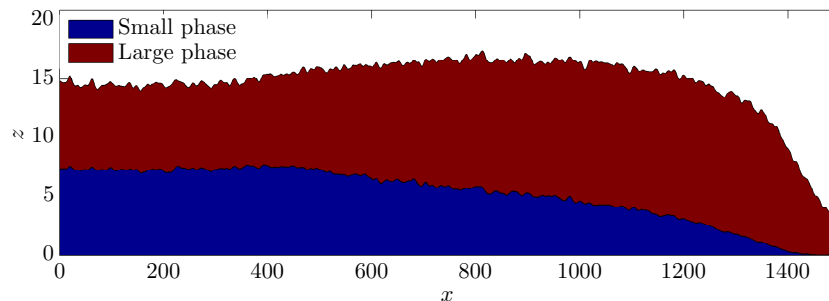


Figure 4.32: Area plot showing the large and small phase for the third avalanche, the large phase is summed on top of the small phase, such that the height in this plot reflects the total height of the flow.

Figure 4.32 looks similar as for the first two cases, except of course the doubling of the inflow height. The head shows a similar shape as for the second avalanche. Also it should be noted that this avalanche is significantly longer than the first two, due to the increase in flow velocity.

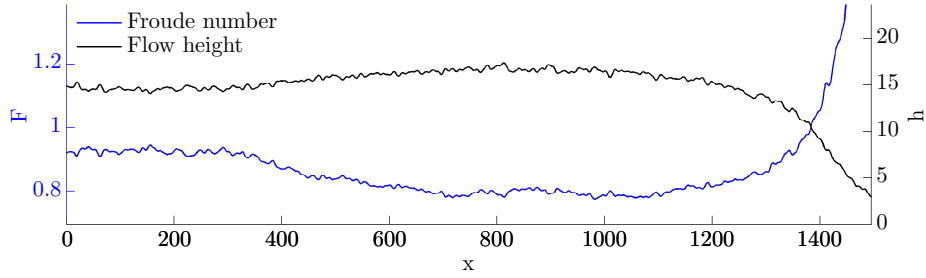


Figure 4.33: Two parameters needed for $\mu(F, h, \eta)$, the Froude number and the height of the flow.

Qualitatively the Froude profile in figure 4.29 looks very similar to that of the second avalanche in figure 4.29. A similar decrease in the head is observed, which again can be explained by the increasing height and decreasing depth-averaged velocity.

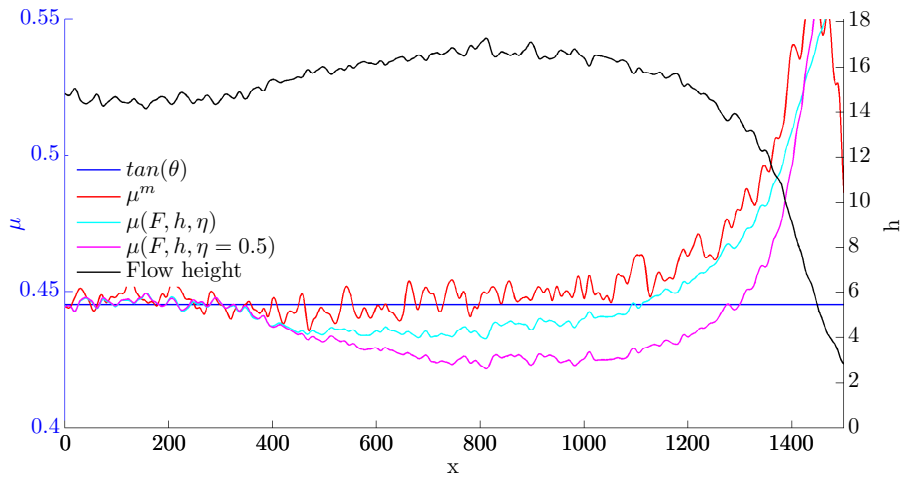


Figure 4.34: Depicted are the values of the friction coefficient throughout the flow for Avalanche 3 with $\mu_s^p = \mu_l^p/2$. The height is shown as reference, μ^m is the friction as measured from the stress tensor, $\mu(F, h, \eta)$ is the friction predicted with the flowrule. For comparison, $\mu(F, h, \eta = 0.5)$ is the friction as predicted by the flowrule with a fixed volume ratio $\eta = 0.5$, therefore neglecting the influence of the volume-ratio. Lastly, also $\tan(\theta)$ is graphed, the steady state friction for this chute-angle.

First thing to note from 4.34 is that now the steady state friction for $x < 300$ is correctly predicted. Whereas the first two cases showed a significant error here, for this case the increase in height shifted the flowrule into the domain where the steady state predictions are pretty accurate (see figure 4.31, a height of 15 large particle diameters corresponds roughly to the dark blue curve). However, the prediction of the friction in the head is still to low. A possible explanation for this effect is given in the next paragraph.

Conclusion

Reviewing all three avalanches, one important deviation in the prediction of $\mu(F, h, \eta)$ is that it is always too low in the bulbous head. This can be explained. The friction law is valid for *segregated* flows, with a specific η . However, in the front, the flow is a combination of a segregated flow *on top* of a layer of large particles that have reached the front of the flow and are being overrun. This can clearly be seen from figure 4.22, which shows how the large particles reach the front and then end up at the bottom of the flow. So in the front the flow develops a layer of large particles at the base. Now instead of over a relatively smooth layer of small particles, the flow has to move over a layer of frictional large particles, slowing the flow down. The flowrule on the other hand, does not incorporate this effect and is only a function of (depth-averaged) volume-ratio η . Therefore, the avalanche is slower than it should be according to the flowrule, which results in a lower predicted friction coefficient: according to the

flowrule the flow should accelerate. Therefore, to predict the friction with a higher accuracy in this region, the transient phenomena of the segregation profile should be taken in to account. This can also be seen from figure 3.5, which is reprinted in figure 4.35.

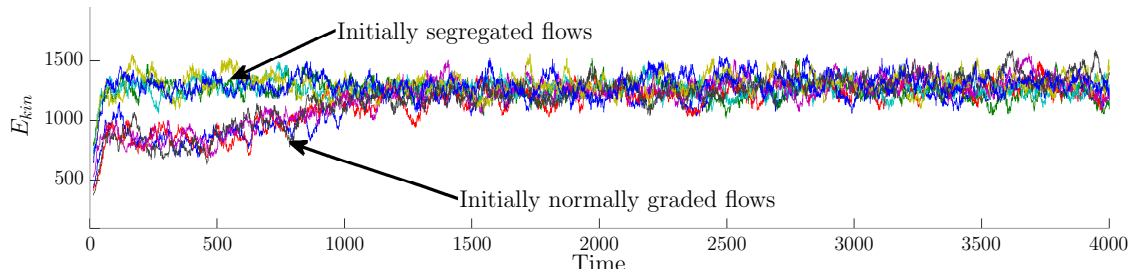


Figure 4.35: Total kinetic energy for initially normally graded (small on top of large) and segregated (large on top of small) flows.

For the initially normally graded flows it can be seen that for $t < 1000s$ the kinetic energy is significantly lower than for the segregated flows, thus the latter are quicker. This explains why the avalanche front, which is not in a steady segregated state experiences the higher friction, and the flowrule, which assumes steady segregation underestimates the friction for the given height and Froude number.

Chapter 5

Conclusion and recommendations

5.1 Conclusion

The Pouliquen friction law allows to predict the friction coefficient that appears in the depth averaged shallow layer equations, in terms of flow variables, being the Froude number F and the flow-height h . Research initially focussed on mono-dispersed flows, which does not allow the modelling of the segregation phenomena that are present in bi-dispersed chute flows. In this thesis, I aimed to extend the Pouliquen friction law to the domain of bi-dispersed flows. The necessary experiments to validate my approach were done numerically, since physical experiments are in general very difficult or even impossible for the granular systems considered. To investigate the problem, I formulated two main research questions:

- Can the Pouliquen friction law be applied to predict the macroscopic friction in steady, bi-dispersed chute flows?
- Can the friction law be applied to predict the friction in bi-dispersed avalanche fronts, incorporating the effect of the different mixtures throughout the flow?

To start with the first research question, this involved two main steps: the fitting of measured arresting angles of chute flows of different heights to a set of h_{stop} curves, and the collapsing of measured steady state Froude numbers on a linear fit when the flow height was scaled with h_{stop} . For both steps it was not known on beforehand if they would work for bi-dispersed flows. For both however, I did find results to be in agreement up to the same extent as for mono-dispersed flows. To measure the h_{stop} -curve and the steady state Froude numbers, I set-up a series of DPM simulations, which allowed me to do experiments that are difficult or impossible to do in real life. For both the h_{stop} -curves and the steady state Froude fit, simulations were performed in a periodic box, which made it possible to simulate a system in steady state with relatively low numbers of particles. In the results the h_{stop} -curves did not show major deviations from the proposed fit, and the only problem I encountered was with the case for a particle size ratio $\sigma^{-1} = 2.0$, for which the data was too noisy and lacking resolution.

The main focus of this part of my research was on the influence of the large particle concentration η on the behaviour of the flow. Whereas the influence of η on the h_{stop} -fit is small when the particle friction coefficients are the same for both small and large particles, a clear dependency was found when the small particles are made less frictional. The latter is a phenomena that is known from real geophysical mass flows, for which large boulders are more frictional (due to their non-spherical shape) than the small pebbles.

With the h_{stop} -fit completed, the next step was the verification of the linear Froude scaling. Note that the applicability of this linear scaling was not at all certain at the start of this research, since for flows of different height the flow velocity will be different, which can have an effect on the shape of the concentration profile throughout the depth of the flow. To verify the Froude relation a series of steady flows with different mixtures (different η), inclinations, heights and size-ratios was set up, and the depth averaged Froude number and the flow height were measured. For the cases with varying η , all simulations collapsed nicely on the linear fit. However, for the case with varying σ this was less obvious, since this linear scaling depends heavily on the quality of the h_{stop} -fit. Therefore I have formulated a combined fitting routine, which, given the assumption that the linear Froude fit holds, fits the h_{stop} -curve and the Froude relation in a single fit. This has the effect that the Froude-fit affects

the h_{stop} -fit, the h_{stop} -curve is ‘bend’, such that the linear Froude relation holds. This proved to work well, and I am of the opinion that it is a valuable tool to acquire fit parameters with a high precision. Having fitted the linear Froude fit I found that the important fit parameter β , marking the slope of the linear Froude-curve was almost independent of η for both the case with equal particle friction and the case with reduced friction of the small particles. This hypothesis was strengthened by the combined fit procedure, for which the variation in β for varying η became even smaller. For varying σ the role of β is less clear, but it certainly does not show a nature independent of σ . The amount of data available however is too limited to draw any definite conclusions.

The next step I took was aimed to answer the second research question: can the Pouliquen flowrule be used to predict the friction in a developing, bi-dispersed avalanche? For this I used a quasi 2D domain, periodic in y -direction, with the avalanche flowing freely in x -direction. A novel inflow technique was used which ensured steady state inflow, and the friction law as derived using the h_{stop} -curve and Froude-fits was used to predict the friction coefficient as a function of flow variables, being the Froude number F , the flow-height h and the large particle concentration η . From these results two important conclusions are formulated. First of all: in general the friction law predicts the friction coefficient up to a fair accuracy, and the incorporation of the concentration η was shown to be of significant importance. Second, the model failed in capturing all phenomena influencing the friction. This is due to the general idea of the Pouliquen friction-law: it is fitted with data measured from steady flows. However, in the avalanche front there are flow configurations which do not exist in a steady state (i.e, large particles at the front are overrun and end up temporarily at the bottom of the flow, introducing extra friction), rendering the correct prediction of the friction impossible with only depth averaged information.

5.2 Recommendations

As with any other project carried out in a limited amount of time I encountered several problems, possible solutions and in general interesting directions during my research which in my opinion are worth pursuing. First of all, the most obvious follow-up for this thesis would be to actually use the friction law that was derived to numerically solve the depth averaged shallow layer equations with it. It will be very interesting whether the resulting avalanches resemble the results from the DPM simulations. Secondly, halfway through the project I came to the conclusion that the simple bi-dispersed system was in fact not so simple. The result of having particles of only two exact sizes introduces phenomena like extreme layering which are not observed in real geophysical mass flows, in which there is always poly-dispersity which severely affects or even destroys layering structures. Therefore the introduction of a small variance in the large and small particle sizes might yield different results. Thirdly, the role of the size-ratio σ is not treated very thoroughly in this research. An interesting approach would be to investigate up to what size-ratio the friction law works. Finally, the major lack of accuracy in predicting the friction for the quasi 2D avalanche was due to the unsteady segregation profiles. This unsteady segregation profile is the result of layers of large particle being overrun and ending up (temporarily) at the bottom of the flow, an unsteady position for them, as they will be segregated upwards again. A solution for this problem is not directly evident, but one can think of implementing a correction factor which takes the deviation from the steady segregation into account. This however imposes the need of depth-dependent data on the segregation profile, quantifying the ‘unsteadiness’ of the segregation profile.

Bibliography

- [1] R. A. Bagnold. Experiments on a Gravity-Free Dispersion of Large Solid Spheres in a Newtonian Fluid under Shear. *Proceedings of the Royal Society of London. Series A.*, 225(1160):49–63, Aug. 1954.
- [2] O. Bokhove and A. R. Thornton. Shallow granular flows. Technical Report 1921, Department of Applied Mathematics, University of Twente, Enschede, May 2010.
- [3] J. Bridgwater. Fundamental powder mixing mechanisms. *Powder Technology*, 15(2):215–236, Nov. 1976.
- [4] P. A. Cundall and O. D. L. Strack. A discrete numerical model for granular assemblies. *Géotechnique*, 29(1):47–65, Jan. 1979.
- [5] A. Daerr and S. Douady. Two types of avalanche behaviour in granular media. *Nature*, 399(6733):241–243, May 1999.
- [6] J. A. Drahn and J. Bridgwater. The mechanisms of free surface segregation. *Powder Technology*, 36(1):39–53, Sept. 1983.
- [7] Y. Forterre and O. Pouliquen. Long-surface-wave instability in dense granular flows. *Journal of Fluid Mechanics*, 486:21–50, 2003.
- [8] GDR MiDi. On dense granular flows. *The European Physical Journal E: Soft Matter and Biological Physics*, 14(4):341–365, Aug. 2004.
- [9] I. Goldhirsch. Stress, stress asymmetry and couple stress: from discrete particles to continuous fields. *Granular Matter*, 12(3):239–252, Mar. 2010.
- [10] I. Goldhirsch and N. Sela. Origin of normal stress differences in rapid granular flows. *Physical Review E*, 54:4458–4461, Oct. 1996.
- [11] J. M. N. T. Gray, Y. C. Tai, and S. Noelle. Shock waves, dead zones and particle-free regions in rapid granular free-surface flows. *Journal of Fluid Mechanics*, 491:161–181, Aug. 2003.
- [12] J. M. N. T. Gray and A. R. Thornton. A theory for particle size segregation in shallow granular free-surface flows. *Proceedings of the Royal Society A: Mathematical, Physical and Engineering Science*, 461(2057):1447–1473, May 2005.
- [13] R. M. Iverson. The physics of debris flows. *Reviews of Geophysics*, 35(3):245–296, 1997.
- [14] S. Luding. Introduction to discrete element methods : basic of contact force models and how to perform the micro-macro transition to continuum theory. *European Journal of Environmental and Civil Engineering*, 12(7-8), 2008.
- [15] G. V. Middleton. *Experimental Studies Related to Problems of Flysch Sedimentation.*, volume 7. The Geological Association of Canada, 1970.
- [16] O. Pouliquen. Scaling laws in granular flows down rough inclined planes. *Physics of Fluids*, 11(3):542–548, 1999.
- [17] O. Pouliquen and Y. Forterre. Friction law for dense granular flows: application to the motion of a mass down a rough inclined plane. *Journal of Fluid Mechanics*, 453:133–151, Jan. 2002.

- [18] O. Pouliquen and J. W. Vallance. Segregation induced instabilities of granular fronts. *Chaos: An Interdisciplinary Journal of Nonlinear Science*, 9(3):621–630, 1999.
- [19] S. B. Savage and K. Hutter. The motion of a finite mass of granular material down a rough incline. *Journal of Fluid Mechanics*, 199(-1):177–215, Jan. 1989.
- [20] S. B. Savage and C. K. K. Lun. Particle Size segregation in inclined chute flow of dry cohesionless granular solids. *Journal of Fluid Mechanics*, 189:311, 1988.
- [21] L. E. Silbert, D. Ertas, G. S. Grest, T. C. Halsey, D. Levine, and S. J. Plimpton. Granular flow down an inclined plane: Bagnold scaling and rheology. *Physical Review E*, 64(5):051302+, Oct. 2001.
- [22] A. Thornton, T. Weinhart, S. Luding, and O. Bokhove. Frictional dependence of shallow-granular flows from discrete particle simulations. *EPJE*, 35(12):1–8, 2012.
- [23] A. Thornton, T. Weinhart, S. Luding, and O. Bokhove. Modeling of particle size segregation: Calibration using the Discrete Particle Method. *International Journal of Modern Physics C*, 23(08):1240014+, Aug. 2012.
- [24] A. R. Thornton, D. Krijgsman, R. H. A. Fransen, S. Gonzalez, D. Tunuguntla, Voortwis, S. Luding, O. Bokhove, and T. Weinhart. Mercury-DPM: Fast particle simulations in complex geometries. *Enginsoft Newsletter Simulation Based Engineering & Sciences*, 10(1):48–53, 2013.
- [25] T. Weinhart, R. Hartkamp, A. R. Thornton, and S. Luding. Coarse-grained local and objective continuum description of 3D granular flows down an inclined surface. *Phys. Fl.*, 25(6), 2012.
- [26] T. Weinhart, A. Thornton, D. Krijgsman, S. Luding, and O. Bokhove. Mercury DPM. <http://www2.msm.ctw.utwente.nl/athornton/MD/>.
- [27] T. Weinhart, A. R. Thornton, S. Luding, and O. Bokhove. Closure relations for shallow granular flows from particle simulations. *Granular Matter*, 14(4):531–552, July 2012.
- [28] T. Weinhart, A. R. Thornton, S. Luding, and O. Bokhove. From discrete particles to continuum fields near a boundary. *Granular Matter*, 14(2):289–294, Apr. 2012.
- [29] M. J. Woodhouse, A. R. Thornton, C. G. Johnson, B. P. Kokelaar, and J. M. N. T. Gray. Segregation-induced fingering instabilities in granular free-surface flows. *Journal of Fluid Mechanics*, 709:543–580, Sept. 2012.